AN ANALYSIS OF THE WIND-FORCED RESPONSE OF CONCEPTION BAY USING A REDUCED-GRAVITY NUMERICAL MODEL

TIMM OTTERSON

AN ANALYSIS OF THE WIND-FORCED RESPONSE OF CONCEPTION BAY USING A REDUCED-GRAVITY NUMERICAL MODEL

by

©Timm Otterson

A thesis submitted to the School of Graduate

Studies in partial fulfillment of the

requirements for the degree of

Master of Science

Department of Physics

Memorial University of Newfoundland

1992

St. John's Newfoundland

ISBN 0-315-73325-X

ABSTRACT

A reduced-gravity numerical model of Conception Bay, Newfoundland, with a realistic coastline and driven by local wind is developed to analyze the wind-forced reponse of the pycnocline. Model solutions are compared with temperature and current measurements collected from sub-surface moorings deployed at the mouth in the spring of 1989 and near the head in the spring of 1990. The observed temperature near the head shows similar behavior at all six moorings indicating upwelling of the pycnocline due to northeastward winds. Upwelling around the head and evidence of phase lag from one mooring to the next are consistent with Kelvin wave propagation. The model reproduces most of this variability at all six moorings including the two moorings on the eastern side of the Bay near Bell Island Tickle where Kelvin waves might be expected to be scattered by bottom topography. At the mouth, only the 2 day temperature signal at the mooring closest to the western shore is successfully reproduced by the model. The model's ability to better reproduce temperature variability at the head is explained by the increased wind-forced response at the head and the likely importance of external forcing at the mouth, either from Trinity Bay or due to eddies entering the Bay from outside. The current field at both the head and mouth is poorly reproduced by the model, probably due to the complicated vertical structure of the current. Coherence analysis of the current data shows that the horizontal scale of coherent motions is small (less than 10 km).

In developing the model used for comparison with observations, boundary conditions that allowed an accurate solution were developed. Placing a radiation condition perpendicular to the coast "upstream" of the Bay resulted in the generation of spurious fluxes and

near-inertial Kelvin waves at the boundary. These problems were eliminated by extending the coastline out to sea on the "upstream" side of the mouth and applying a condition of zero normal gradient in interface displacement on the artificial stretch of boundary. Experiments using sponge layers rather than radiation conditions on the other boundaries showed that sponging only the interface displacement and leaving the velocities undamped gives results that compare well with those obtained using radiation conditions. Sponging the velocities as well as the interface displacement led to significantly different results suggesting that applying highly viscous layers around open ocean parts of model boundaries can be counter-productive.

TABLE OF CONTENTS

TABLE OF CONTENTS (Continued) Page

LIST OF FIGURES

ACKNOWLEDGEMENTS

I would like to thank my two supervisors, Brad de Young and Richard Greatbatch, for conceiving this project and providing the guidance and support necessary for its conclusion. Thanks go out to all those who worked on acquiring the field data used in this thesis, with special thanks due to Jack Foley and Ken Forward, to Allan Goulding for his help with computing, to Kevin Lamb for allowing the use of his workstation, and Roger Guest for drafting several figures. Thanks are also due to the reviewers of Greatbatch and Otterson (1991), whose comments led to an improved understanding and presentation of the boundary condition formulation, and to the reviewers of earlier versions of this thesis for providing many helpful comments.

Monetary support for my research was provided by a grant from the Natural Science and Engineering Research Council of Canada in support of the Cold Ocean Productivity Experiment (COPE).

Many thanks go out to the numerous unmentioned people who contributed in different ways to this thesis and who make this department a nice place to work and the world an amusing place to live.

And thank you Morrissey.

CHAPTER 1: INTRODUCTION

Conception Bay is one of many bays located along the east coast of the island of Newfoundland (see Figure 1.1). The Bay is situated facing northeast on the most southeasterly part of the island, the Avalon Peninsula. To the west is Trinity Bay, a deep water bay connected to the sea via a deep trough. Conception Bay, although a deep bay, is separated from the sea by a sill of roughly 180m depth. To the south and east lie the Grand Banks, still one of the most fertile ocean regions in the world. Newfoundland's largest city and capital, St. John's, is located roughly 30 kilometers east of Conception Bay making it the most observed bay in the region (Aggett et al., 1987).

The ocean off the east coast of Newfoundland is dominated by two major currents. The Gulf Stream flows just south of the Grand Banks bringing warm, saline water into the northern Atlantic. The Labrador Current flows southward carrying cold, fresh water along the shelf and across the Grand Banks (Petrie and Anderson, 1983). The inshore branch of the Labrador Current moves through the Avalon Channel and is thought to strongly influence conditions in Conception Bay. By late winter, most of the east coast of Newfoundland is typically covered by pack ice, much of which forms well north of the study area and is carried southwards by the Labrador Current. Conception Bay is sometimes inundated by pack ice with ice often present from late-February to April.

Newfoundland has a rocky and rugged coastline due to its geologic history and the presence of glaciers, particularly during the last ice age approximately 16,000 years ago. Much of the shoreline around Conception Bay consists of nearly vertical cliffs. The steepest of these cliffs are located on the eastern side of the Bay from near Bell Island to the head at

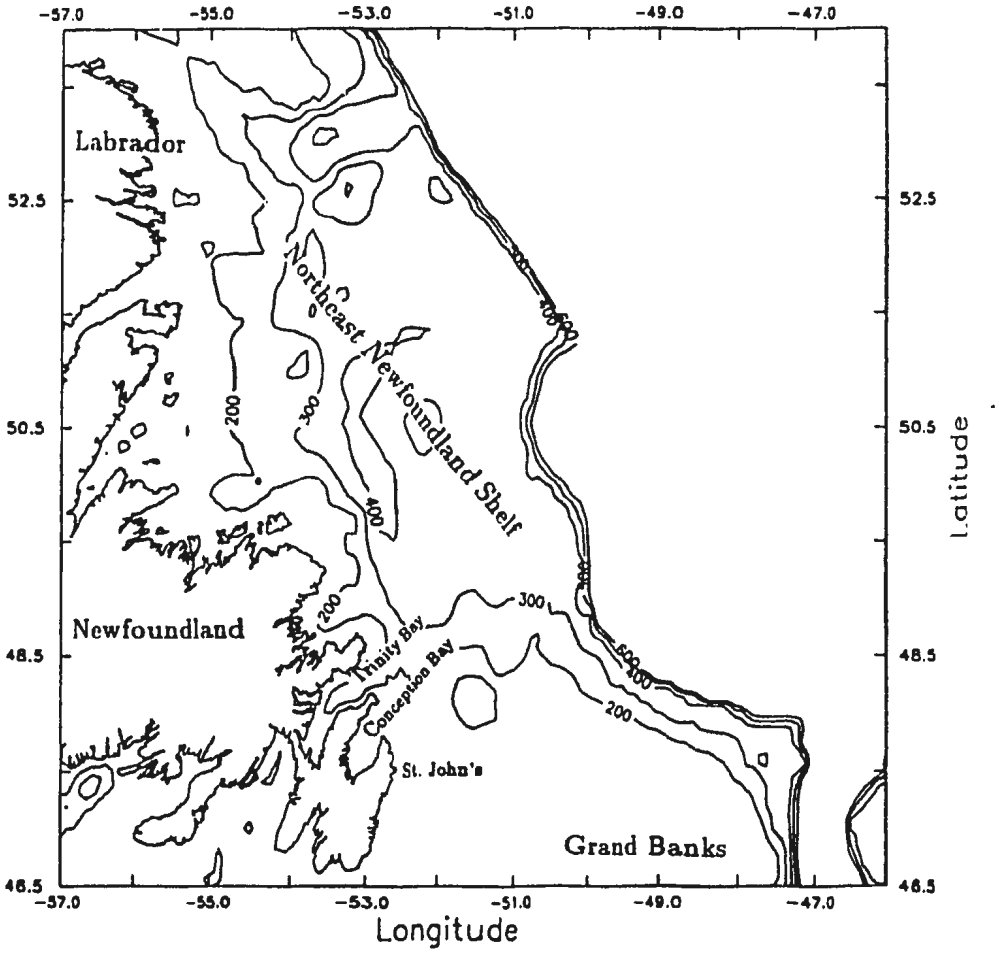

Figure 1.1 Northeast coast of Newfoundland. Conception Bay is located on the southeastern end of the island about 30 km west of St. John's, the capital city. Depth contours are in meters.

Cape St. Francis. The rugged nature of the region suggests that Conception Bay is fairly deep, which is true, with a maximum depth of approximately 300 meters even though the bay is only 30 kilometers wide by 70 kilometers long (see Figure 1.2).

In this thesis, the response of the surface layer of Conception Bay due to wind forcing will be examined using a reduced-gravity, numerical model. The Bay will be shown to be vertically stratified with less-dense water at the surface. The stratification tends to limit the wind-forced response to the surface allowing for the simplification of the governing equations.

The vertical structure of the ocean is often described as a well-mixed, surface layer separated by a transition region, called the pycnocline, from a layer of denser water at depth. The depth of the mixed-layer and the size and density gradient in the pycnocline vary, but, in general, the ocean consists of a warmer, upper layer lying on a colder, more-dense, lower layer. The depth and density of the mixed layer are controlled by several factors, with the primary ones being heat transfer at the surface and vertical mixing due to wind (Kraus and Turner, 1967). Fresh water input at the surface can also act to reduce the density and depth of the mixed layer. Since density is a function of temperature and salinity, the vertical profile of density at a given location will also depend on the time of the year and the intensity and duration of solar radiation in the region. Upper layers in higher latitudes, such as Newfoundland, tend to be shallower and denser than upper layers in lower latitudes (Pickard and Emery, 1982). In fact, at the end of winter in Conception Bay, the upper layer has been cooled to the point where the vertical density profile is essentially homogeneous because of vertical convection. With the advent of spring, the surface density on the eastern

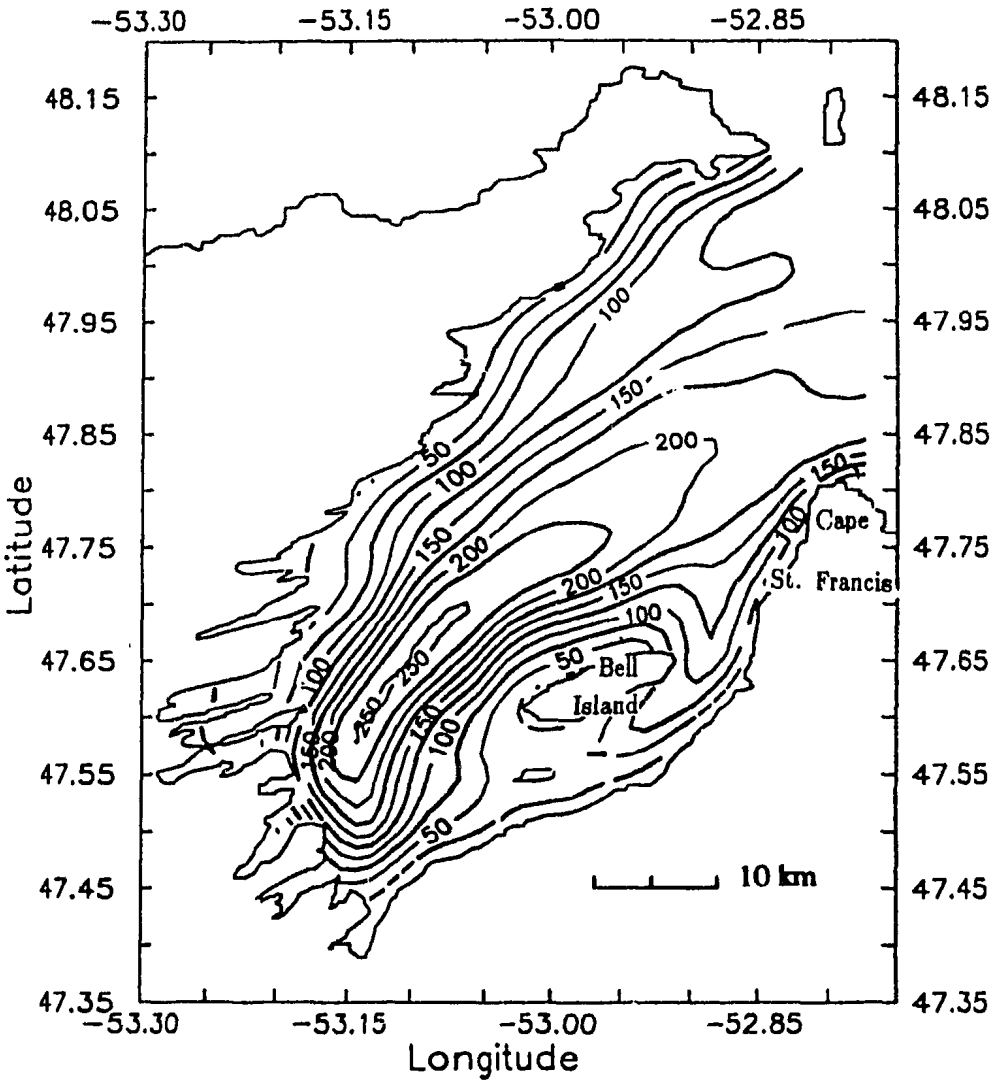

Figure 1.2 Topography of Conception Bay. The contour interval is 50 meters.

Newfoundland shelf is reduced by an increase in temperature due to solar heating and a decrease in salinity due to freshwater runoff and melted sea-ice. Petrie et al., (1991) show that vertical mixing of heat input by solar radiation raises the temperature along the shelf from its minimum in spring to a peak in early fall. The increase in temperature acts in tandem with a decrease in salinity from melted sea-ice and freshwater runoff to reduce the density throughout the water column on the shelf (Keeley, 1981). The amplitude of yearly temperature and salinity variations are largest at the surface.

Momentum input by wind stress at the ocean surface will be mixed downwards throughout the upper layer causing it to move in the horizontal plane. If the wind is blowing parallel to a coastline, currents created by the wind will be turned to the right by the Coriolis force (in the northern hemisphere) and cause either convergence or divergence in the upper layer at the coast. If the currents are turned into the coast, convergence in the upper layer will occur, depressing the pycnocline (downwelling). If the currents are turned away from the coast, divergence in the upper layer will occur, raising the pynocline (upwelling). In the upwelling case, the pycnocline is lifted at the coast bringing cooler sub-surface water upwards. In the downwelling case, the pycnocline is depressed at the coast pushing warmer water downwards. Fluctuations in the pycnocline will be transmitted along the pycnocline and throughout the water column by a variety of waves. The primary wave of interest in this thesis is the internal Kelvin wave. Kelvin waves are waves trapped at the coastline by the Earth's rotation. The equations describing Kelvin waves in a uniform density, flat-bottomed ocean can be easily derived from the governing equations

$$\frac{\partial u}{\partial t} - fv = -g\frac{\partial \eta}{\partial x},$$

$$\frac{\partial v}{\partial t} + f u = -g\frac{\partial \eta}{\partial y}. \qquad (1.1)$$

$$\frac{\partial \eta}{\partial t} + H\left(\frac{\partial u}{\partial x} + \frac{\partial v}{\partial y}\right) = 0,$$

where η is the upwards displacement at the surface, u and v are the velocities in the x and y directions, respectively, and are independent of depth, f is the Coriolis parameter, g is the acceleration due to gravity, H is the ocean depth, and external forcing (i.e., wind stress at the surface) has been neglected. For a straight coastline with $y \leq 0$ being land, solutions can be sought for which the component of velocity normal to the coast is equal to zero, (i.e., the terms involving v can be dropped since v must equal zero at the coast). Equations (1.1) then have two solutions with the physical one (in the northern hemisphere) given by equations (1.2):

$$\eta = \eta_o e^{-y/a}\cos(kx - \omega t),$$

$$u = \eta_o \left(\frac{g}{H}\right)^{1/2} e^{-y/a}\cos(kx - \omega t), \qquad (1.2)$$

where η_o is the amplitude of the surface displacement, k is the wavenumber, ω is the angular frequency, and a is the Rossby radius of deformation equal to c/f, where $c = (gH)^{1/2}$ is the propagation speed of a long gravity wave. For simplicity, the wave is assumed to be sinusoidal, but could have other shapes (see Gill, 1982, Equation 10.4.7). The Kelvin wave has no component of velocity normal to the coast ($v = 0$), propagates with the coast on its right (in the northern hemisphere), and decays exponentially away from the coast over distances on the order of the Rossby radius. The dispersion relation is given by $\omega = kc$, and, since c is constant, wavelength and frequency are linearly related to one another.

Displacement of the pycnocline will generate internal Kelvin waves that propagate in the same manner. Equations (1.3) are for the idealized case of a Kelvin wave propagating

along the interface between an upper layer of depth H_1 and density ρ_1 and an infinitely deep lower layer of density ρ_2.

$$\begin{aligned} \eta &= \eta_1 e^{-y/a_1} \cos(k_1 x - \omega_1 t), \\ u &= \eta_1 \left(\frac{g'}{H_1}\right)^{1/2} e^{-y/a_1} \cos(k_1 x - \omega_1 t). \end{aligned} \tag{1.3}$$

where η is the downwards displacement of the interface, η_1 is the amplitude of the interface displacement, $g' = g(\rho_2 - \rho_1)/\rho_1$ is the reduced gravity, $c_1 = (g' H_1)^{1/2}$ is the propagation speed, $a_1 = c_1/f$ is the baroclinic Rossby radius, and the shape of the wave is assumed to be sinusoidal. The dispersion relation is $\omega_1 = k_1 c_1$. g' and H_1 are much less than g and H, respectively, making the propagation speed and the Rossby radius much smaller for baroclinic waves.

These two waves are similar to waves that exist in the first two vertical normal modes in a continuously stratified, flat-bottomed ocean. Such a system has an infinite number of vertical modes. The horizontal structure associated with each mode is described by the shallow water equations

$$\begin{aligned} \frac{\partial u_n}{\partial t} - f v_n &= -g \frac{\partial \eta_n}{\partial x}, \\ \frac{\partial v_n}{\partial t} + f u_n &= -g \frac{\partial \eta_n}{\partial y}, \\ \frac{\partial \eta_n}{\partial t} + H_n \left(\frac{\partial u_n}{\partial x} + \frac{\partial v_n}{\partial y}\right) &= 0, \end{aligned} \tag{1.4}$$

where n is the number of the mode, H_n is an equivalent depth that determines the mode wave speed $c_n = (g H_n)^{1/2}$, u_n and v_n are the velocities of each mode in the x and y directions, respectively, and η_n is the effective displacement representing the pressure in each mode. The $n = 0$ mode describes the barotropic case in which H_0 is the ocean depth,

making $c_0 = 55$ ms^{-1} for $H_0 = 300$ meters, η_0 is the surface displacement, and the velocity field is independent of depth (i.e., the equation (1.2) case). The subsequent n modes are defined by c_n. These have the property that $c_0 > c_1 > \cdots > c_{n-1} > c_n > c_{n+1} > \cdots$. The c_n for $n \geq 1$ depend on the stratification. c_n is usually in the range 0.5 to 3 ms^{-1} for the $n = 1$ mode, and for large n, the c_n decrease as $1/n$. The total solution is attained by summing over all the modes (see Gill, 1982, Chapter 6).

For the case of Conception Bay, the coastline is not straight but has a U-shaped bend at the head along with irregular smaller-scale features. Kelvin wave propagation and reflection along irregular coastlines was first considered by Taylor (1920) and, more recently, by Buchwald (1968) for the case of a right-angled bend and by Packham and Williams (1968) for a bend with a general angle. They showed that Kelvin waves will propagate around a bend with the boundary condition of no flow normal to the boundary being satisfied by including Poincaré waves. Poincaré waves can be found as solutions to

$$\frac{\partial^2 \eta}{\partial t^2} - c^2 \left(\frac{\partial^2 \eta}{\partial x^2} + \frac{\partial^2 \eta}{\partial y^2} \right) + f^2 \eta = 0 \tag{1.5}$$

(This equation can easily be derived from equations (1.1).) When solutions of the form $\eta \propto \exp i(kx + ly - \omega t)$ are sought for equation (1.5), where $i = (-1)^{1/2}$ and k and l are the wavenumbers in the x and y directions, the dispersion relation is

$$\omega^2 - f^2 = c^2(l^2 + k^2) \tag{1.6}$$

For frequencies with $|\omega| > |f|$, propagating Poincaré waves will be generated as a Kelvin wave travels around a bend, while for Kelvin waves with $|\omega| < |f|$, Poincaré waves that

decay exponentially (i.e., evanescent Poincaré waves) will be generated. In this thesis, we shall mostly be concerned with sub-inertial Kelvin waves for which $|\omega| < |f|$. Packham and Williams (1968) showed that these Kelvin waves propagate around corners with no loss of amplitude. This is because evanescent Poincaré waves do not transmit energy. On the other hand, they did find some loss of energy to propagating Poincaré waves in the case of super-inertial Kelvin waves ($|\omega| > |f|$). This will not concern us here.

Considerable effort has been put into understanding upwelling and its possible effects on fish populations and climate. Smith (1968) provides a fundamental study of the physical processes and observations of large-scale upwelling at different locations throughout the world. He describes the initial hypothesis of Ekman (1905) that a steady, uniform wind blowing over an infinite ocean will transport water to the right (in the northern hemisphere) and its application by Sverdrup (1938) to explain upwelling/downwelling at a coast. Before computers became widely available, several analytic models were developed (Hidaka (1954); Yoshida (1955)) that sought to explain aspects of upwelling by making assumptions that simplify the solution, such as two-layer stratification, straight coastlines and uniform winds blowing parallel to the coast. Although such models are instructive about the nature of certain upwelling features, they are limited in that they are analytic and, therefore, only apply to idealized geometries and forcing. The advent of affordable computing has allowed oceanographers to further explore the processes involved in upwelling by including more realistic stratification, irregular coastlines and time-varying winds.

The problem of wind-forced upwelling and, in particular, the role of Kelvin waves has been addressed by Gill and Clarke (1974). These authors derive an equation describing the

propagation of an internal Kelvin wave along a coastline and its modification by alongshore wind stress. To arrive at an equation describing internal Kelvin wave propagation, an ocean with a straight coastline at $y = 0$ and alongshore wind stress only is assumed. Since wind stress varies over length scales much larger than the internal radius of deformation, the alongshore length scale will be much greater than c/f. Solutions can then be restricted to the case in which time scales are long compared to $1/f$ and alongshore variations (i.e., with x) are slow compared with variations normal to the shore (i.e., with y). The equations of motion yield the following equation.

$$\frac{1}{c}\frac{\partial \eta}{\partial t} + \frac{\partial \eta}{\partial x} = X(x,t) \tag{1.7}$$

where η is the downwards displacement of the pycnocline at the coast, c is the speed of an internal Kelvin wave, t is time, x is alongshore distance, and X is proportional to the alongshore wind stress. Equation (1.7) provides an analytic description of how the amplitude of a propagating internal Kelvin wave will change in response to wind forcing (see also Gill, 1982, Chapter 10). Their simplified theory can be used to interpret the solutions of a numerical model with realistic wind-forcing and coastline.

The aim of this thesis is to model the movement of the pycnocline in Conception Bay in response to wind forcing and compare the model results to observations. In an earlier study of neighboring Trinity Bay, Yao (1986) found some evidence of a wind-forced response. Yao showed that there is significant coherence between observed alongshore wind stress and alongshore currents, especially at frequencies near 0.2 cpd. He applied the idealized two-layer model developed by Gill and Clarke (1974) by approximating Trinity Bay

as a U-shaped, flat-bottomed bay driven by uniform wind stress. Yao showed that this simplified model can reproduce several features observed in current measurements. The model predicted that a wind blowing out the bay initially produces upwelling on one side of the bay and downwelling on the other, as indicated by the current meter data. Yao's model was also able to account for a significant amount of the variance at a frequency of 0.2 cpd (i.e., the same frequency where observed wind and current had significant coherence). Agreement between the model and observations was better at positions toward the head of the bay. Yao speculated that outside influences, possibly the Labrador Current, were responsible for a significant part of the signal, especially toward the mouth.

To investigate the movement of the pycnocline in Conception Bay in response to wind forcing, a 1-1/2 layer model with a realistic coastline driven by wind measured at nearby St. John's has been developed. The 1-1/2 layer model assumes that the ocean has two distinct layers of different density and that the lower layer is infinitely deep and at rest. This model is the simplest, most computationally efficient model used to represent the upper layer of the ocean. The equations governing a 1-1/2 layer ocean are the same as the ones governing the baroclinic modes in a continuously stratified, flat-bottomed ocean. In a series of papers beginning with Busalacchi and O'Brien (1980), O'Brien and co-workers have shown that such a model has considerable success in reproducing observed sea level variability in equatorial regions and also along the Pacific coast of North America (Pares-Sierra and O'Brien (1989) and Johnson and O'Brien (1990a,b)). In a similar way, we intend to determine how effective a 1-1/2 layer model is at reproducing variablity in the upper layer of a mid-latitude bay. When developing a numerical model of this kind, the boundary

conditions must be carefully specified to avoid the influx of spurious information through the open boundaries. The formulation of the open boundaries that minimizes the presence of spurious information in the solution is described in Chapter 3 of this thesis and in a paper by Greatbatch and Otterson (1991).

The work presented in this thesis is part of a larger effort known as the Cold Ocean Productivity Experiment (COPE). COPE is a cooperative effort among biological, physical, and chemical oceanographers to better understand microbial production and respiration in a cold water environment. The goal of this program is to describe energy flow along three major pathways: loss to microbial activity, loss to metazoan grazers, and loss through sinking to the benthos. Thermal suppression of the microbial activity was hypothesized. As part of this effort, a large amount of data on the physical oceanography was collected (deYoung and Sanderson, 1992). The model developed in this thesis for the wind-forced response of the Bay is used to interpret observed temperature changes in the pycnocline on time scales of a few days.

The outline of this thesis is as follows. Chapter 2 presents the data used in specifying the 1-1/2 layer model and field measurements used to evaluate the model. Chapter 3 describes the numerical model and the boundary conditions required to assure an accurate solution in the Bay. Chapter 4 presents comparisons between the model and the observations. A summary of the work and conclusions are presented in Chapter 5.

CHAPTER 2: DATA

This chapter describes the data used to specify the 1-1/2 layer model and to make the comparison of observations with model solutions. The data presented include wind data from St. John's airport (see Figure 1.1), conductivity, temperature, and density (CTD) data from cruises, and current meter and thermistor data from moorings deployed in Conception Bay. All current meter, thermistor and wind data presented have been filtered using a low-pass Butterworth filter so that most of the energy with frequency greater than one cycle per day is removed. Filtering is done because we are only interested in the low frequency response, since high-frequency ($>$ 2 cpd) and tidal energy compose a small part of the energy in Conception Bay (deYoung and Sanderson, 1992). A low-pass filter is used with a cut-off near 30 hours. At 32 hours, greater than 99% of the signal is passed, while less than 25% is passed at 30 hours. The filter is run over the data in the forward and reverse directions to neutralize phase distortion. All data presented are in Greenwich Mean Time (GMT).

2.1: Wind Data

The model of Conception Bay is driven by wind stress exclusively. Therefore, reliable wind data are essential. A variety of physical processes make knowing the wind field over a bay like Conception Bay difficult.

To translate wind velocity into surface wind stress, the wind must be known at a certain height above the water surface; the standard reference height is 10 meters (Large and Pond, 1981). In the case of Conception Bay, long period measurements of wind velocity over the center of the bay are difficult to make. Six months of wind data were obtained

on Bell Island in an unsuccessful attempt to measure the wind. Comparison of St. John's wind with that from Bell Island showed that measurements at Bell Island were influenced by orographic effects and, thus, are not representative of the wind field over Conception Bay. The weather station at St. John's airport, located 30 km to the east of the bay and on land, provides the only reliable wind data in the area. Comparison of St. John's wind data with data collected during a limited period at a weather station in Kelligrews, located on a flat region toward the head of the Bay, showed good agreement. This implies that wind measured at St. John's airport is representative of wind over Conception Bay. Data from the St. John's weather station are used recognizing that there are some doubts about transferring land-based wind measurements to the ocean.

Wind data collected by the Atmospheric Environment Service (AES) at the St. John's airport were obtained for the study period. The airport is located northwest of St. John's on a flat area 150 m above sea level about 5 km from the ocean. Although the airport wind data are expected to have some directional bias due to the presence of hills along the coast, they provide the best available record of the local wind.

At a significant height in the atmosphere beyond the boundary layer, large scale atmospheric movements are nearly geostrophic. The pressure gradient balances the Coriolis force, and flow is parallel to lines of constant pressure. At the land-atmosphere or ocean-atmosphere interface, the air-flow velocity is reduced. This decrease in velocity reduces the Coriolis force and causes the wind velocity at the surface to have a component down the pressure gradient. This means that in the northern hemisphere the surface wind is rotated counter-clockwise from the velocity higher up. The magnitude of the rotation angle

depends on the amount of friction created by the surface, which is a function of surface roughness. For an identical pressure gradient, surface winds over water are generally faster and rotated less than winds over land, because the surface roughness of water is considerably less than that of land. This phenomenon has been demonstrated in numerical models (Taylor, 1969a,b) and verified by measurements (Smith and MacPherson, 1987). When a surface wind leaves land and passes over water, it encounters a transition region where it accelerates and rotates clockwise. A wind leaving water and passing over land encounters a transition region where it decelerates and rotates counter-clockwise. Smith and MacPherson used measurements along the coast of Nova Scotia to show that at a height of 50 m the speed of a wind passing from over land to water increases by roughly 20% over a transition region of 10 kilometers.

Smith and MacPherson's measurement area was over a flat section of the coast. For the case of Conception Bay, the wind field is complicated by convergence and divergence caused by hills that surround the bay as well as the islands within the bay. The influence of the terrain on the local wind field was demonstrated by the behavior of the wind measured at Bell Island. Thus, the wind field over Conception Bay is complicated not only by transition regions due to the difference in surface roughness between water and land, but also by the influence of hills along the coast.

Being the only reliable source, wind data from the St. John's airport are used to determine the wind stress input to the model. Since surface roughness and orographic effects cannot be compensated for in a dependable manner, the wind stress used in the model is assumed uniform over the bay and to be in the same direction as at St. John's. However,

wind speed is scaled by 1.25 following Smith and MacPherson (1987) to compensate for the reduced velocity measured over land. Wind velocity is converted to wind stress following Large and Pond (1981).

$$\tilde{\tau} = \rho_{AIR} C_D |\tilde{U}| \tilde{U} \tag{2.1}$$

where $\tilde{\tau}$ is the surface wind stress, ρ_{AIR} is the density of air, C_D is a dimensionless drag coefficient, and $\tilde{U}$ is the wind velocity at 10 m above the water surface. The drag coefficient according to Large and Pond (1981) is given by

$$10^3 C_D = \begin{cases} 1.14, & \text{if } 4 \text{ ms}^{-1} < |\tilde{U}| \leq 10 \text{ ms}^{-1} \\ 0.49 + 0.065|\tilde{U}|, & \text{if } 10 \text{ ms}^{-1} < |\tilde{U}| < 25 \text{ ms}^{-1} \end{cases} \tag{2.2}$$

These criteria are extended for our case to include velocities above and below those specified by (2.2). C_D is set equal to 0.00114 for wind speeds less than 4 ms^{-1}, and $C_D = (0.49 + 0.065|\tilde{U}|)/1000$ for wind speeds greater than 25 ms^{-1}.

Figure 2.1 shows the wind stress for mid-April to the end of July 1990 calculated using this method. The coordinate system, which we shall refer to as bay coordinates, is shown in Figure 2.2. The positive y-direction points out the bay, and the positive x-direction points across the bay towards the St. John's side. Wind stress components have been filtered using a Butterworth filter with a cut-off at 32 hours to remove energy with frequencies greater than one cycle per day. Note that after 150 days the wind stress is generally positive in both the x and y directions, indicating that the dominant wind in summer 1990 is from the west-southwest.

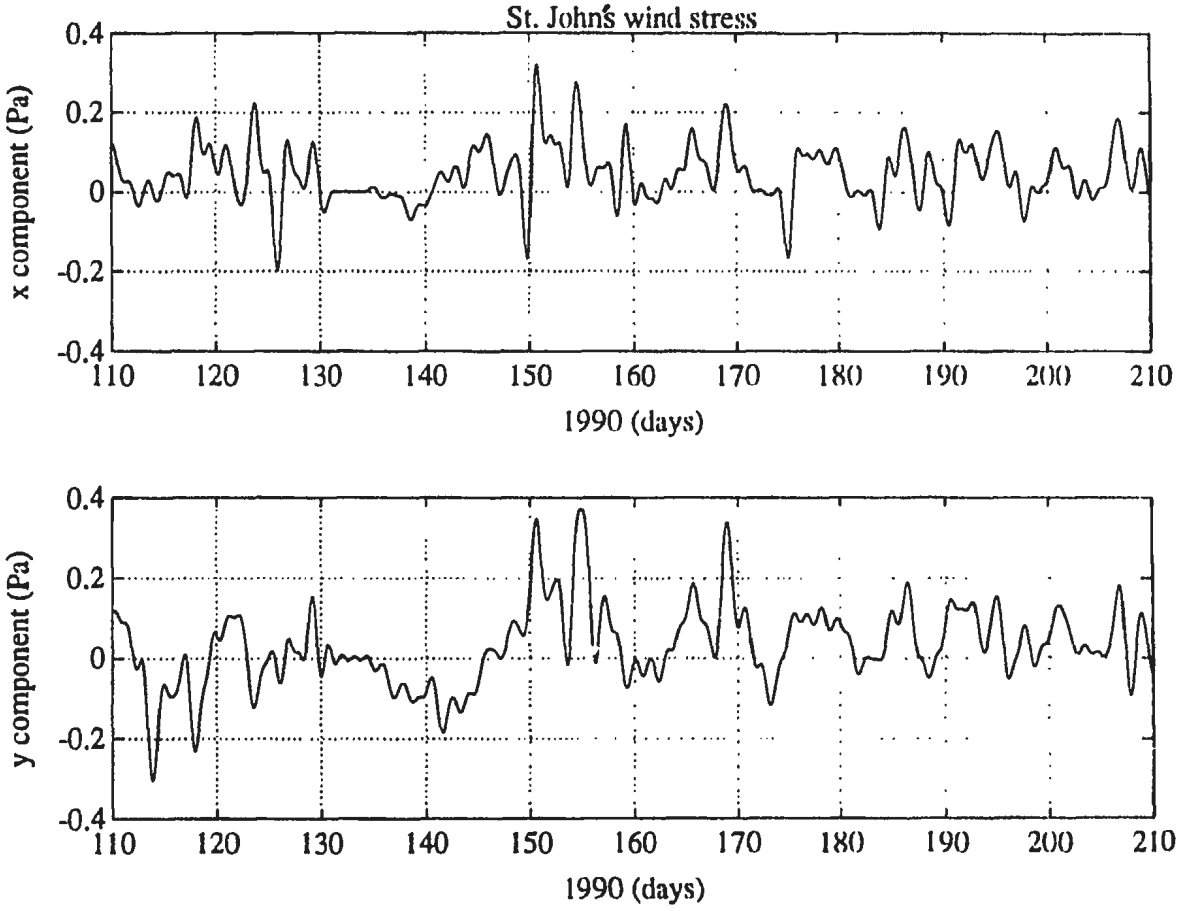

Figure 2.1 Wind stress (in Pa) computed from wind velocity measurements taken at St. John's airport and converted into wind stress following Large and Pond (1981)

2.2: CTD Data and the Use of the 1-1/2 Layer Model

Density, temperature, and salinity have been collected from Conception Bay for the years 1989 and 1990. Measurements were made during both day and week-long cruises using a Neil Brown MkIIIB. Station positions sampled during these cruises are shown in Figure 2.2.

Figure 2.3 shows the density at stations along the CC line (see Figure 2.2) for April 22, 1989. CTD data averaged at 1 m intervals were interpolated onto a fixed grid using a Kriging technique. The figure shows the along-bay density field with 0 km on the x-axis being the head of the bay and 70 km being near the mouth. A shallow, upper layer overlies a diffuse, weak pycnocline. At this time of year, the Bay is beginning to restratify itself after the winter. At the peak of winter, the entire water column is nearly homogeneous in the vertical. There is almost no vertical temperature gradient with the temperature being $-1.5°C$ at the surface and -1.4 to $-1.2°C$ at the bottom. The stratification is preserved by a weak salinity gradient. The upper layer in April is expected to be shallow (as shown in Figure 2.3), since it has only begun to develop.

Figure 2.4 shows the density along the CTR3 line (see Figure 2.2) for April 18, 1989. (Note that the CTR3 and CT3 lines refer to the same station positions but that the "R" has been dropped from Figure 2.2 due to space constraints.) The figure shows the cross-bay density structure of the bay with 0 km on the x-axis located at the shore on the northwest side of the bay and 24 km being the shore on the southeast side of the bay. As in Figure 2.3, a diffuse pycnocline and a shallow upper layer are present. There is evidence of a nearly

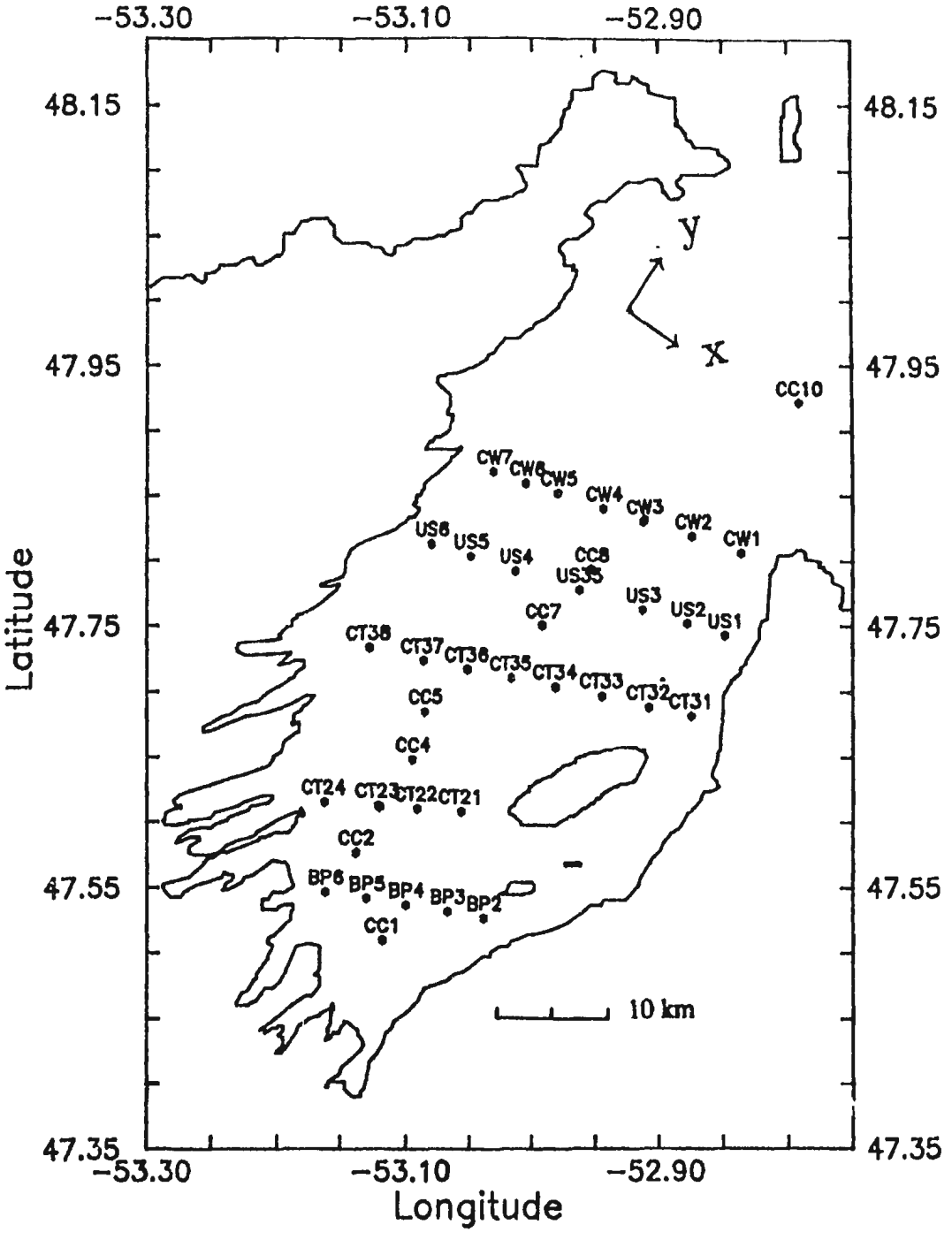

Figure 2.2 CTD station positions in Conception Bay

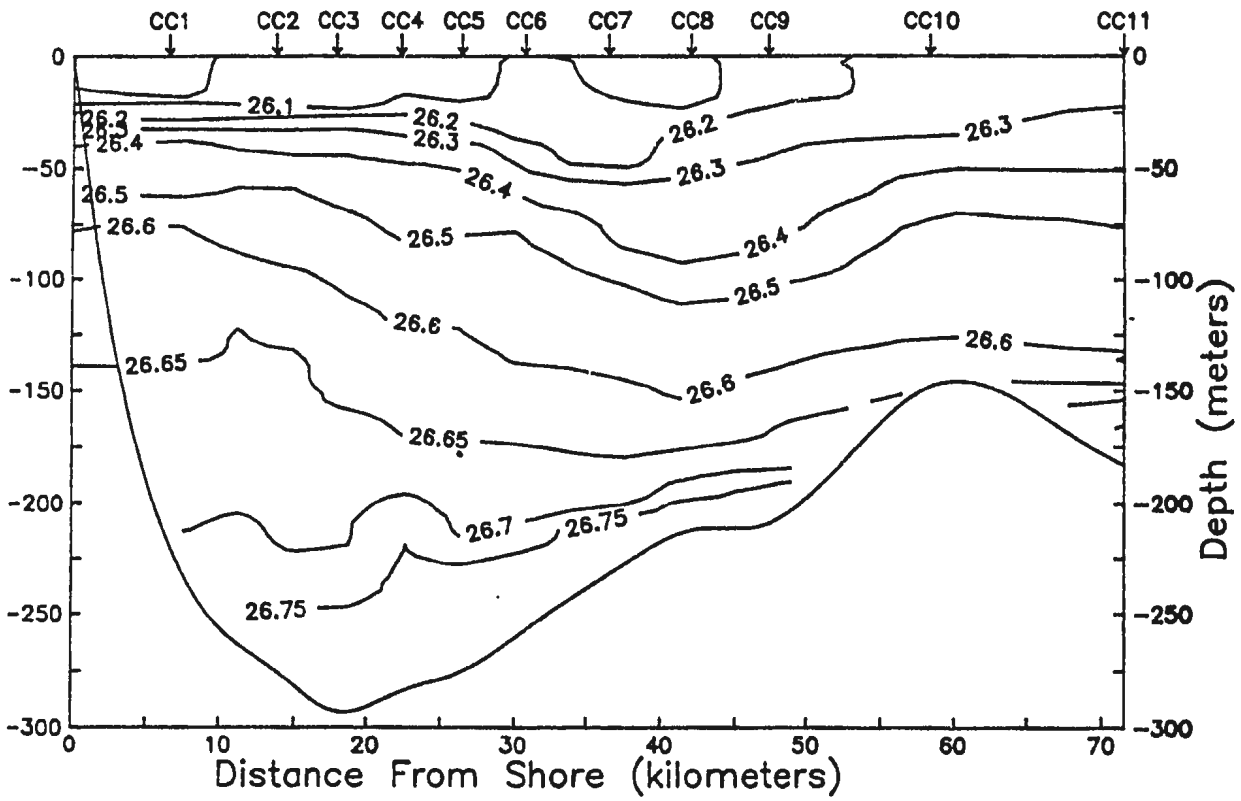

Figure 2.3 Along-bay density field for April 22, 1989 calculated from CTD casts along the CC line shown in Figure 2.2. Densities are given in units of σ_t, where $\sigma_t = \rho(S,T,0)$ - 1000 kgm^{-3}.

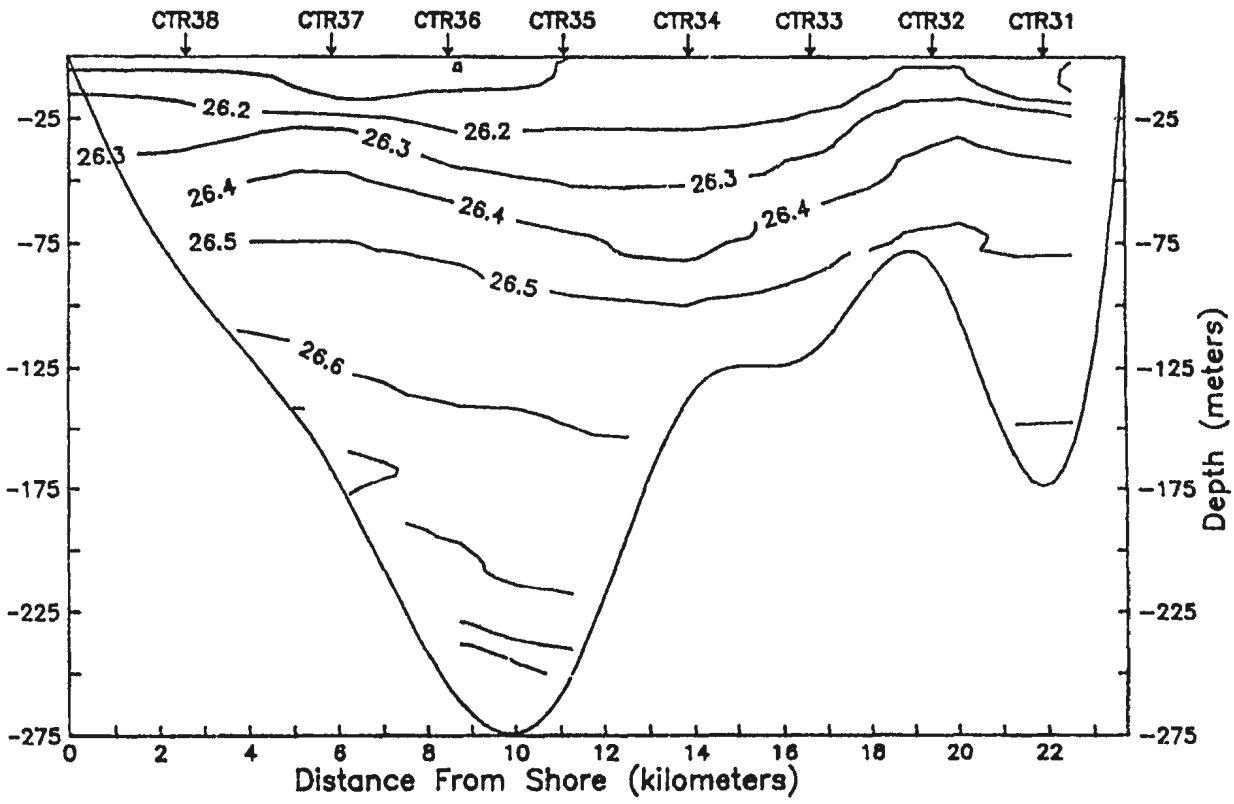

Figure 2.4 Cross-bay density field for April 18, 1989 calculated from CTD casts along the CTR3 line shown in Figure 2.2. Densities are given in units of σ_t. Note that the CTR3 line is shown as the CT3 line in Figure 2.2 due to space constraints.

homogeneous region below 75 meters depth. This nearly homogeneous region below the pycnocline is referred to as the lower layer.

Figure 2.5 shows the density at stations along the CC' line (see Figure 2.2) for November 2, 1989. Comparison of Figures 2.5 and 2.3 shows how the stratification of the water column has developed over the summer. The lower layer exhibits relatively little change in density over the six month period. However, the upper layer and pycnocline have changed considerably. The upper layer density is 1.5 kgm^{-3} less in November than it was in April due to heating at the surface and an influx of less saline water (Petrie et al., 1991), and the pycnocline now extends from 30 to 150 meters depth.

Figures 2.6 and 2.7 show along- and cross-bay density fields for May 5-7, 1990. These plots show essentially the same structure as was observed the previous year (see Figures 2.3 and 2.4). A nearly uniform lower layer is present with a developing pycnocline above 150 meters.

Individual CTD casts can also be used to show the vertical density profile. The vertical profiles at BRLP 5 (shown on Figure 2.2 as station BP 5) for five times during 1989 and 1990 are shown in Figure 2.8. The figure shows the development of the pycnocline during the spring and summer in each year.

The 1-1/2 layer model assumes that the ocean has two distinct layers of different density and that the lower layer is infinitely deep and at rest. The pycnocline is "compressed" into the interface between the two layers. Momentum input by wind forcing at the surface is mixed throughout the upper layer, and the shallow water equations (see equations (1.1)) describe the motion of the upper layer where g is replaced by g', H is the upper-layer depth,

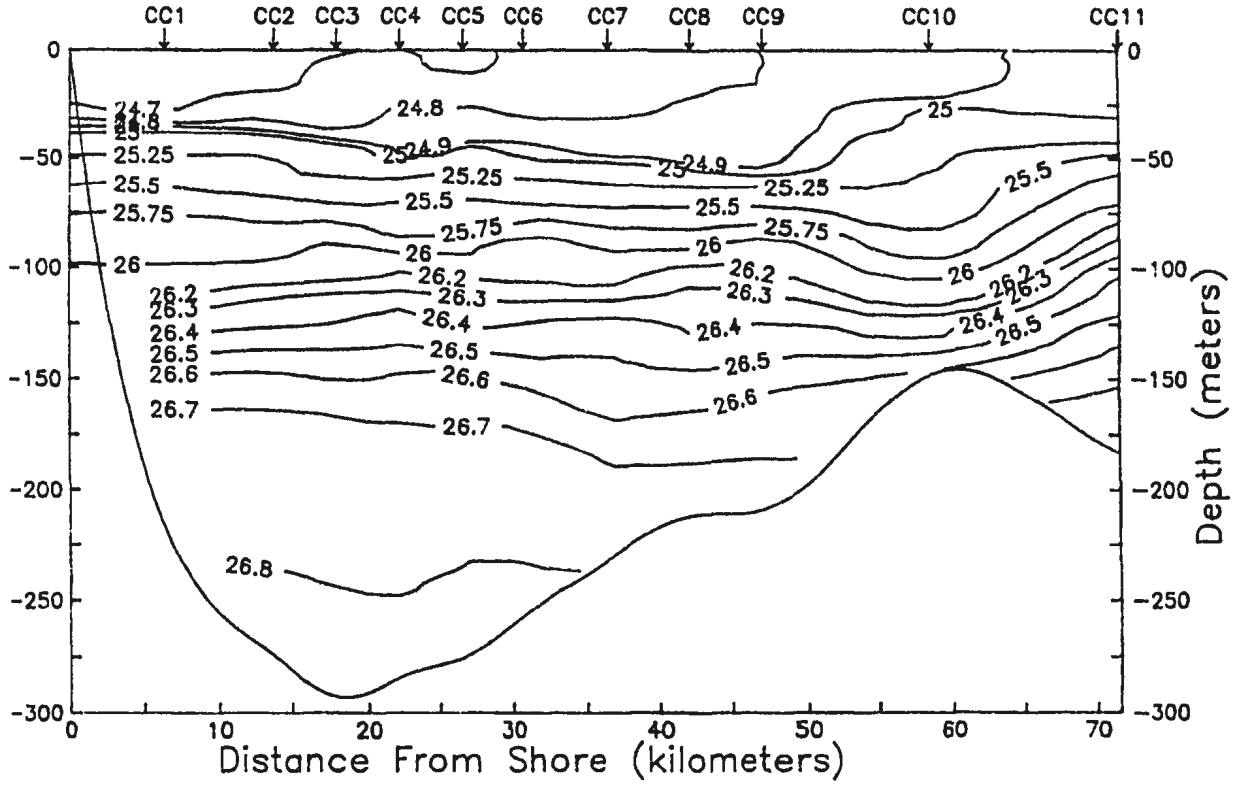

Figure 2.5 Along-bay density field for November 2, 1989 calculated from CTD casts along the CC line shown in Figure 2.2. Densities are given in units of σ_t.

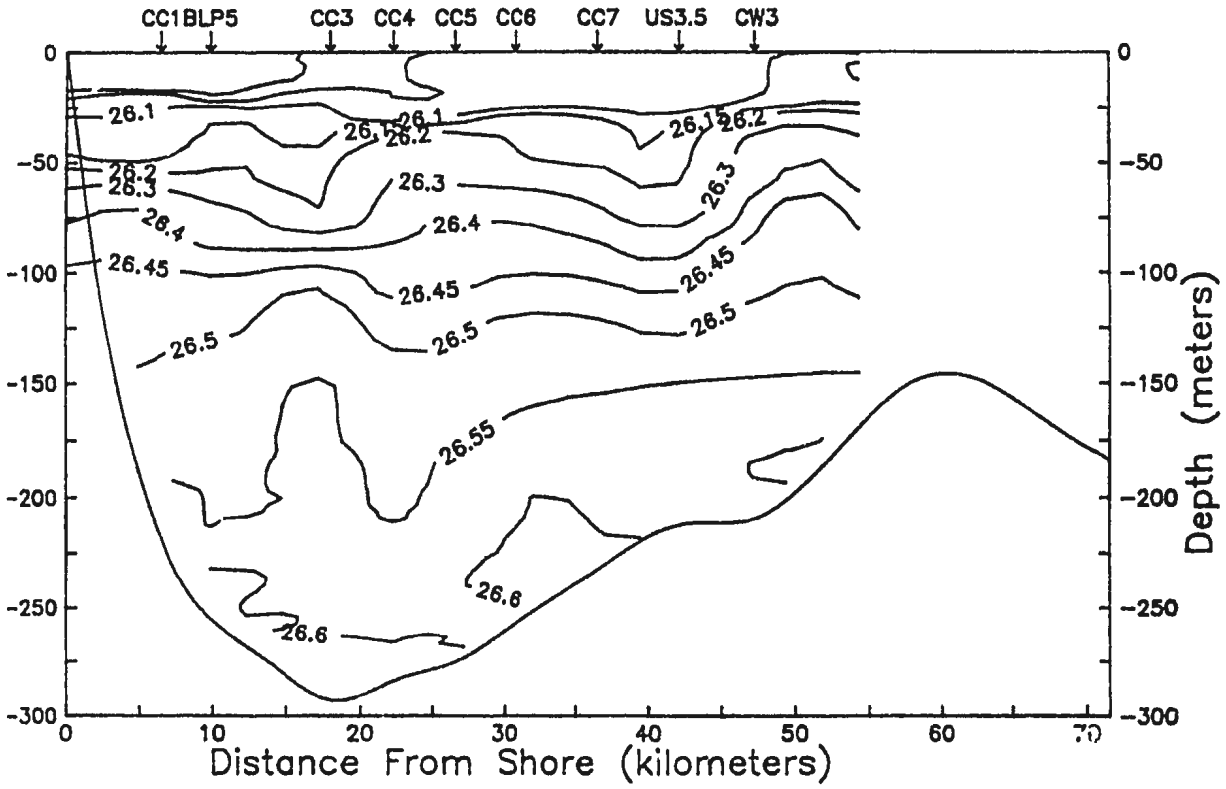

Figure 2.6 Along-bay density field for May 6/7, 1990 calculated from CTD casts along the CC line shown in Figure 2.2. Densities are given in units of σ_t.

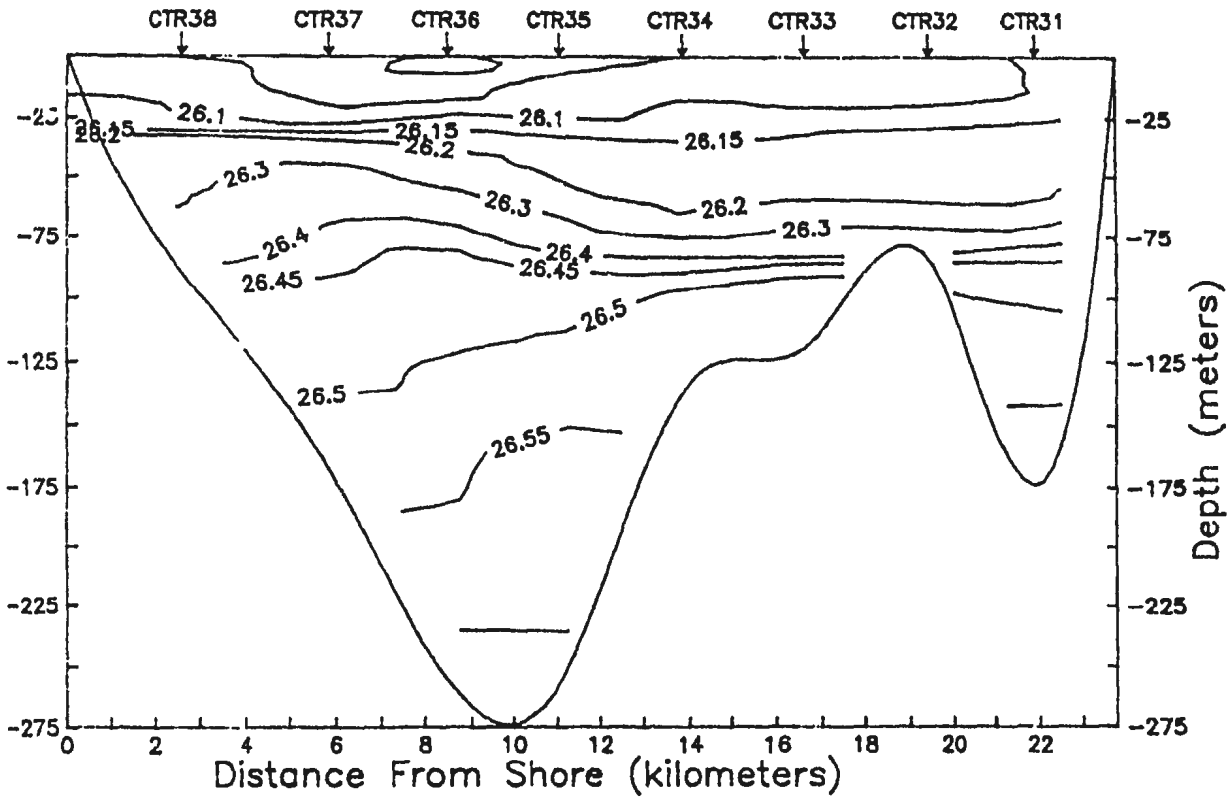

Figure 2.7 Cross-bay density field for May 5, 1990 calculated from CTD casts along the CTR3 line shown in Figure 2.2. Densities are given in units of σ_t. Note that the CTR3 line is shown as the CT3 line in Figure 2.2 due to space constraints.

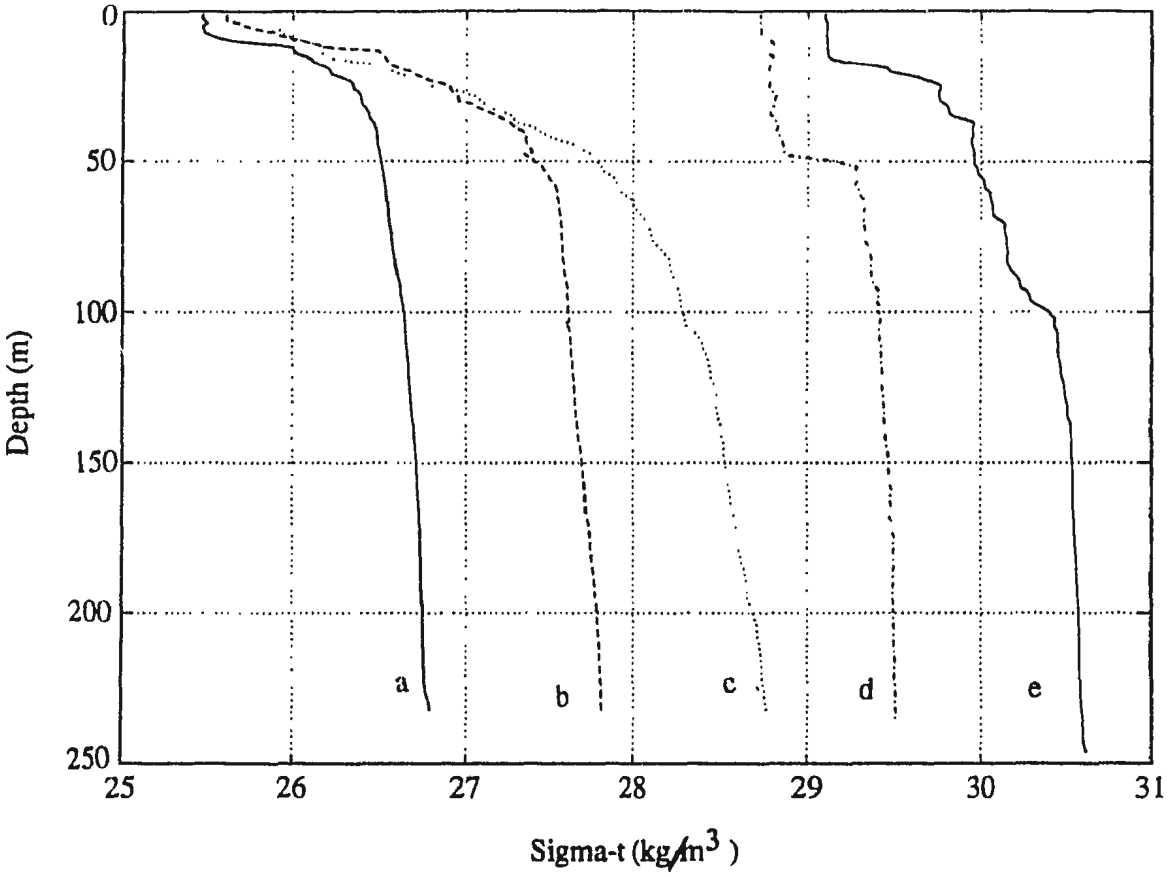

Figure 2.8 Vertical profile of σ_t at station BRLP 5 for five times throughout 1989 and 1990: (a) day 150 of 1989, (b) day 181 of 1989, (c) day 250 of 1989, (d) day 148 of 1990, and (e) day 173 of 1990. For easier comparison, the density profiles are offset by adding 1 kgm^{-3} to curve (b), 2 kgm^{-3} to curve (c), and so on. Note that station BRLP 5 is shown as station BP5 on Figure 2.2 due to space constraints.

and the wind-forcing terms $\tau_x/(\rho H)$ and $\tau_y/(\rho H)$ are added to the right-hand sides of the x and y momentum equations, respectively. In reality, the pycnocline is spread over a range of depths (as shown in Figures 2.3 through 2.8) and the ocean is not infinitely deep. However, the 1-1/2 layer model is still relevant and, in fact, has been used successfully to model wind-driven variability in the Northeast Pacific Ocean (Pares-Sierra and O'Brien (1989) and Johnson and O'Brien (1990a,b)) and in equatorial regions (Busalacchi and O'Brien (1980)). To understand the relevance of the model to Conception Bay, we note that, as was mentioned in the introduction, a uniformly stratified, flat-bottomed ocean can be described by an infinite number of vertical modes, the horizontal structure of each being described by the shallow water equations (i.e. equations (1.4)). The zeroth (barotropic) mode is not sensitive to the density stratification and behaves as in a uniform density ocean with H equal to the ocean depth. For this mode, the vertical structure of the horizontal velocity field is independent of depth. For the higher (baroclinic) modes, the integral over the depth of the ocean equals zero. The first baroclinic mode has one zero crossing with the flow in the lower half of the water column being in the opposite direction to that above. The equations governing the baroclinic modes are the same as those for the 1-1/2 layer model. Usually, the mode dominantly excited by the wind is the first baroclinic mode, but in some regions of the ocean, it is the second baroclinic mode (see Philander and Pacanowski, 1980, for an example). In this thesis, we shall assume that it is the first baroclinic mode that is most important. This assumption is supported by the data in Figures 2.11, 2.16, 2.17, and 2.18 (to be presented in the section 2.3) which show that vertical movement of the isopycnals occurs in the same direction throughout the depth of the Bay, a feature consistent with the

first baroclinic mode. It remains to discuss the likely importance of the variable bottom topography in Conception Bay. The effect of the bottom topography will be felt through the velocity field at the bottom. If the bottom velocities associated with the pycnocline movements in the Bay are weak, then its effect can be safely neglected. This will be the case if the pycnocline is confined near the surface of the Bay. As it happens, observed currents in the Bay are, in general, found to be surface intensified (deYoung and Sanderson, 1992), a feature consistent with the 1-1/2 layer assumption, although scattering of Kelvin waves by bottom topography could still be important. On the other hand, the 1-1/2 layer model used here should give a first-order description of the response of the pycnocline in the Bay to wind. To include bottom topography would require use of a more complicated model (e.g. Anderson and Corry, 1985) and is beyond the scope of this thesis. We choose to investigate the response separated from the topographic influence, as a first step in understanding wind forcing in the Bay.

2.3: Current Meter and Thermistor Chain Data

Figure 2.9 shows the positions of the current meter and thermistor chain moorings deployed from late April to late October of 1989. The moorings were sub-surface and consisted of two Aanderaa current meters, nominally located at 25 m and 100 m at M1-M6. Thermistor chains were placed on M1 and M3-M6 with 11 thermistors distributed between the two current meters. Only the thermistor chains at M3, M4, and M5 were successfully recovered. Only the surface current meters at M2, M3, and M4 were successfully recovered. Unfortunately, the current meter at M4 failed. All Aanderaa current meters had paddle-wheel rotors with vector averaging RCM7 current meters used near the surface and RCM5s

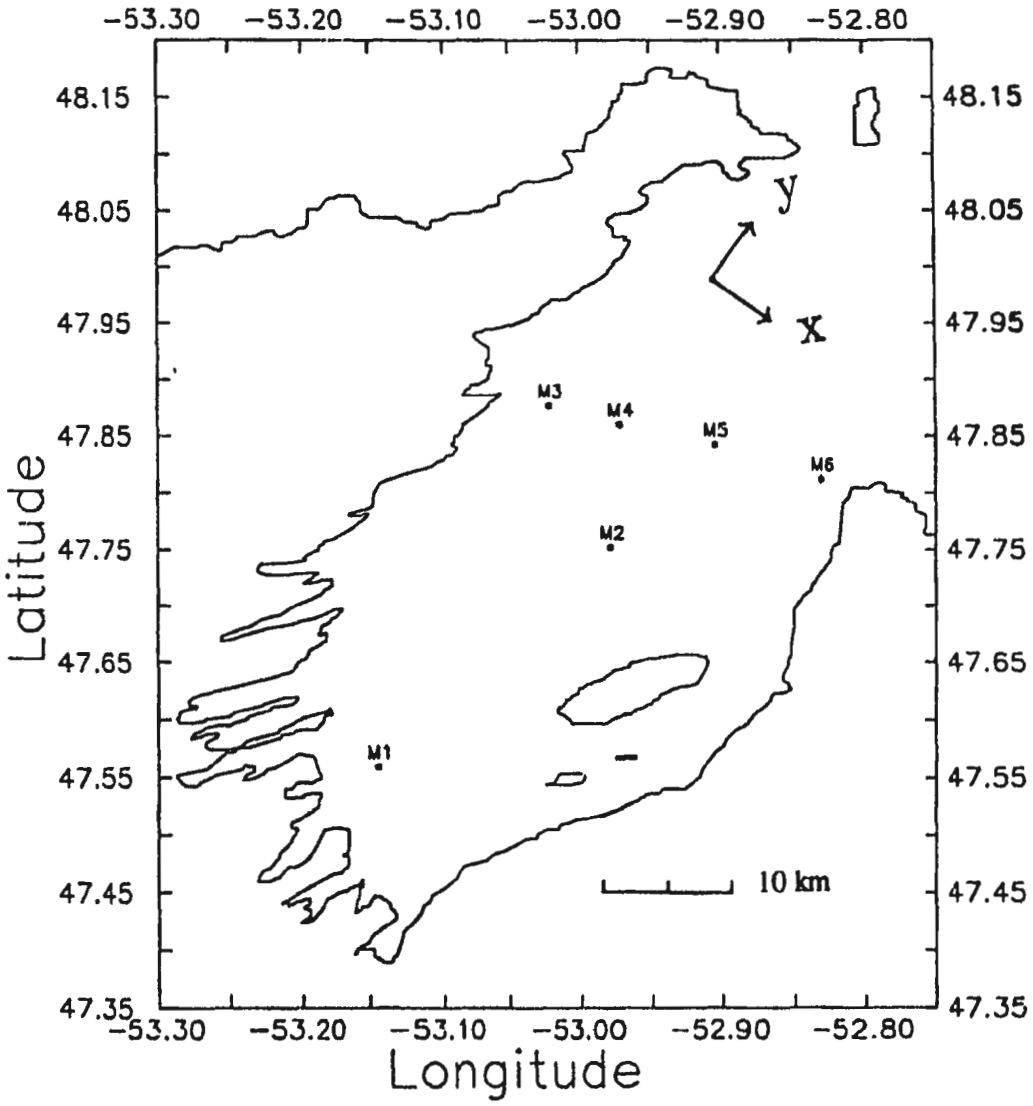

Figure 2.9 Mooring positions for 1989.

at depth. The paddle-wheel rotors are used because they have been shown to minimize the effects of vertical motion on the measured horizontal speed (Hammond et al., 1986). For both the current meters and thermistors, data were collected at hourly intervals.

All of the current meter moorings were recovered in late October of 1989. In the case of current meter data, u and v components have been filtered in the same manner as the wind stress. In order to more easily compare with modelled velocities, all observed currents have been transformed into bay coordinates. Figure 2.10 shows the current and temperature at 25 m at mooring 3. Since the mooring is only 3km from shore, one might expect the velocity component perpendicular to the shore to have considerably less magnitude than the component parallel to the shore. However, principal component analysis has shown that there is no dominant velocity direction at M3.

A plot of temperature versus depth and time is shown in Figure 2.11 using temperatures collected from the thermistor chain at M3. For the thermistor chains, data at each of the 11 depths have been filtered separately. The figure shows that the depth of the thermocline increases considerably during the warming period. The thermocline at mooring 3, which is located ~3 kilometers from the coast, moves vertically as if in response to wind-forcing. Throughout the time series, vertical displacements of the isotherms of 20 m or more dominate the signal. Thermocline movements of ~20 m also dominate the plots of temperature versus depth and time at moorings 4 and 5. Similarity in the amplitude of the vertical movement between moorings 3, 4 and 5 is not consistent with the simple theory describing the wind-forced response of a bay. This theory predicts that the amplitude of the vertical

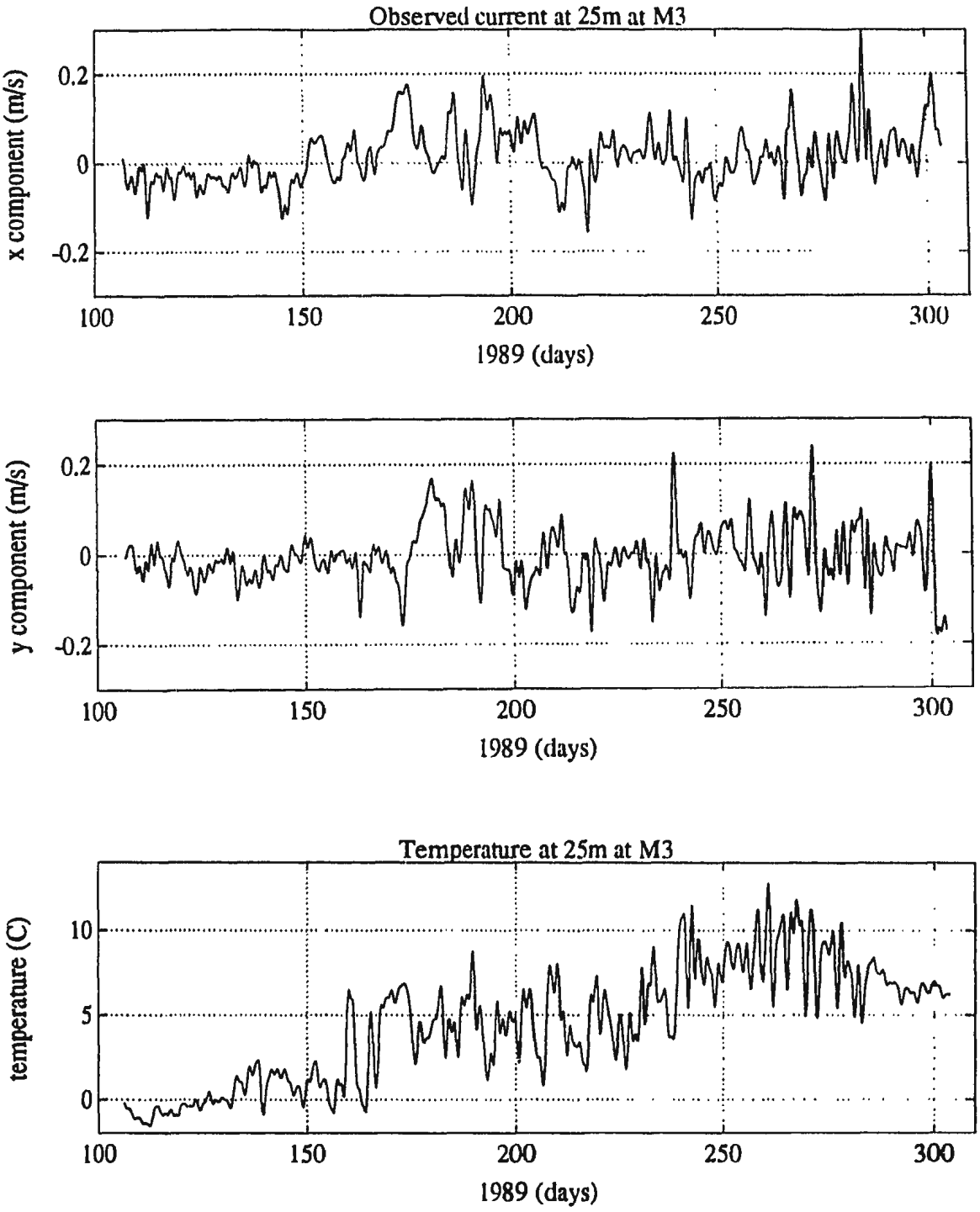

Figure 2.10 Current (in ms^{-1}) and temperature (in °C) at ~25 m at mooring 3 for 1989

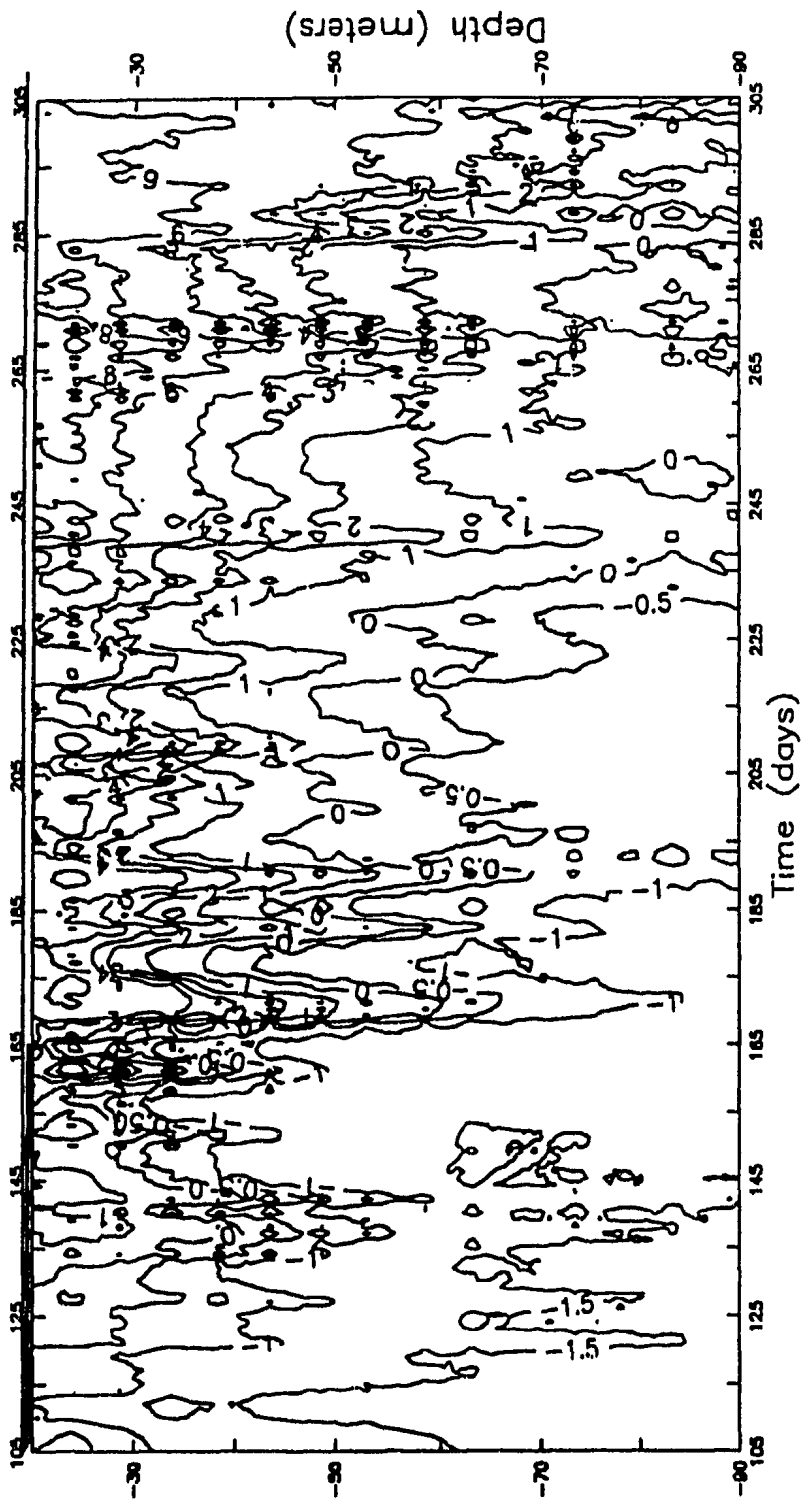

Figure 2.11 Temperature (in °C) vs depth (in meters) and time (in days) at mooring 3 for 1989

motion of the pycnocline/thermocline should decay exponentially away from the coast on the order of the internal Rossby radius, which is roughly 5 km.

In 1990, moorings were deployed in late April and recovered in late July at the six positions shown in Figure 2.12. As in 1989, the moorings were sub-surface and consisted of two current meters, one at approximately 25 m and another at approximately 85 m on all of the six moorings. Thermistor chains were placed on M2-M6 with 11 thermistors distributed between the two current meters. Aanderaa RCM7s were used at 25 m at moorings 1 and 3, while InterOcean S4s were used at 25 m for moorings 2, 4, 5 and 6. All of the bottom current meters were Aanderaas, either RCM5 or RCM7 (vector averaging meters). All of the Aanderaa current meters were equipped with paddle-wheel rotors. The Aanderaa RCM7s collected data at 15 minute intervals, while the S4s and the thermistors collected data at 30 minute intervals.

In 1990, all of the instruments were successfully recovered. Data recovery was about 90% with the thermistor chain at M3 malfunctioning. Figures 2.13, 2.14, and 2.15 show time series of the current and temperature at M1, M3 and M6. As in the 1989 data, the velocities are relative to bay coordinates. Principal component analysis of the currents shows that currents at M1, M2, and M3 have a strong, directional bias parallel to the coastline, while currents at M4, M5, and M6 exhibit virtually no directional bias. The similarity of the temperature signal between M1 and M3 after 170 days suggests that information is propagating around the head of the bay. Several events characteristic of upwelling and relaxing of the pycnocline are present in the temperature signals at M1 and M3 at 175, 185, 190, and 197 days. Note that upwelling events occur before 170 days, but will not

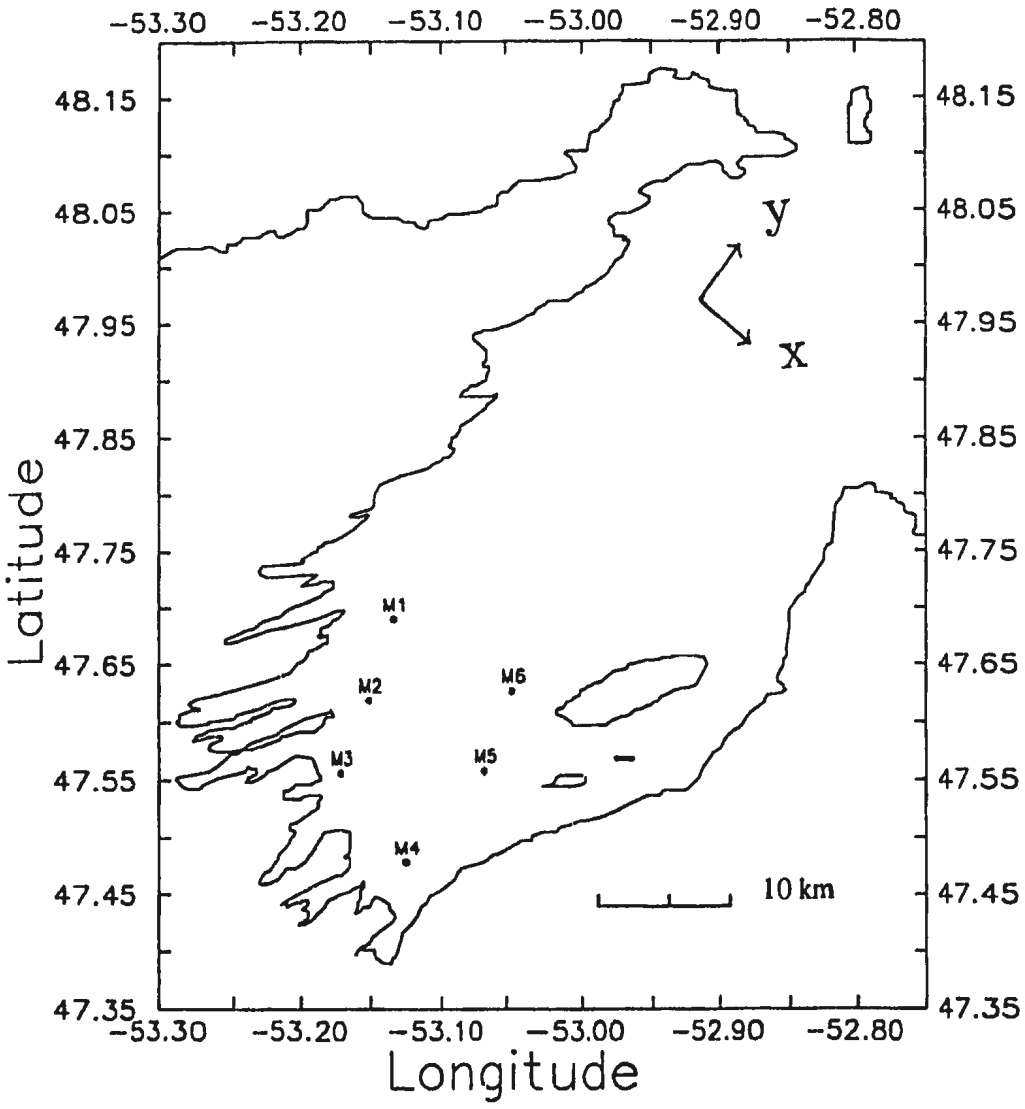

Figure 2.12 Mooring positions for 1990

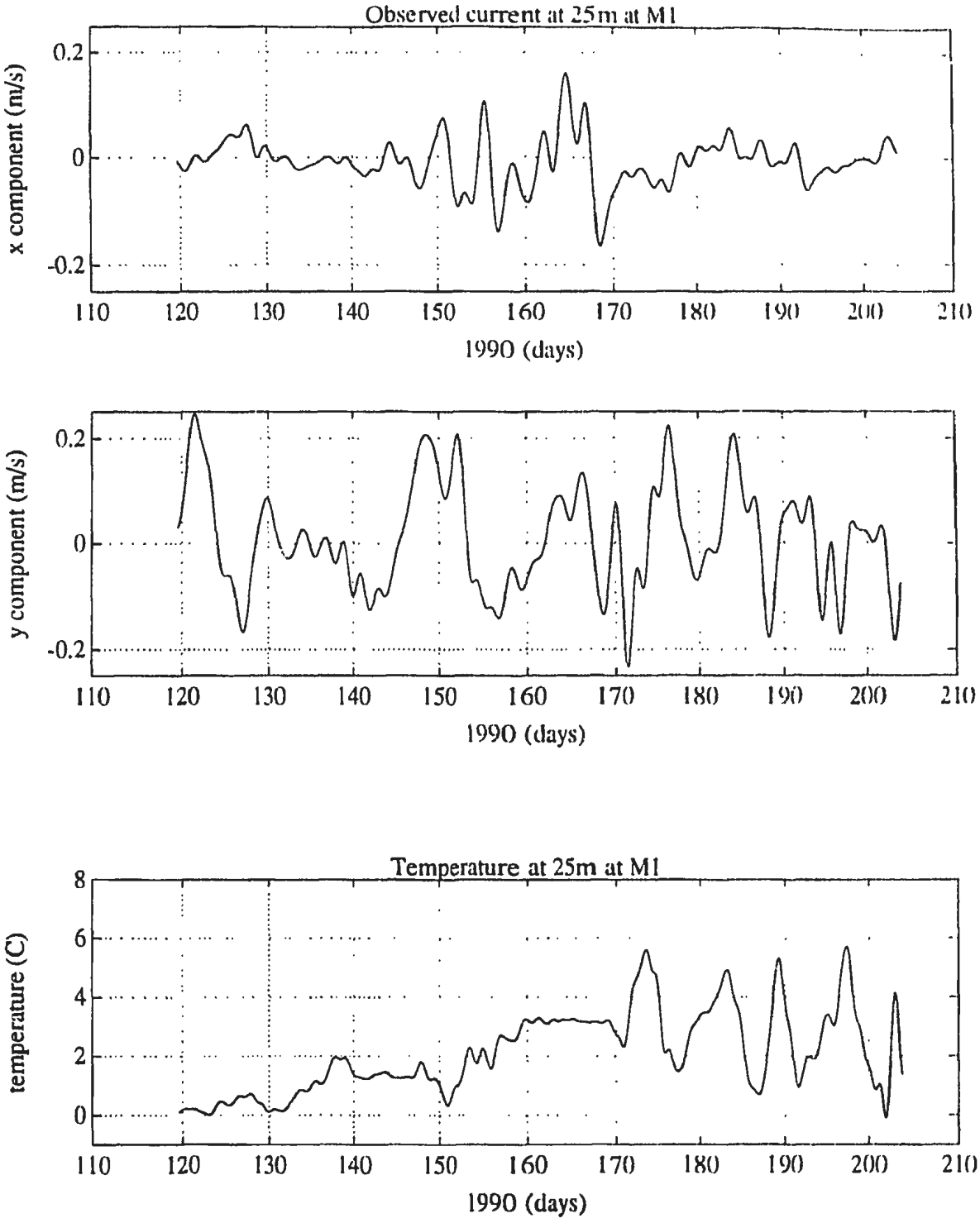

Figure 2.13 Current (in ms^{-1}) and temperature (in °C) at ~25 m at mooring 1 for 1990

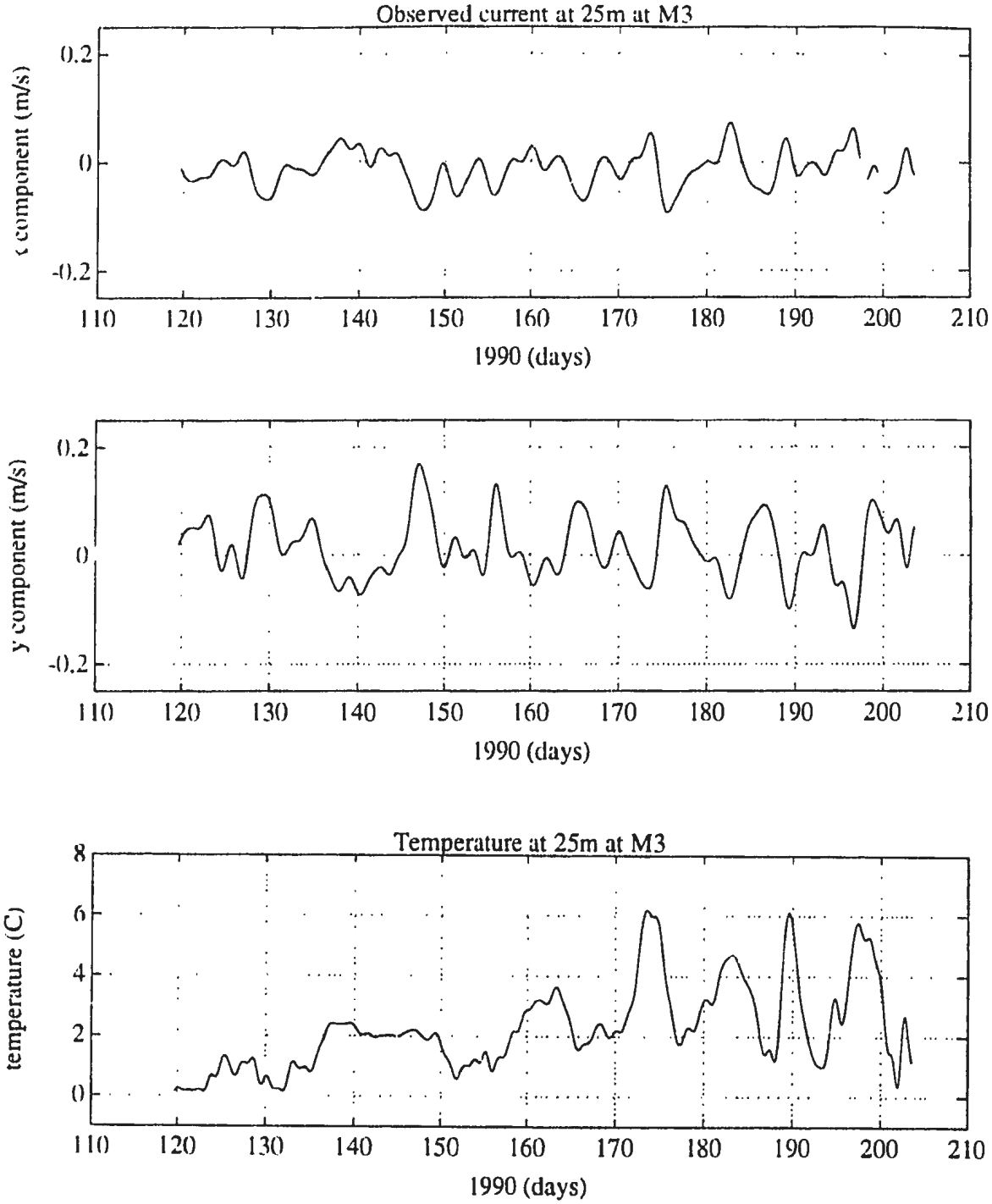

Figure 2.14 Current (in ms^{-1}) and temperature (in °C) at ~25 m at mooring 3 for 1990

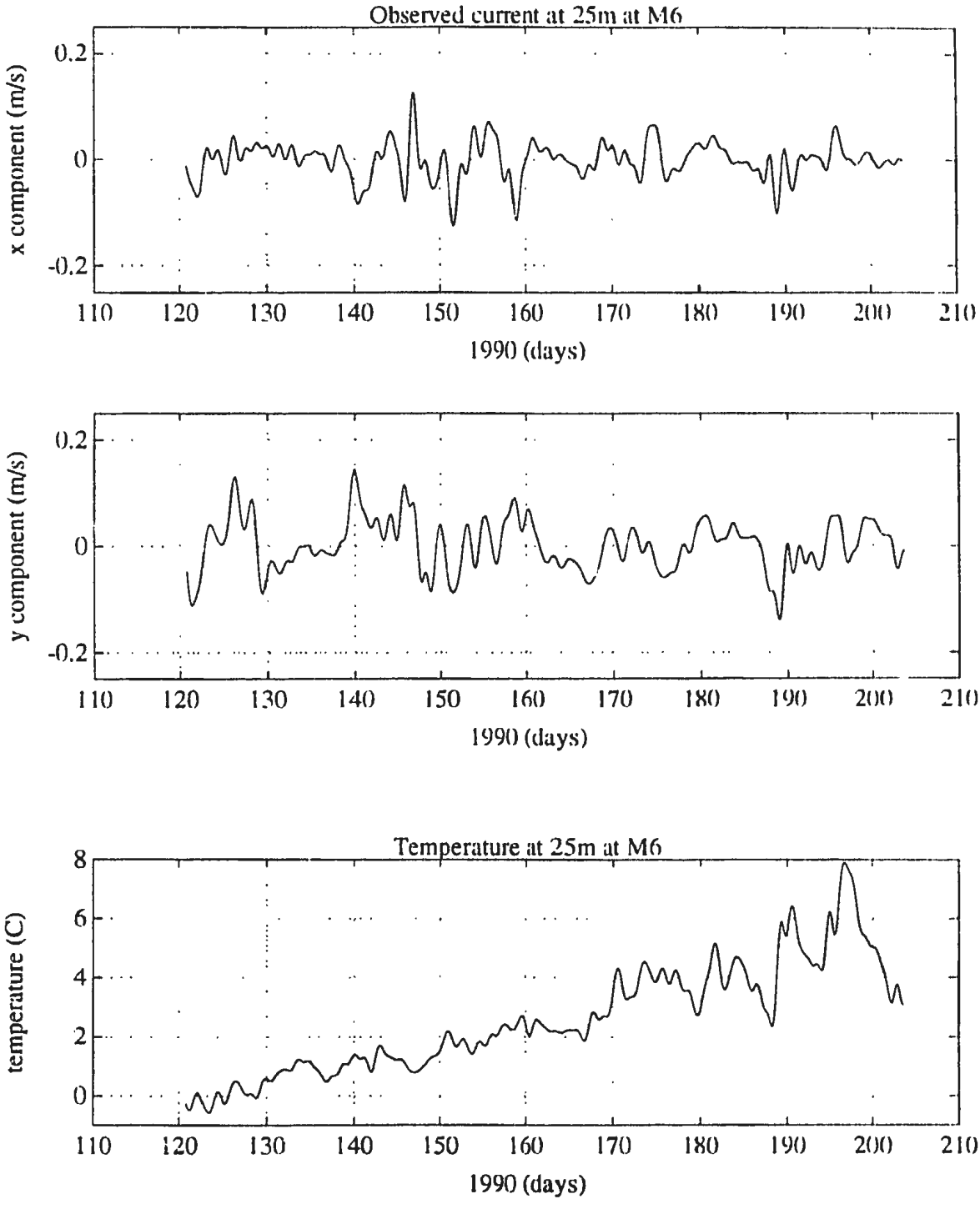

Figure 2.15 Current (in ms^{-1}) and temperature (in °C) at ~25 m at mooring 6 for 1990

be addressed in detail, because the temperature measurement at M1 from 160 to 168 days is doubtful. A constant temperature of 3°C was recorded implying that some part of the data acquisition system malfunctioned during this period. Due to its two-dimensional nature, similarity in the current field is more difficult to pick out, but is apparent in the v components of M1 and M3 after day 160.

Figures 2.16, 2.17, and 2.18 show temperature versus depth and time as recorded by the thermistor chains at M2, M4 and M6. The similarity in the temperature signals evident in the temperature plots at M1, M3 and M6 is present in Figures 2.16, 2.17, and 2.18 as well, especially between M2 and M4. The drop in temperature present at days 175, 185, 190, and 197 in Figures 2.13 and 2.14 corresponds to rapid upward motion of the thermocline in Figures 2.16 and 2.17.

2.4: Suspected Wind-Forced Response

The data presented in this chapter exhibit certain features characteristic of a wind-forced response. In particular, the similar behavior at neighboring stations near the head in 1990 is an indication that the Bay is responding to wind forcing.

The mooring positions for the year 1990 present an excellent opportunity for the study of wind-forced Kelvin waves propagating along the pycnocline. Figure 2.19 shows the temperatures recorded at the six current meters at ~25 m at the head of the bay in 1990 (see Figure 2.12 for mooring positions in 1990). Signals at M1-M4 are nearly identical after day 170, except for slight phase lags present that indicate propagation around the bay. The signals at M5 and M6 exhibit similar behavior, but are corrupted before day 185 possibly

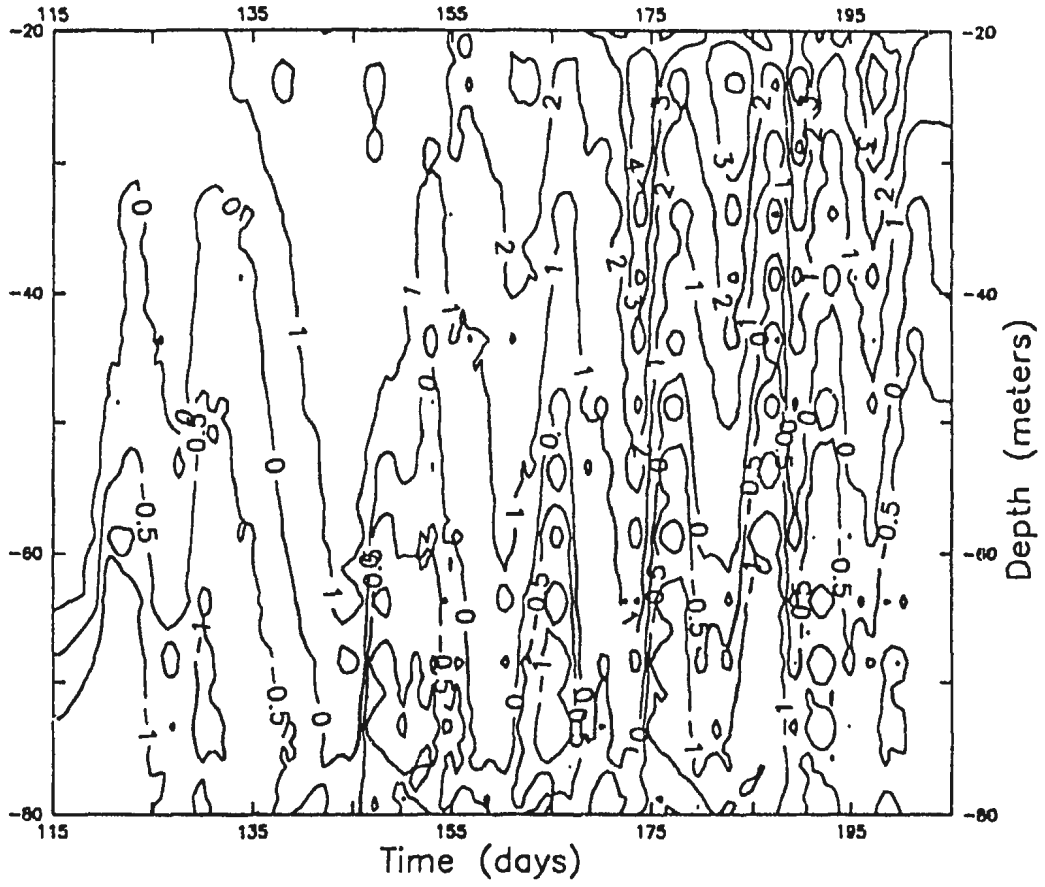

Figure 2.16 Temperature (in °C) vs depth (in meters) and time (in days) at mooring 2 for 1990

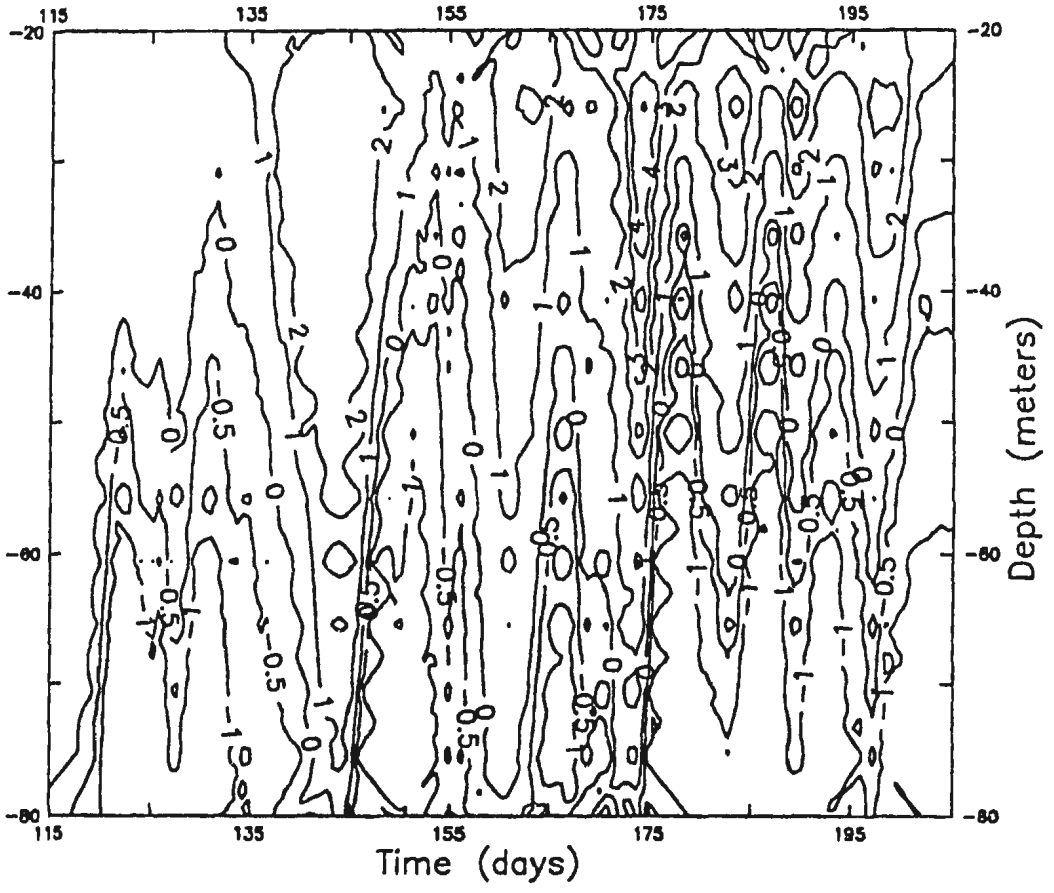

Figure 2.17 Temperature (in °C) vs depth (in meters) and time (in days) at mooring 4 for 1990

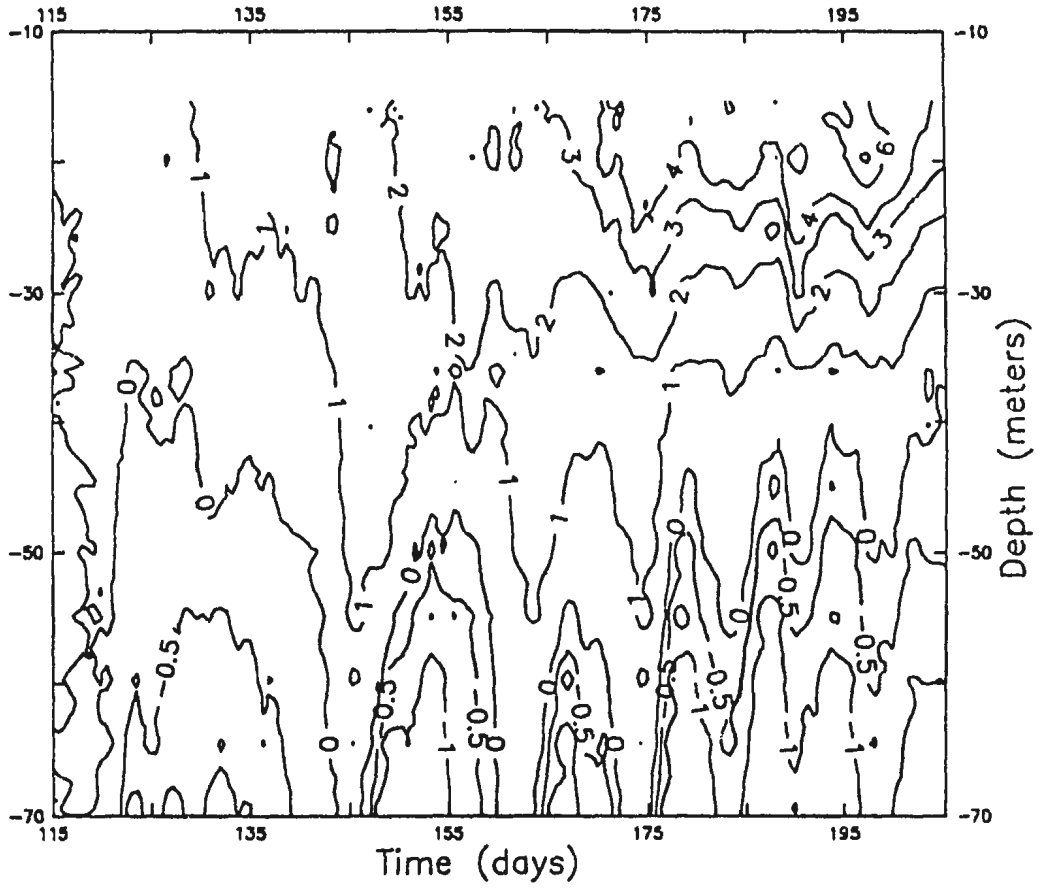

Figure 2.18 Temperature (in °C) vs depth (in meters) and time (in days) at mooring 6 for 1990

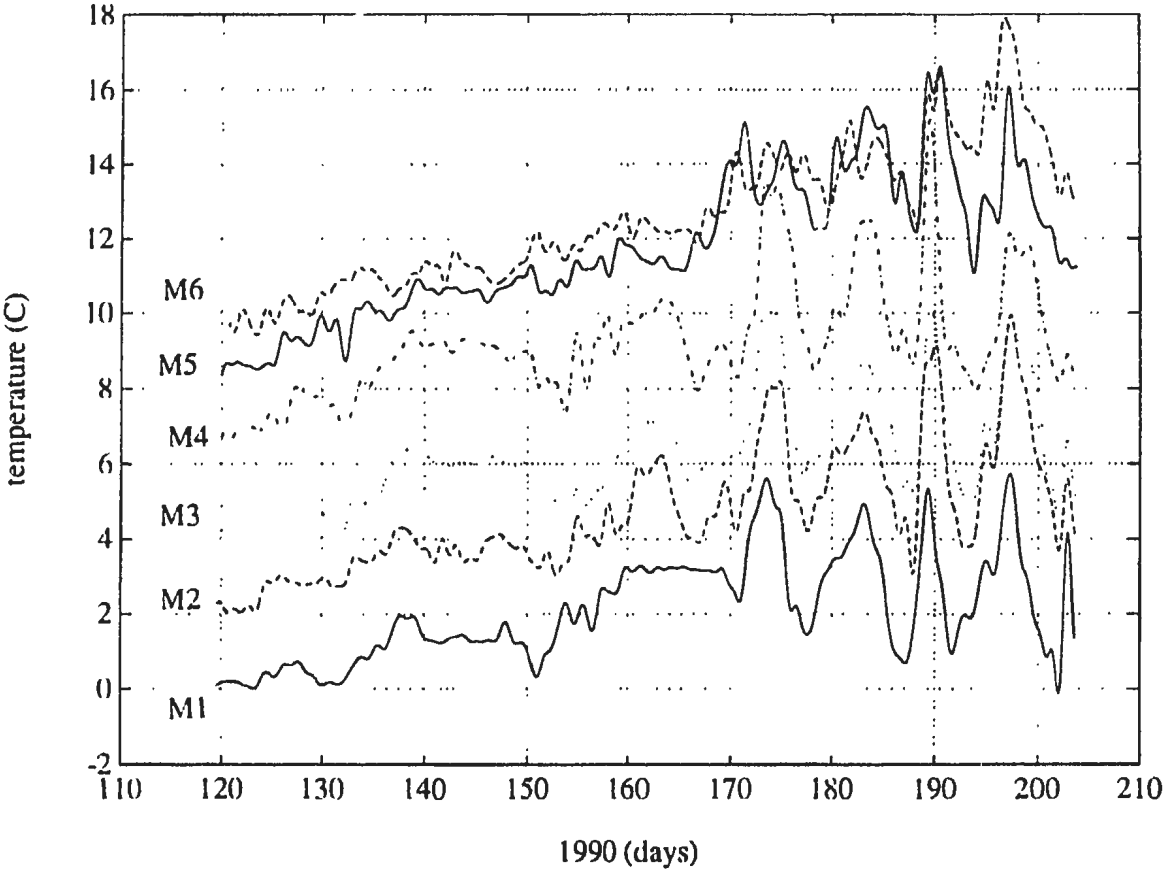

Figure 2.19 Temperatures (in °C) at ~25 m at the 6 current meters for 1990. For easier comparison, 2°C has been added to the temperature at M2, 4°C added to the temperature at M3, and so on.

by their location relative to the shallow region in Bell Island Tickle (see Figure 1.2). Comparison with the wind in Figure 2.1 suggests a correlation between a southwesterly wind and a decrease in temperature in the upper layer at the head of the bay.

Spectral analysis can be used to quantify the amount of agreement between two time series. Figure 2.20 shows the cross-spectrum between the temperatures at 25 m at M2 and M3 in 1990 for the period 170-203 days. The details of the spectral analysis used will be discussed further in Chapter 4. Notice that in Figures 2.20a and 2.20b filtering has greatly reduced the energy at frequencies greater than 1 cpd. Figure 2.20c shows the difference in phase between the temperature signals at M2 and M3. Figure 2.20d shows the (coherence)^2 between the two time series. The spectrum has 12 degrees of freedom. Values of (coherence)^2 greater than 0.6 mean that coherence between the signals is significant with 90% confidence. Figure 2.20 shows that temperatures at M2 and M3 agree with one another, at least at low frequencies, as is to be expected from Figure 2.19. Figure 2.21 shows the same analysis repeated for M3 and M4. Again, agreement between the two series is high.

The moorings (M3, M4 and M5) for 1989 provide data at the mouth of the bay (see Figure 2.9). While propagation of information (at least by Kelvin waves) cannot be checked using these data, the data do provide an opportunity to analyze the expected decay of the wind-forced response with distance from the coast and the influence of regions outside the bay.

The similarity of structure apparent in the 1990 data is not as obvious in the 1989 data. Figure 2.22 shows the temperature at approximately 25 m at moorings 3, 4, and 5 as recorded by the thermistor chains, as well as the wind stress. The signals at the neighboring

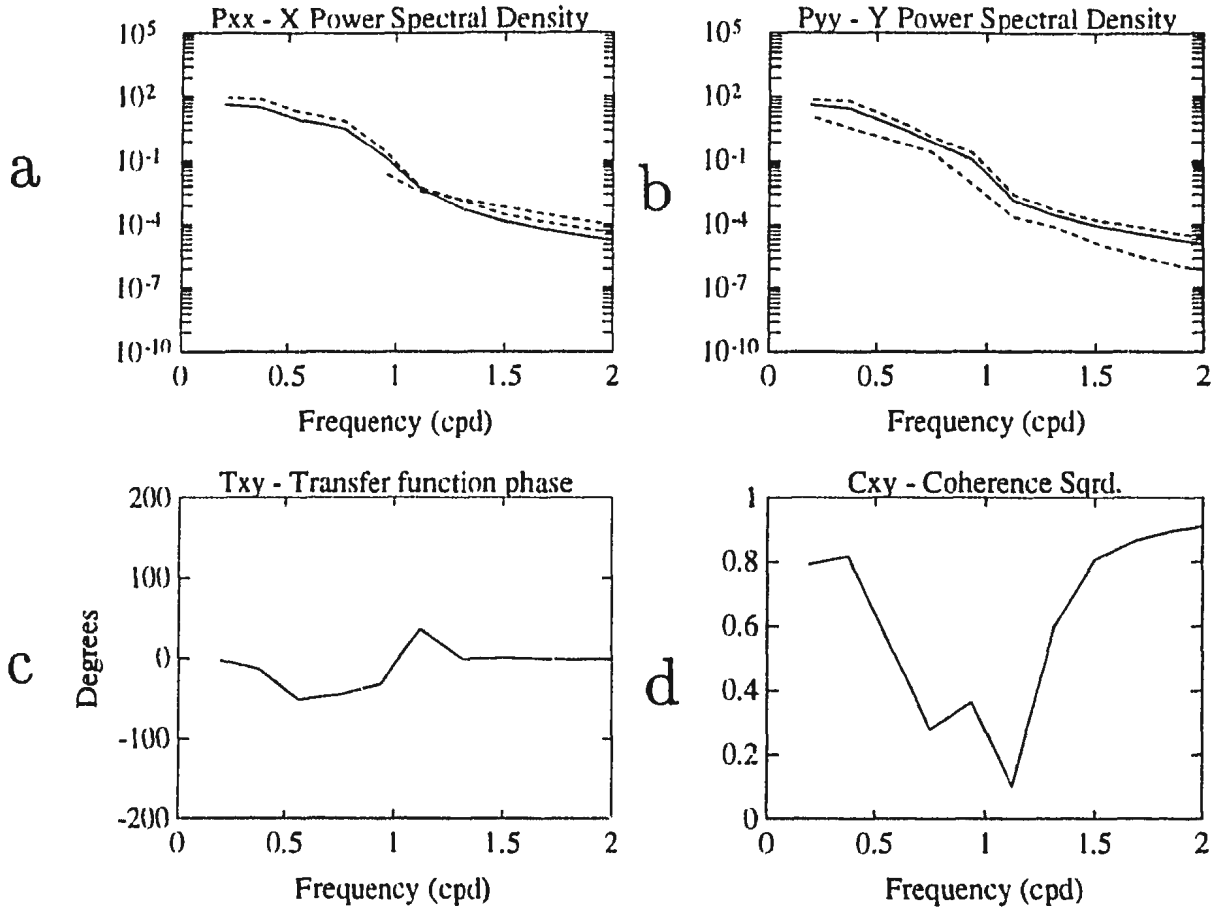

Figure 2.20 Cross-spectrum for temperatures at ~25m at M2 and M3 for 170-203 days in 1990. Spectrum has 12 degrees of freedom, and values of (coherence)^2 greater than 0.56 are significant at the 90% confidence level. (a) Power spectrum of temperature at M2. (b) Powerspectrum of temperature at M3. (c) Phase difference between temperature at M2 and M3 (d) (Coherence)^2 between the two time series.

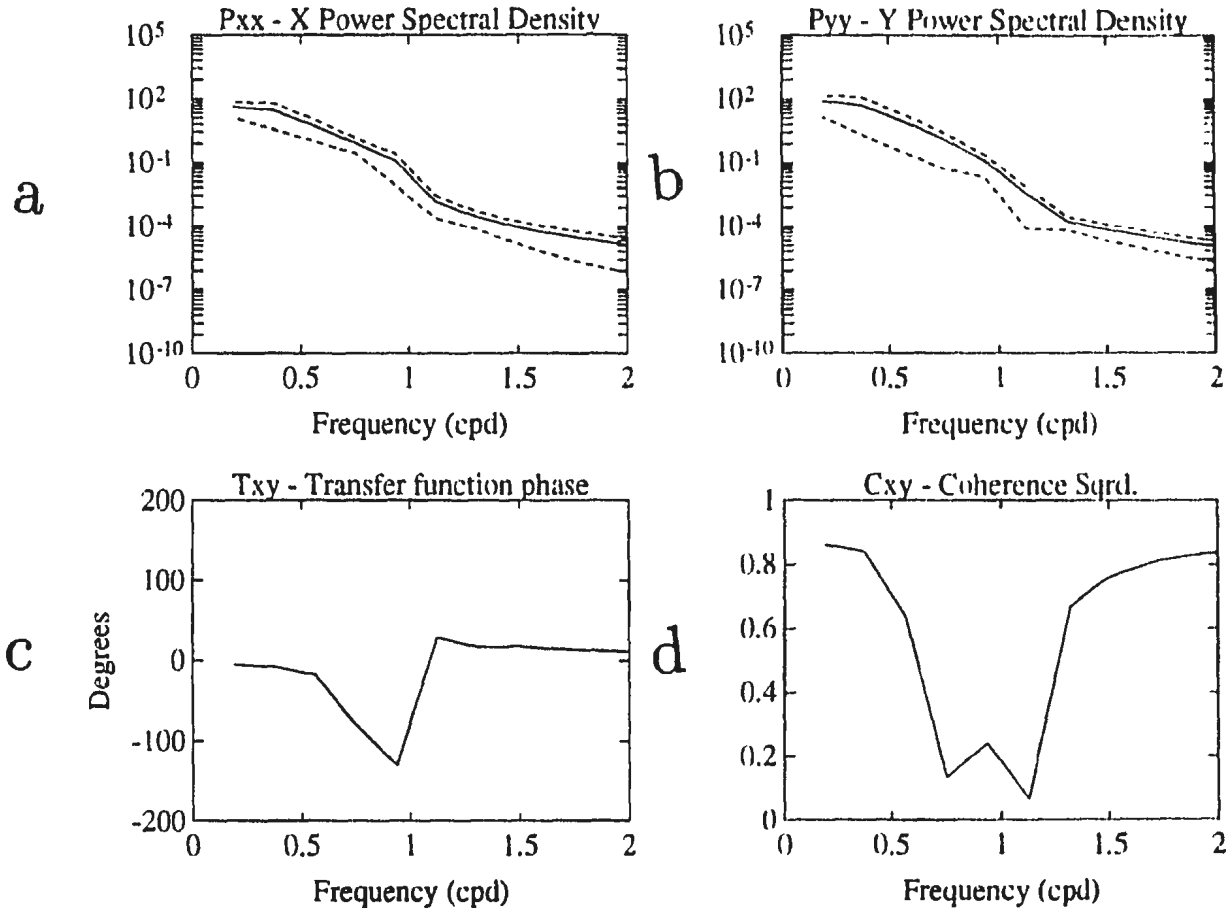

Figure 2.21 Same as Figure 2.20, except cross-spectrum is computed for M3 and M4, instead of M2 and M3.

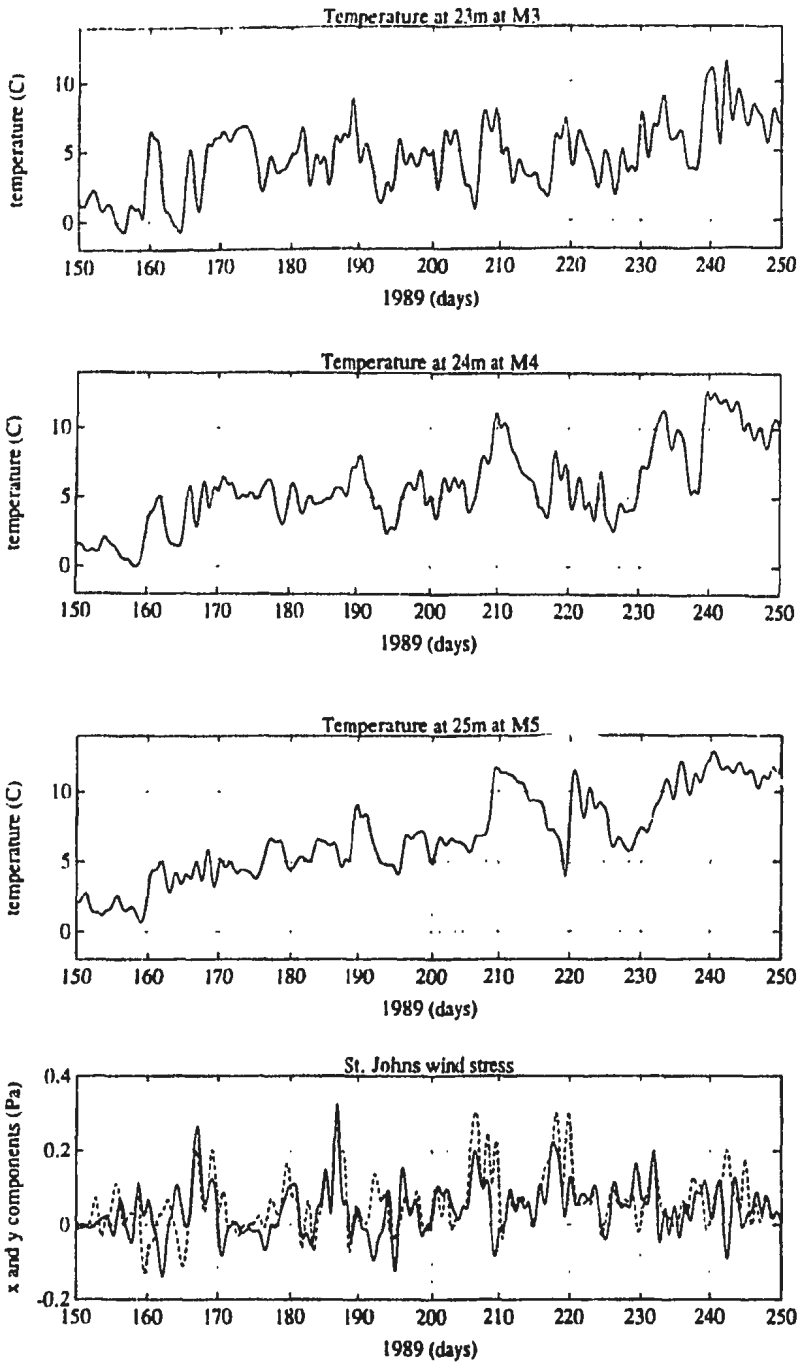

Figure 2.22 Temperature (in °C) at ~25 m at moorings 3, 4, and 5 in 1989 and St. John's wind stress (in Pa). In the wind stress plot, the solid line represents the x-component of wind stress, and the dashed line represents the y-component.

stations appear to have many of the same events, but overall the agreement is much poorer than between the 1990 stations at the head. The poor coherence is reflected in cross spectra between the temperature at 1989 stations. Comparison of temperature with the wind stress does not show any obvious correlations.

In chapter 4, observed data and model output will be analyzed to determine the processes behind the upper-layer movement. In particular, spectral analysis will be performed on the wind data, observed current data, and model current output to determine the role of the wind on observed currents. Modelled pycnocline displacement will be compared to observed temperatures and pycnocline movement. Analysis of data at the mouth and head of the bay will be used to show the effect of outside influences on the upper layer of the bay.

CHAPTER 3: THE MODEL

3.1: Equations of Motion

A 1-1/2 layer model is used to approximate the upper layer of the Bay. The 1-1/2 layer model is composed of a less-dense fluid, ρ_1, resting on a more dense fluid, ρ_2. The upper layer is assumed to be well-mixed, incompressible, and homogeneous and is taken to have a uniform undisturbed depth of H_1. The finite jump in density between the two layers represents the pycnocline in the real ocean. Downwards displacement of this interface is measured by η. The lower layer is homogeneous, infinitely deep and at rest. Since the upper layer is well-mixed and of uniform density, the velocity at a point in horizontal space is independent of depth. With these simplifications and neglecting non-linear effects, the equations of motion for the upper layer on an f-plane simplify to these three equations

$$\frac{\partial u}{\partial t} - fv = -g'\frac{\partial \eta}{\partial x} + \frac{\tau^x}{\rho_1 H_1}, \tag{3.1}$$

$$\frac{\partial v}{\partial t} + fu = -g'\frac{\partial \eta}{\partial y} + \frac{\tau^y}{\rho_1 H_1}, \tag{3.2}$$

$$\frac{\partial \eta}{\partial t} + H_1\left(\frac{\partial u}{\partial x} + \frac{\partial v}{\partial y}\right) = 0, \tag{3.3}$$

where (τ^x, τ^y) is the surface wind stress, and f is the Coriolis parameter. $f = 2\Omega sin\phi$, where ϕ is latitude and Ω is the Earth's angular velocity, and is equal to $1 \times 10^{-4}s^{-1}$ for Conception Bay. It should be noted that for a mid-latitude bay the size of Conception Bay the f-plane approximation is clearly appropriate.

In developing the numerical model, the question of what open boundary formulation to apply at the mouth of the bay must be addressed. This is discussed in depth in this chapter. For now, values of $g' = 10^{-2}$ ms^{-2} and $H_1 = 50$ m are selected. By choosing

these values, we are attempting to mimic summer conditions in Conception Bay, when the stratification is the strongest. For these values, the propagation speed of internal Kelvin waves and the maximum group velocity of Poincaré waves is $(g'H_1)^{1/2} = 0.7$ ms^{-1}. The Rossby radius of deformation is 7 km and is roughly 1/6 of the width of the bay. This means that rotation plays a big role in the dynamics on time scales longer than a few hours and is an important consideration in the design of the boundary conditions to be applied at the mouth. All the experiments we describe in this chapter use a spatially uniform wind stress (either northward or westward) of magnitude 0.05 Nm^{-2} unless otherwise specified.

3.2: C-Grid

For computational efficiency, an Arakawa C-grid (shown in Figure 3.1) is used. Δx and Δy are the grid spacings. The Arakawa C-grid facilitates the calculation of centered spatial differences. For example, η_x is required to find u_t in Equation 3.1. Using the C-grid shown above, a second order accurate approximation of η_x at the u point $(i+\frac{1}{2}, j)$ is equal to $(\eta_{i+1,j} - \eta_{i,j})/\Delta x$.

3.3: Stepping Forward in Time

u, v, and η are given values (typically zero) at time $t = 0$ at their respective locations on the C-grid. Equations 3.1-3.3 are used to update these values. The model uses a method suggested by Sielecki (1968) for an E-grid and modified by Heaps (1971) to fit the C-grid. In discretized form, Equations 3.1-3.3 are

$$\eta_{i,j}^{n+1} = \eta_{i,j}^{n} - H_1 \Delta t \left(\left(u_{i+\frac{1}{2},j}^{n} - u_{i-\frac{1}{2},j}^{n} \right)/\Delta x + \left(v_{i,j+\frac{1}{2}}^{n} - v_{i,j-\frac{1}{2}}^{n} \right)/\Delta y \right), \qquad (3.4)$$

$$u_{i+\frac{1}{2},j}^{n+1} = u_{i+\frac{1}{2},j}^{n} + \frac{f\Delta t}{4}\left(v_{i+1,j+\frac{1}{2}}^{n} + v_{i,j+\frac{1}{2}}^{n} + v_{i+1,j-\frac{1}{2}}^{n} + v_{i,j-\frac{1}{2}}^{n} \right)$$

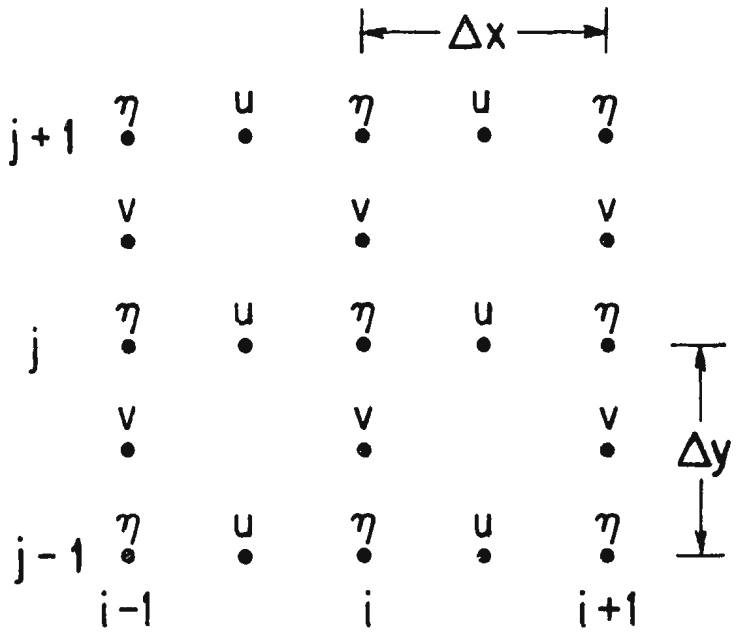

Figure 3.1 The Arakawa C-Grid

$$-\frac{g'\Delta t}{\Delta x}(\eta^{n+1}_{i+1,j} - \eta^{n+1}_{i,j}) + \frac{\tau^x \Delta t}{\rho_1 H_1}. \tag{3.5}$$

$$v^{n+1}_{i,j+\frac{1}{2}} = v^{n}_{i,j+\frac{1}{2}} - \frac{f\Delta t}{4}\left(u^{n+1}_{i+\frac{1}{2},j} + u^{n+1}_{i+\frac{1}{2},j+1} + u^{n+1}_{i-\frac{1}{2},j} + u^{n+1}_{i-\frac{1}{2},j+1}\right)$$

$$-\frac{g'\Delta t}{\Delta y}(\eta^{n+1}_{i,j+1} - \eta^{n+1}_{i,j}) + \frac{\tau^y \Delta t}{\rho_1 H_1}. \tag{3.6}$$

where n denotes the present time level and $n+1$ denotes one time step, Δt, in the future. Note that in calculating the Coriolis term in Equation 3.5, the 4 neighboring values of v are averaged. Likewise in Equation 3.6, the 4 neighboring values of u are averaged to calculate the Coriolis term. η, u and v are updated using (3.4) (and appropriate boundary conditions) to first update all new values of η, followed by the use of (3.5) to update all u values, and lastly, all v values are updated using (3.6). Forward time differencing is used in (3.4) and backward time differencing in (3.5) and (3.6), with the exception of the Coriolis term in (3.5), which uses forward time differencing. In this way, η, u and v are all known at the same time.

The grid spacing must be chosen so that the Rossby radius of deformation ($a = c/f$) is well-resolved by the grid (Hsieh et al., 1983). Hsieh et al. show that to accurately resolve a free Kelvin wave on a C-grid, the grid spacing should be at most the size of the Rossby radius and that the accuracy will improve as the grid spacing decreases relative to the Rossby radius. The Rossby radius will be 7 km for the experiments used in this chapter for determining the appropriate boundary conditions and will always be larger than 4 km for all simulations presented in this thesis; therefore, a grid spacing of 1 km in both the x and y directions is chosen.

To ensure computational stability, the value of Δt must be chosen so that

$$\sqrt{2}c\frac{\Delta t}{\Delta s} \leq 1. \tag{3.7}$$

where $c = (g' H_1)^{1/2}$ and Δs is the smallest grid spacing used (i.e. Δs = 1 km in all cases) (Mesinger and Arakawa, 1976). For the experiments used in determining the boundary conditions, a time step of 1000 seconds is used which is less than the maximum allowed time step of 1100 seconds set by the wave speed of 0.7 ms^{-1}. The choice of the time step to be used in the modelling of Conception Bay in response to realistic wind forcing will be discussed in a later section.

3.4: Land Boundaries

In order to model ocean regions with complex geometries, a method must be developed to designate what grid points are land and what are water. The simplest case is an enclosed, square basin with sides of length L. To ensure that flow normal to the closed boundaries is not allowed, u points are placed along the lines $x = 0$ and x = L, and v points are placed along the lines $y = 0$ and y = L. Values of velocity at these points are set to zero and not updated. u, v and η inside the boundaries are updated as described in section 3.3.

To model more complicated regions, the masking arrays $Umask$ and $Vmask$ are used. $Umask$ is defined at u points, while $Vmask$ is defined at v points. H values are defined at the points in between u values and v values (see Figure 3.2). The coastline of the bay is represented by the values in the H-array. H values equal to 10 represent water, and H

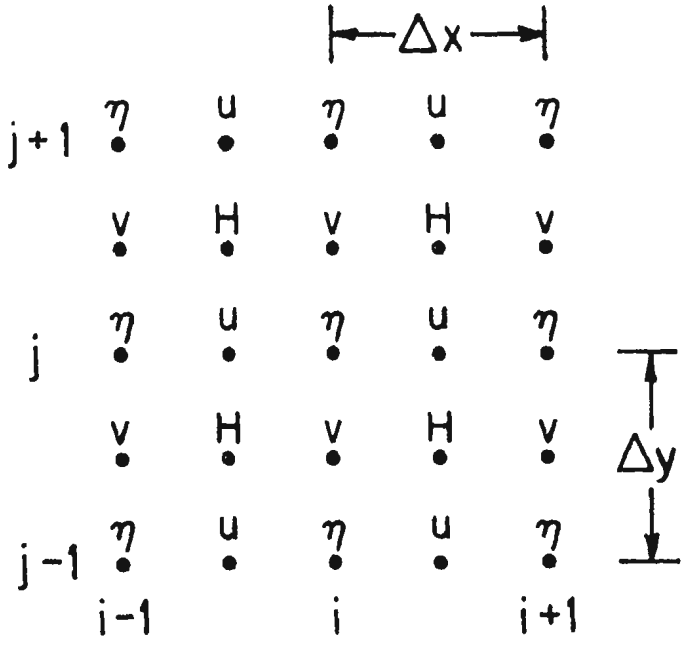

Figure 3.2 C-grid with H-array used in masking velocities

values equal to 1 represent land. $Umask$ and $Vmask$ are calculated from the H-array using the following equations

$$Umask_{i+\frac{1}{2},j} = \begin{cases} 1. & \text{if } \left(H_{i+\frac{1}{2},j-\frac{1}{2}} + H_{i+\frac{1}{2},j+\frac{1}{2}}\right)/2 > 1.0 \\ 0. & \text{otherwise.} \end{cases} \tag{3.8a}$$

$$Vmask_{i,j+\frac{1}{2}} = \begin{cases} 1. & \text{if} \left(H_{i+\frac{1}{2},j+\frac{1}{2}} + H_{i-\frac{1}{2},j+\frac{1}{2}}\right)/2 > 1.0 \\ 0. & \text{otherwise.} \end{cases} \tag{3.8b}$$

η, u and v are integrated as before except that now newly calculated $u_{i+\frac{1}{2},j}$ are multiplied by $Umask_{i+\frac{1}{2},j}$ and newly calculated $v_{i,j+\frac{1}{2}}$ are multiplied by $Vmask_{i,j+\frac{1}{2}}$. η values are updated as before with no masking required.

3.5: Boundary Condition Requirements

To determine the proper boundary conditions, the simple geometry shown in Figure 3.3 is chosen; that is, a 40 km square bay on a straight coastline. This idealized bay has dimensions similar to Conception Bay. The objective is to calculate the response of the bay to wind forcing over the bay. We are not concerned with the response of the bay to disturbances propagating in from outside. In particular, it is clear that coastal Kelvin waves can propagate into the bay from the west, but such influences will not be considered. Rather, the concern is with developing boundary conditions for the numerical model such that Kelvin and Poincaré waves generated inside the model domain exit with as little reflection as possible back into the bay. Although it is true that our comparison with observations in Chapter 4 will be limited to the sub-inertial frequency range, we would prefer to develop a model suitable for the more general case.

The boundary conditions must also be such as not to generate spurious effects which contaminate the solution. In particular, it is important that the model does not make

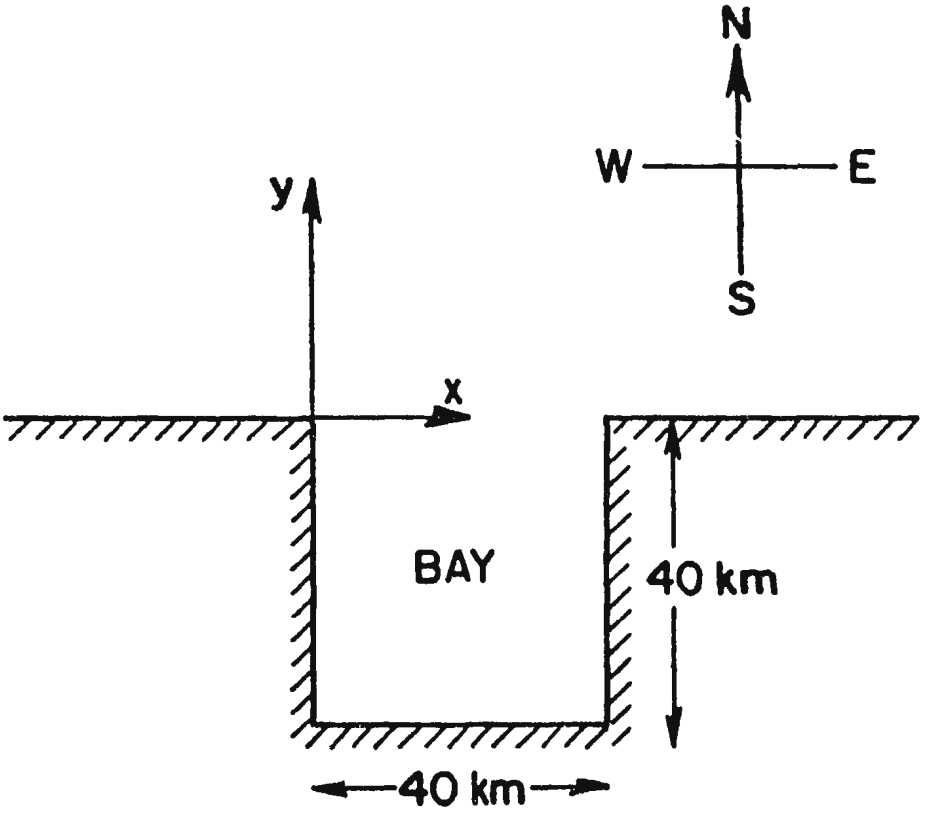

Figure 3.3 The model geometry used to determine suitable boundary conditions

spurious inferences about the nature of the region outside the model domain. Figure 3.3 shows a straight coastline to the west of the bay. However, the nature of the coastline in this region is of no concern to the problem we are trying to solve. Indeed, in the case of Conception Bay, there is another bay, Trinity Bay, to the west. The influence of Trinity Bay on Conception Bay is not a problem we will address. This situation is no different from that in any other limited area model. Indeed, with any such model, it is important that information is not inferred about the region beyond the model domain unless that information is explicitly given to the model.

In section 10.10 of his book, Gill (1982) shows that when alongshore length scales are large compared to the radius of deformation and time scales are long compared to $1/f$, equations (3.1), (3.2) and (3.3) can be used in the nearshore region to derive a wave equation of the form

$$\frac{\partial A}{\partial t} + c\frac{\partial A}{\partial s} = X, \tag{3.9}$$

where A is the amplitude of η at the coast, X is proportional to the alongshore wind stress at the coast, $c = (g'H_1)^{1/2}$ and (3.9) describes the propagation of a forced Kelvin wave around the coastal boundary, with s measuring distance around that boundary. Note that equation (3.9) is the same equation derived by Gill and Clarke (1974) for a Kelvin wave modified by alongshore wind stress (see equation (1.7) of this thesis). For this problem, neglecting the influence of regions "upstream" in the sense of Kelvin wave propagation (i.e. regions for which $s < s_o$) is clearly well-posed - one simply fixes $A = 0$ at $s = s_o$. However, once alongshore variations of the order of, or less than, the radius of deformation and time scales of the order of, or less than $1/f$ are considered, the problem is complicated by the

presence of Poincaré waves. These waves can propagate in all directions and in particular, "backwards" in the sense of Kelvin wave propagation. Clearly, fixing η at $s = s_0$ will lead to spurious reflection of these waves. The problem in this more general case is how to neglect the influence of "upstream" regions, while at the same time allowing Poincaré waves to exit through the "upstream" boundary.

3.6: Basic Form of the Radiation Condition to be Used

The formulation of open boundary conditions is a long-standing and important problem that has faced modellers of the atmosphere and ocean ever since the first numerical integrations (e.g. Charney et al., 1950). For a review the reader is referred to Røed and Cooper (1986). In this thesis, two kinds of open boundary conditions will be considered: radiation conditions and sponge layers. This section describes the radiation condition used. The use of the sponge layers is discussed in section 3.9. The basic building block is the Sommerfeld radiation condition (Sommerfeld, 1949)

$$\frac{\partial Q}{\partial t} + \frac{\tilde{c}\partial Q}{\partial n} = 0, \tag{3.10}$$

where Q is usually taken to be η, but also sometimes the unforced parts of u and v (see later), $\tilde{c}$ denotes propagation speed normal to the boundary, and $\partial/\partial n$ denotes spatial derivative normal to the boundary. Following Miller and Thorpe (1981), (3.10) is applied using forward-in-time, upstream differencing with $\tilde{c} \geq 0$, i.e.

$$Q_b^{n+1} = Q_b^n - \left(\frac{\tilde{c}\Delta t}{\Delta n}\right)(Q_b^n - Q_{b-1}^n), \tag{3.11}$$

where superscript n denotes time-level, b is the boundary grid point, $b-1$ is one grid point in from the boundary and Δn is the grid spacing normal to the boundary. In order to

determine $\tilde{c}$, (3.10) is applied to values of Q just inside the boundary and at preceding times, i.e.

$$\hat{c} = \frac{\tilde{c}\Delta t}{\Delta n} = -(Q^n_{b-1} - Q^{n-1}_{b-1})/(Q^{n-1}_{b-1} - Q^{n-1}_{b-2}), \tag{3.12}$$

where $(b-2)$ denotes two grid points in from the boundary. If $\hat{c} \leq 0$, indicating wave propagation into the model domain, then $\tilde{c}$ in (3.11) is set equal to zero. Otherwise, when $\hat{c} > 0$, $\tilde{c}$ is set equal to $\hat{c}\Delta n/\Delta t$, following Orlanski (1976), with the limitation that if $\hat{c} > 1$, then $\tilde{c} = \Delta n/\Delta t$. Other choices when $\hat{c} > 0$ are to put $\tilde{c} = \Delta n/\Delta t$, following Camerlengo and O'Brien (1980), or $\tilde{c} = \sqrt{g' H_1}$. All three alternatives worked well in the test cases run, although, overall the Orlanski method appears to work marginally better. For this reason results are presented using only Orlanski's method.

Since the bay is large compared to the Rossby radius, the velocity field at the mouth, and beyond a Rossby radius from the coast, will be dominated by oscillations of near-inertial frequency (Pollard, 1970; Greatbatch, 1983), a first order description for which is provided by

$$\begin{aligned} u_t - fv &= \frac{\tau^x}{\rho_o H_1} \\ v_t + fu &= \frac{\tau^y}{\rho_o H_1}. \end{aligned} \tag{3.13}$$

These equations are valid when the length scale is large compared to the baroclinic Rossby radius. This contrasts with the barotropic case considered when designing open boundary conditions for tidal (e.g. Garrett and Greenberg, 1977) or shelf models (Chapman, 1985). This is because the barotropic Rossby radius of deformation is usually comparable to or larger than the size of the bay, implying much weaker inertial oscillations in the barotropic case. It follows that, for the problem of Conception Bay, any formulation of boundary

conditions at the mouth must allow for inertial oscillations on the boundary. Since inertial oscillations described by (3.13) are a local, forced response of u and v to wind, it follows that applying the radiation condition to u and v directly is not appropriate. A grid arrangement was therefore adopted with η chosen to be on the open boundary, together with u on the northern boundary and v on the eastern and western boundaries as required by the use of the C-grid. To begin with, the radiation condition (3.11) was applied only when calculating the new value of η on the boundary with the velocity component on the boundary set equal to its value at the first grid point inside, e.g., on the northern boundary $u_b^{n+1} = u_{b-1}^{n+1}$ and on the eastern and western boundaries $v_b^{n+1} = v_{b-1}^{n+1}$. Later, we experimented with applying a radiation condition to the propagating part of u and v by splitting the velocity field near the boundary into two parts, following Gill (1982, Ch. 9); that is, an Ekman part (u_E, v_E) defined by

$$\begin{aligned} u_{Et} - f v_E &= \frac{\tau^x}{\rho_o H_1}, \\ v_{Et} + f u_E &= \frac{\tau^y}{\rho_o H_1}, \end{aligned} \tag{3.14}$$

and a pressure-driven part defined by

$$\begin{aligned} u_{pt} - f v_p &= -g' \eta_x, \\ v_{pt} + f u_p &= -g' \eta_y, \\ \eta_t + H_1 (u_{px} + v_{py}) &= -H_1 (u_{Ex} + v_{Ey}). \end{aligned} \tag{3.15}$$

The radiation condition was then applied to u_p or v_p, as appropriate, in addition to η with the total velocity on the boundary being obtained by adding the Ekman part. This form of radiation condition gives more noisy results than are obtained using the original method of

setting velocities on the open boundaries equal to the velocities just inside. Therefore, the original, simpler method was chosen for all results to be presented. It should be noted that in all the calculations to be described in this chapter a spatially uniform wind stress field is used. This means that the Ekman divergence term in (3.15) is zero. If this were not zero, the local Ekman pumping it represents could easily be incorporated into the calculation of η on the boundary.

The above method of splitting the velocity field into two parts is a modification of the method originally proposed by Reed and Smedstad (1984) for splitting the solution near the boundary into "forced" and "free" parts. These authors considered open boundary conditions applied across a channel. It therefore made sense for them to retain cross-channel gradients of η when defining the forced part of their solution. In the case of Conception Bay, however, the ocean beyond the bay is unbounded both away from the coast and along it. It therefore makes sense to split the velocities into "free" and "forced" parts without singling out any coordinate direction when defining the "forced" part.

3.7: Problems with Using a Radiation Condition on an "Upstream" Boundary

Consider the set-up shown in Figure 3.4 in which the Orlanski type radiation condition described in section 3.6 is applied on all open boundaries; that is, a radiation condition is applied to η, and the velocity component on the open boundary is set equal to its value at the first grid point in from the boundary. It should be noted that the "upstream" boundary, in the sense of Kelvin wave propagation, is the western boundary of the model domain (northern hemisphere assumed). It is from this boundary that Kelvin waves can propagate along the coast into the interior of the domain. Figure 3.5 shows time series of η

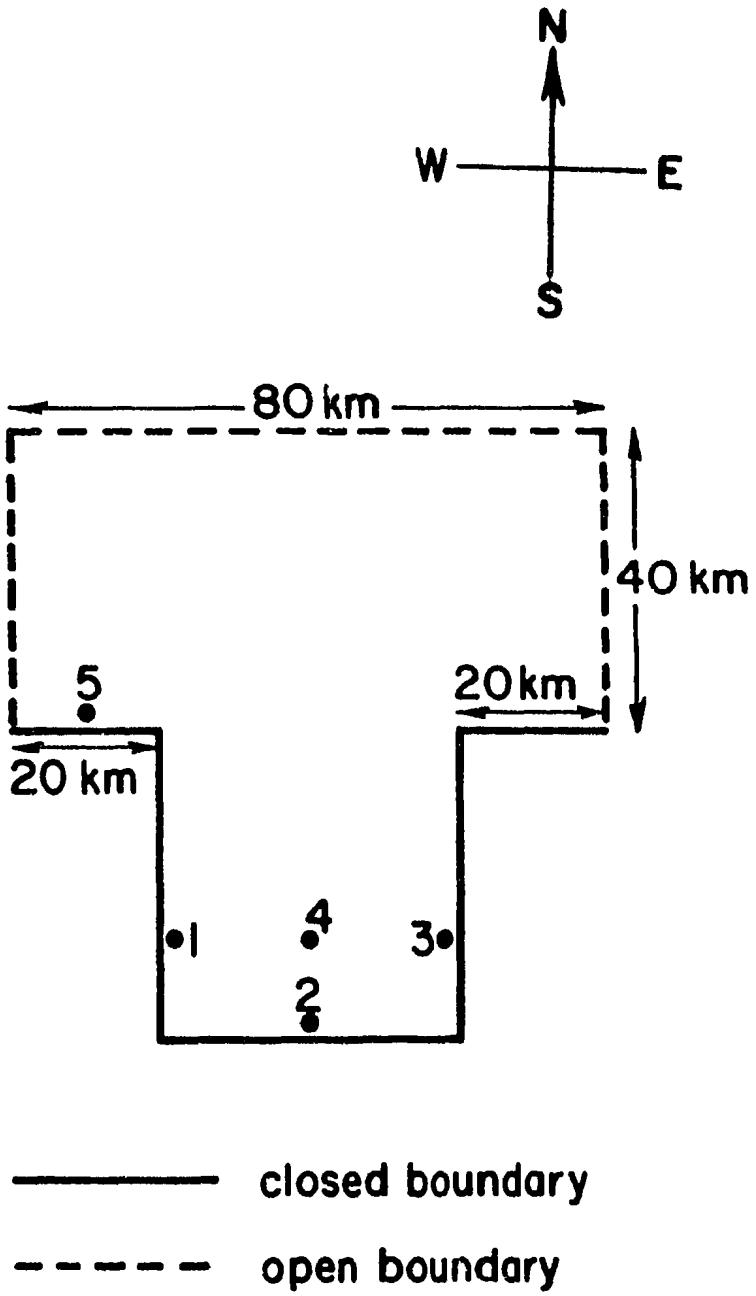

Figure 3.4 The model domain with a radiation condition applied on the western, northern, and eastern boundaries

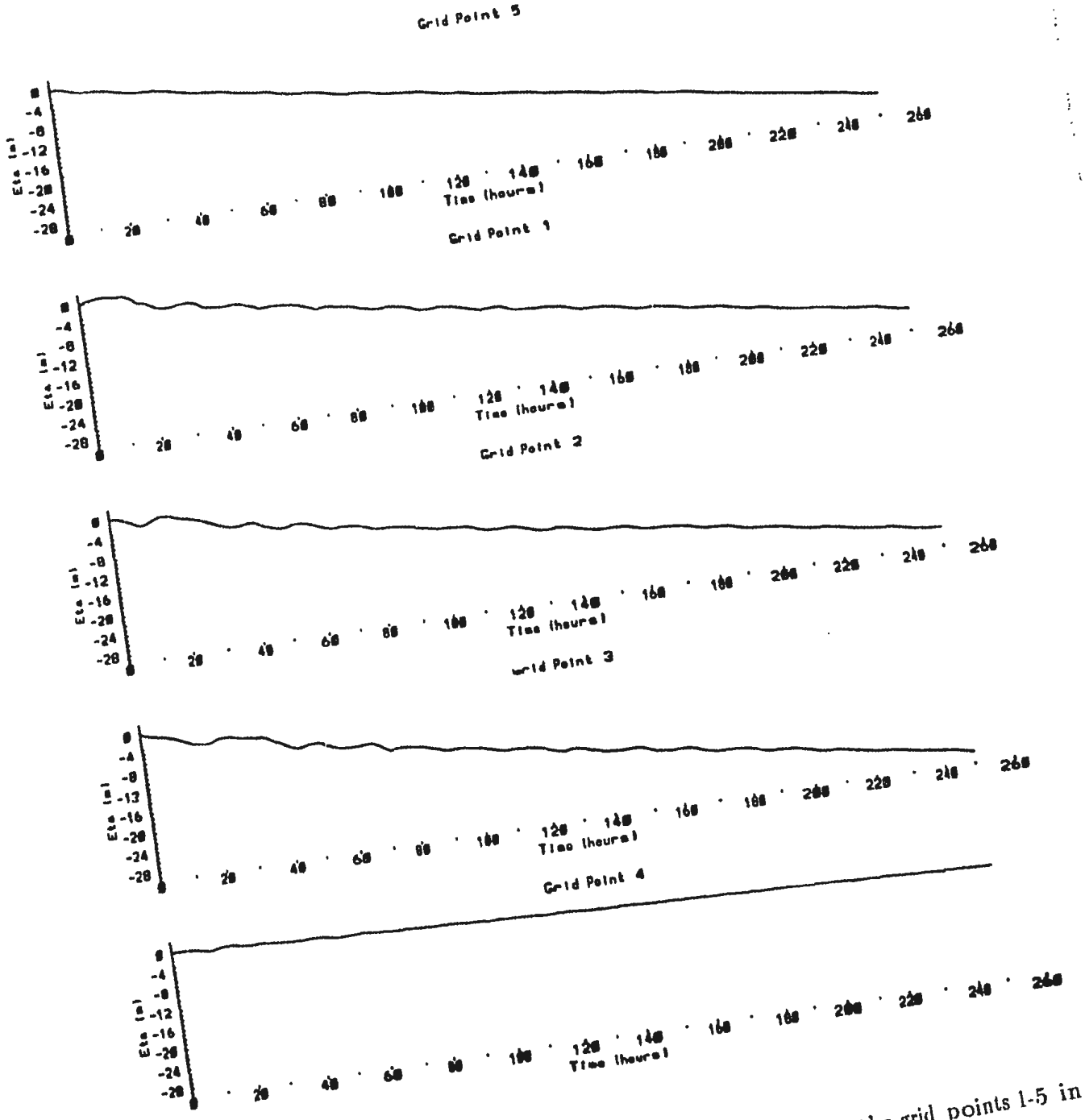

Figure 3.5 Time series of the interface displacement (in meters) at the grid points 1-5 in Figure 3.4 following the sudden application at $t = 0$ of a uniform, steady, westward wind. Note that negative values of η represent upwelling of the interface.

at each of the grid points numbered in Figure 3.4 following the sudden turn-on at $t = 0$ of a uniform, steady, westward wind. The initial conditions are $u = v = \eta = 0$ everywhere. It is clear that a steady upwelling of the interface soon becomes established at each grid point, as indicated by the increasingly negative values of η, including at grid point 5, located 10 km in from the "upstream" boundary. (Recall that the governing equations are interpreted as being for the upper layer of a two-layer ocean in which the lower layer is infinitely deep and at rest. η is the downward displacement of the interface between the two layers.) It is interesting to see how the initial increase in η at grid point 1, in response to the sudden turn-on of the onshore wind, appears a little later at grid point 2 and then a little later again at grid point 3, as it is propagated around the bay as a coastal Kelvin wave. This is followed by the onset of the negative trend in η. Note that the rate of decrease of η is less at grid point 4, in the interior of the bay. This is because the upwelling is confined to within a Rossby radius of deformation of the coast. At first sight, it appears that the upwelling is being driven by the Ekman transport away from the stretch of coastline immediately to the west of the bay, in the area of grid point 5, and being propagated to the rest of the coastline by means of Kelvin waves. However, the rate of upwelling is less than half that predicted by theory. The solution for steady Ekman transport away from an infinite coastline is given on p. 404 of Gill(1982) and, for η (Gill's equation (10.11.2)), is

$$\eta = -\left(\frac{\tau^x}{\rho_o c} e^{-fy/c}\right) t, \tag{3.16}$$

where the coordinate y is as in Figure 3.3. Substituting values appropriate to this experiment (i.e. $\tau^x = 0.05$ Nm^{-2}, $\rho_o = 1027$ kgm^{-3} and $c = 0.7$ ms^{-1}) gives a value for

η_t appropriate to the location of grid point 5 (that is 0.5 km out from the coast) of 6.5 $\times 10^{-5}$ ms^{-1}, whereas the time series in Figure 3.5 (in particular at grid point 5 but also at the other grid points) indicate a value of roughly 2.6×10^{-5} ms^{-1}. Using radiation of the propagating part of velocity as well as η also underestimates the analytic value of η_t. (Replacing the radiation condition on the "upstream" boundary by the condition $\eta_x = 0$ does give a value for the rate of decrease of η in agreement with (3.16). The use of the condition $\eta_x = 0$ is discussed at the beginning of the next section.) This demonstrates a "lack of control" on the solution introduced by the radiation condition. On the one hand, following Chapman (1985, section 4b), one might expect the model to assume that the coastline to the west continues to infinity. However, it does not do so, since otherwise the rate of upwelling would be given by (3.16). On the other hand, the model is certainly making some assumption about the nature of the region to the west, beyond the model domain. Indeed, as the discussion of equation (3.9) in section 3.5 indicates, since the model is given no explicit information about the region outside the domain, η at grid point 5 should remain near to zero (the only departures from 0 being due to outgoing Poincaré waves not included in equation (3.9)). An alternative way to look at this is to follow Jensen (1990) and note that the Kelvin wave part of the model variables is determined on an "upstream" boundary by Kelvin waves propagating along the coast from outside the model domain. The Kelvin wave part includes that associated with time scales greater than $1/f$ and, in particular, the long term trend apparent in Figure 3.5. Since information on the region beyond the model domain is missing from the model, it follows that the long term trend in Figure 3.5 is spurious.

Next, consider the response of the model to the sudden turn on at $t = 0$ of a uniform, steady, northward wind. As before, the initial conditions are $u = v = \eta = 0$. The solid line in Figure 3.6 shows time series of η at the grid points numbered in Figure 3.4. This time, there is no long period trend in η; however, oscillations of near inertial frequency are present (the period is 15.5 hours compared with the inertial period of 17.5 hours). These show strong phase propagation around the coastline and are barely evident at grid point 4 in the interior of the bay. In fact, these are Kelvin waves which are generated at the "upstream" boundary. That they are dependent on the boundary is demonstrated by the dashed line in Figure 3.6. The dashed line shows time series of η for a case in which the western boundary in Figure 3.4 is moved 20 km farther to the west. The grid points are the same as before, except grid point 5 which is also moved 20 km to the west so that it remains 10 km. from the boundary. At grid points 1-4, the resulting oscillations are almost 180° out of phase, indicating a strong dependence on the location of the "upstream" boundary. On the other hand, the time series at the grid point 5, located 10 km in from the "upstream" boundary in each case, are both in phase, confirming that the oscillation is, in fact, originating from the boundary. (Actually on the boundary itself, η remains very close to zero. The problem is that η should oscillate there with near-inertial frequency. The fact that it does not leads to the generation of the near-inertial Kelvin waves.)

Two problems with using this particular radiation condition on an "upstream" boundary have been identified. In the first case, when there is Ekman transport perpendicular to the stretch of coastline immediately to the west of the bay, a long-period trend sets in which soon completely dominates the model solution. This trend is entirely spurious and

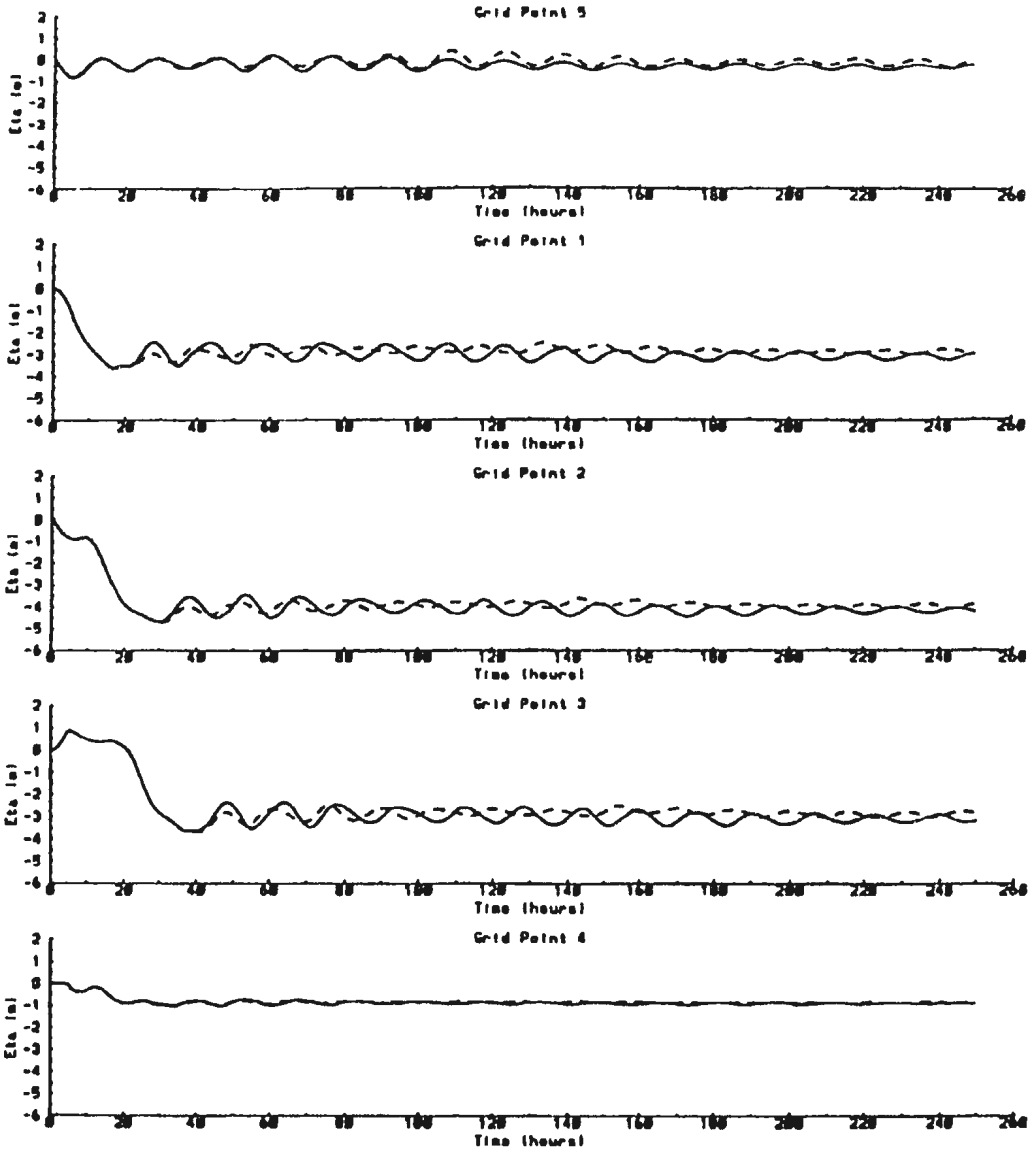

Figure 3.6 Time series of the interface displacement (in meters) following the sudden application at $t = 0$ of a uniform, steady, northward wind. The solid lines represent the interface displacement at the grid points 1-5 in Figure 3.4. The dashed lines represent the interface displacement in the case where the western boundary is moved 20 km to the west. For the dashed-line case, grid points 1-4 remain in the same position, and grid point 5 is moved so that it is still 10 km from the western boundary.

does not even correspond to the case in which the coastline to the west extends to infinity. In the second case, Kelvin waves of near-inertial period are generated at the boundary and propagate into the solution domain, contaminating the solution.

3.8: A Suitable "Upstream" Boundary

We begin by asking what form of condition on the "upstream" boundary would be appropriate in the case that the coastline and forcing does, indeed, extend westwards to infinity. If this boundary is placed far enough to the west of the bay, then we expect the gradient of η parallel to the coast to be near to zero, as for an infinite straight coastline with no bay. To solve the problem of the coastline and forcing extending westwards to infinity, we use the model domain shown in Figure 3.7, in which the western boundary is placed 150 km to the west of the bay, and the condition $\eta_x=0$ is applied there. In a case with a uniform, steady, westward wind, upwelling is driven by Ekman divergence away from the stretch of coast to the west of the bay, and η_t soon assumes, throughout the bay, the value given by (3.16). On the other hand, with a uniform, steady, northward wind, Kelvin waves of near-inertial period are found to propagate around the bay (time series for this case are shown by the dashed line in Figures 3.10a,b to be discussed in detail later). However, these are not found along the coastline to the west of the bay and are not dependent on the location of the western boundary. Indeed, they appear to be a genuine part of the solution generated at the northwest corner of the bay.

The problem is, however, that the coastline to the west of Conception Bay is not straight. The model domain shown in Figure 3.7, and, indeed, any domain that includes coastline west of the mouth, is not appropriate for solving the local wind-forced response.

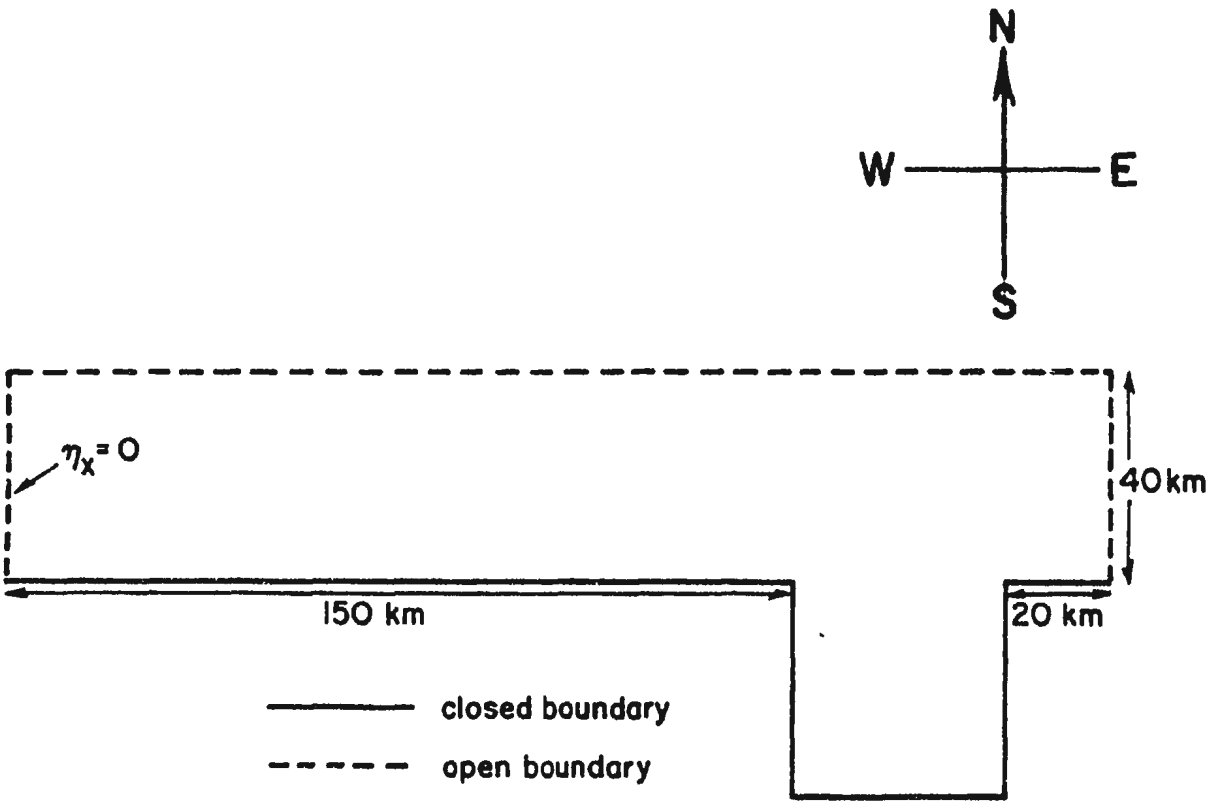

Figure 3.7 The model domain with a radiation condition applied on the northern and eastern boundaries and the condition $\eta_r = 0$ applied on the western boundary, with the latter moved to the west of the bay.

Influences "upstream" of the mouth (in the sense of Kelvin wave propagation) should be avoided in the model solution. Therefore, the model set-up shown in Figure 3.8 is suggested, in which the coastline on the "upstream" side of the mouth of the bay is extended beyond the mouth and a condition $\eta_x = 0$ is applied on the artificial part of the boundary. Radiation conditions are applied on the other open boundaries, as before. The important thing about this set-up is that the western open boundary of the model domain is simply an extension of the coast. In particular, it runs parallel to the coast rather than perpendicular to it (as it does in Figure 3.4). This means that the model does not see the western boundary as cutting across the coastal waveguide - rather, the waveguide suddenly starts on the boundary at the point where it becomes coincident with the coast. In this way, the model is prevented from assuming information about the region to the west of the bay.

The choice of $\eta_x = 0$ on this boundary is less clear cut. The most important point is that this condition prevents Kelvin waves from propagating on the artificial part of the boundary north of the mouth of the bay. In this way, the coastal waveguide is separated from the radiation condition applied on the northern boundary, and artificial effects of the kind discussed in the last section are avoided. On the other hand, the boundary must also be able to deal with incident Poincaré waves without leading to unacceptable reflections. In this respect, putting $\eta_x = 0$ is attractive since Poincaré waves generated in the bay are likely to impinge obliquely on the boundary and as such will have stronger gradients in the north-south than the east-west direction. It follows that putting $\eta_x = 0$ should be a reasonable approximation for such waves. Another possibility is to use the radiation condition described in section 3.6 on the western boundary. However, this results in the

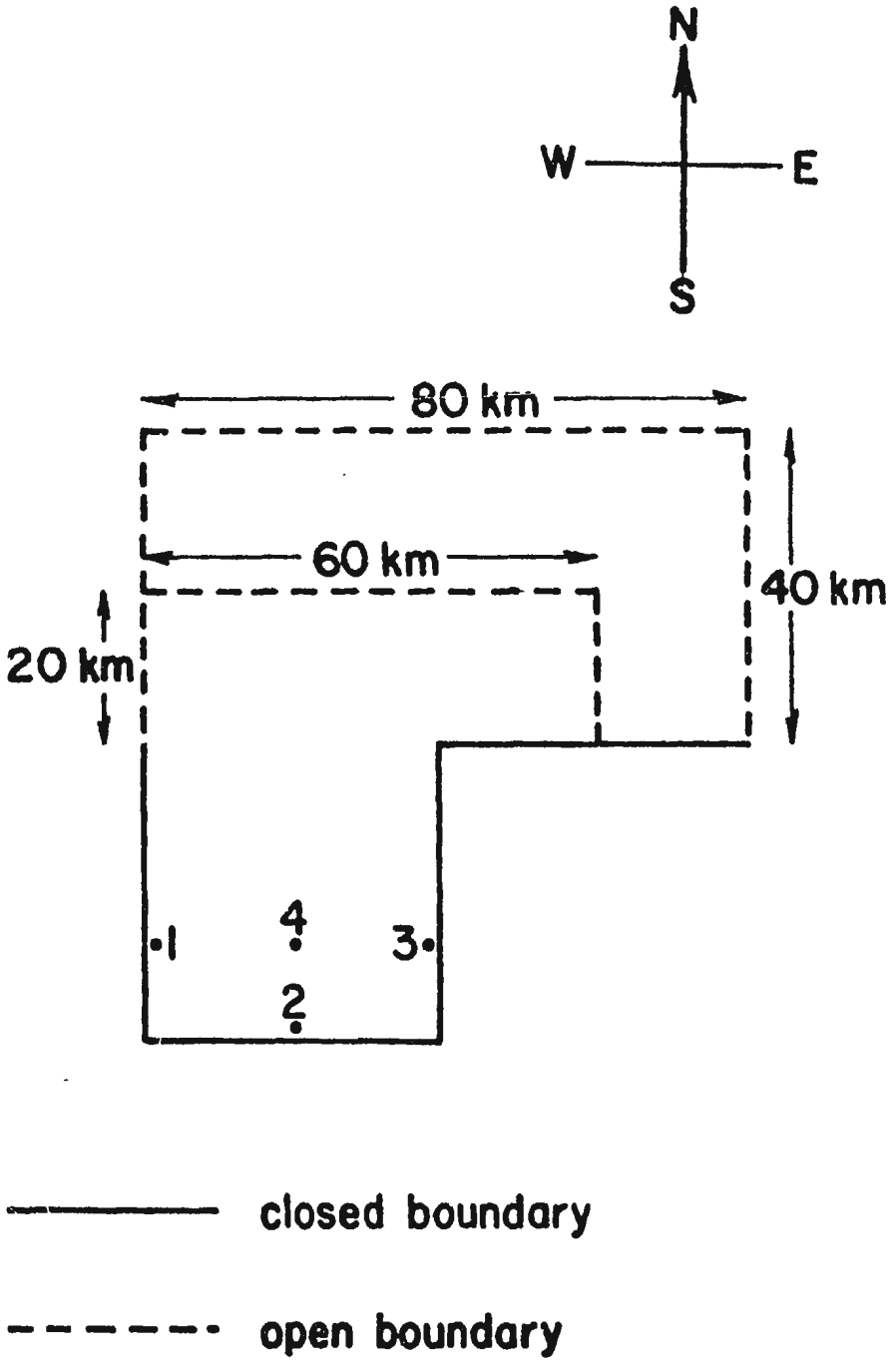

Figure 3.8 The two model domains incorporating the suggested open boundary formulation. A radiation condition is applied on the northern and eastern boundaries, and the condition $\eta_x = 0$ is applied on the open part of the western boundary.

possibility of artificially generating Kelvin waves of near-inertial period, as was found in the last section, and, as such, is best avoided.

Two model domains are shown in Figure 3.8. In the smaller one, the northern and eastern boundaries are placed 20 km beyond the mouth of the bay, while in the larger one, they are placed a further 20 km out. Solutions will be compared using these two domains and also the domain shown in Figure 3.7. The numerical implementation of the condition $\eta_x = 0$ is illustrated in Figure 3.9 for the model domains shown in Figure 3.8 (the implementation in the case of Figure 3.7 is very similar). The figure shows the grid arrangement along the western boundary near the mouth of the bay. South of, and including $j = 10$, we put $u = 0$ at the $i = \frac{1}{2}$ grid points. North of $j = 10$, put $\eta_{0,j} = \eta_{1,j}$ and $v_{0,j-\frac{1}{2}} = v_{1,j-\frac{1}{2}}$ and calculate u in the same way as in the main program. In this way, η_x is set to zero along the boundary, and the problem of setting v values at the $i = 0$ grid points is taken care of.

The solid lines in Figures 3.10a,b show time series of η at the grid points numbered in Figure 3.8. These are for identical model runs, apart from the fact that Figure 3.10a uses the smaller domain shown in Figure 3.8 and Figure 3.10b the larger domain. The dashed line in each figure is the corresponding time series obtained using the model domain shown in Figure 3.7 and, as discussed earlier, corresponds to the solution when the coastline and forcing to the west of the bay extend out uniformly to infinity. In each case, $u = v = \eta = 0$ initially, and the model is spun up by the sudden application at $t = 0$ of a uniform, northward wind stress. The wind stress is kept constant throughout the integrations. For the first 15 hours or so, the three time series are identical. After this time, the dashed line falls below the solid curves in each of the figures. This is because in the dashed line case, the interface

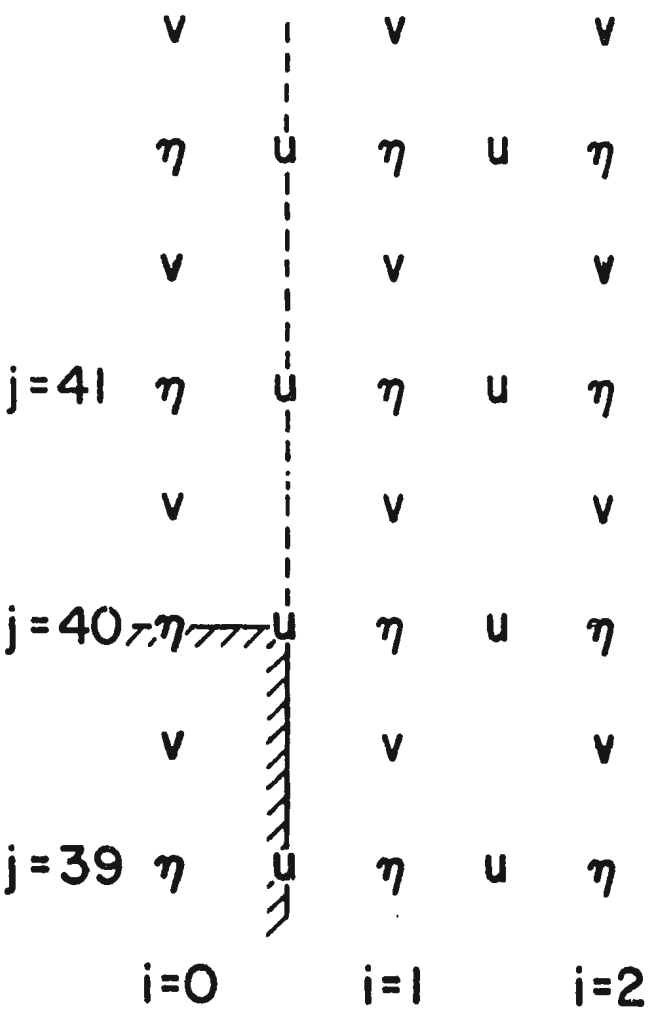

Figure 3.9 Grid arrangement used on the western boundary for the model domains shown in Figure 3.8.

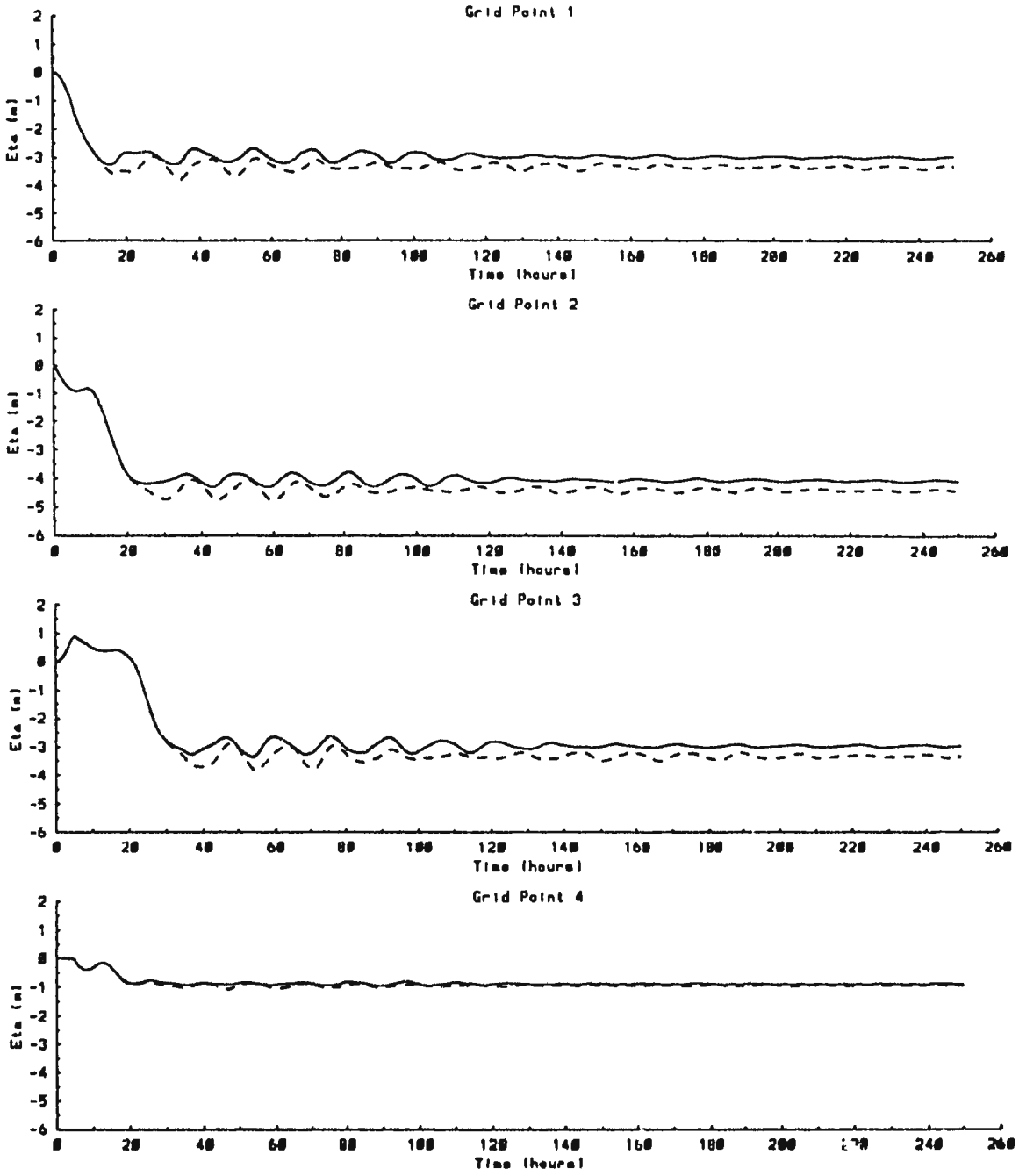

Figure 3.10a Time series of the interface displacement (in meters) at the grid points numbered in Figure 3.8 following the sudden application at $t = 0$ of a uniform, steady, northward wind. The solid lines represent the case using the smaller domain in Figure 3.8. The dashed lines are obtained using the domain shown in Figure 3.7.

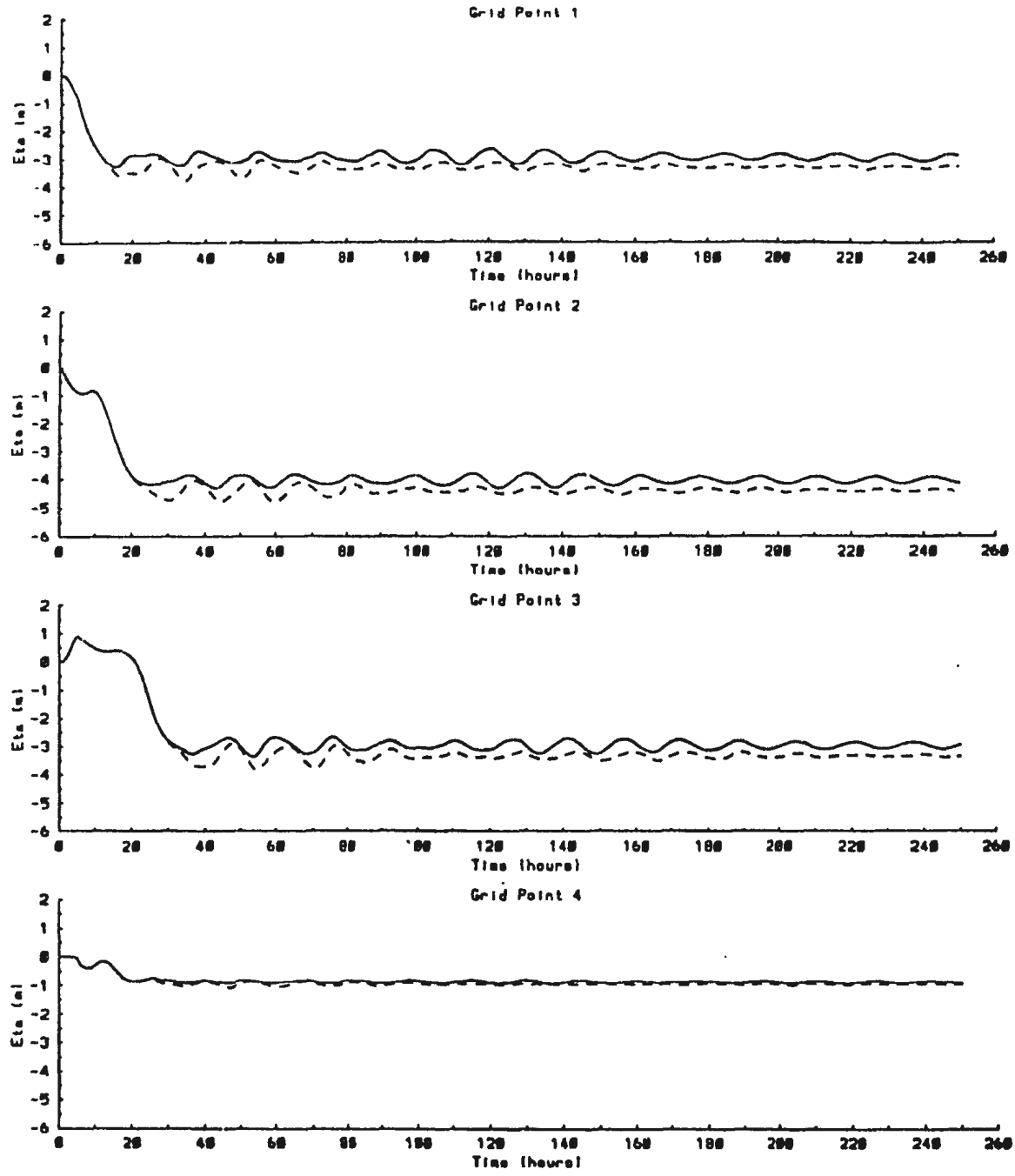

Figure 3.10b Time series of the interface displacement (in meters) at the grid points numbered in Figure 3.8 following the sudden application at $t = 0$ of a uniform, steady, northward wind. The solid lines represent the case using the larger domain in Figure 3.8. The dashed lines are obtained using the domain shown in Figure 3.7.

all along the coast to the west of the bay is upwelled slightly during the first couple of hours following the sudden imposition of the offshore wind. This net upward movement, which extends westwards to infinity, is transmitted eastwards into the bay by means of Kelvin waves and accounts for the negative offset of the dashed line in each of the figures. The fact that this is not found in the other cases is encouraging, since the boundary formulation used in these cases (i.e. Figure 3.8) is supposed to exclude the influence of regions beyond the model domain. At later times, all three cases show the presence of Kelvin waves of near-inertial frequency. Although these oscillations are not identical, those shown for the two cases in Figure 3.10b do roughly agree in phase and amplitude. By comparison, in the smaller domain case, shown by the solid line in Figure 3.10a, the oscillations tend to become out of phase and also die out rather quickly. Other cases using the model domain shown in Figure 3.8 have been tried but with the northern and eastern boundaries placed even further out from the bay than 40 km. The corresponding time series in each of these cases are similar to the solid line in Figure 3.10b. This shows that it is important to place the northern and eastern boundaries far enough out from the bay (for this problem at least 40 km). The fact that there is a reasonable level of agreement between the two time series in Figure 3.10b, and also to some extent Figure 3.10a, is most encouraging. It has been noted that, for the dashed line case, the near-inertial Kelvin waves are generated by the northwest corner of the bay. Given the placement of the western boundary in the solid line cases (Figure 3.8) it is not surprising that these waves should be corrupted compared to that case. On the whole, however, the level of corruption evident from Figure 3.10b is small.

Figures 3.11a,b show the same time series but for a case in which a uniform, westward wind is suddenly turned on at $t = 0$ and then held constant. In the dashed line case, the upwelling, indicated by the increasingly negative values of η, is driven by the Ekman transport away from the coastline to the west of the bay. The rate of decrease of η in this case agrees with that given by equation (3.16) (account must be taken for the fact that the grid points are actually 0.5 km away from the coast). The absence of information about the region to the west of the bay in the solid line cases eliminates this trend. Indeed, in these cases, there is no trend, either positive or negative, following the initial adjustment. Kelvin waves of near-inertial frequency are again found in these cases (they probably also occur in the dashed line case, but are masked by the negative trend in η). As before, they die out quicker in the smaller domain case and also tend to become out of phase with those in the larger domain case. Figures 3.12a,b show plan views of η in the smaller domain case 117 hrs into the integration in both the northward (Figure 3.12a) and westward (Figure 3.12b) wind cases. At this time the model is essentially in a steady state with the pressure gradient along the coast balancing the wind stress. Note that in each case, η is zero at the northwest corner of the bay, as is expected from the discussion following equation (3.9) in section 3.5.

Finally, the model domain shown in Figure 3.7 and the larger domain shown in Figure 3.8 are used to explicitly examine the reflectivity of the western boundary formulation to Poincaré waves generated in the bay. The model is run using both these domains with zero wind forcing. In each case, it is initialized with $u = v = 0$ everywhere and a jump in η from +5 m in the north to -5 m in the south. The jump is defined by a tanh function with

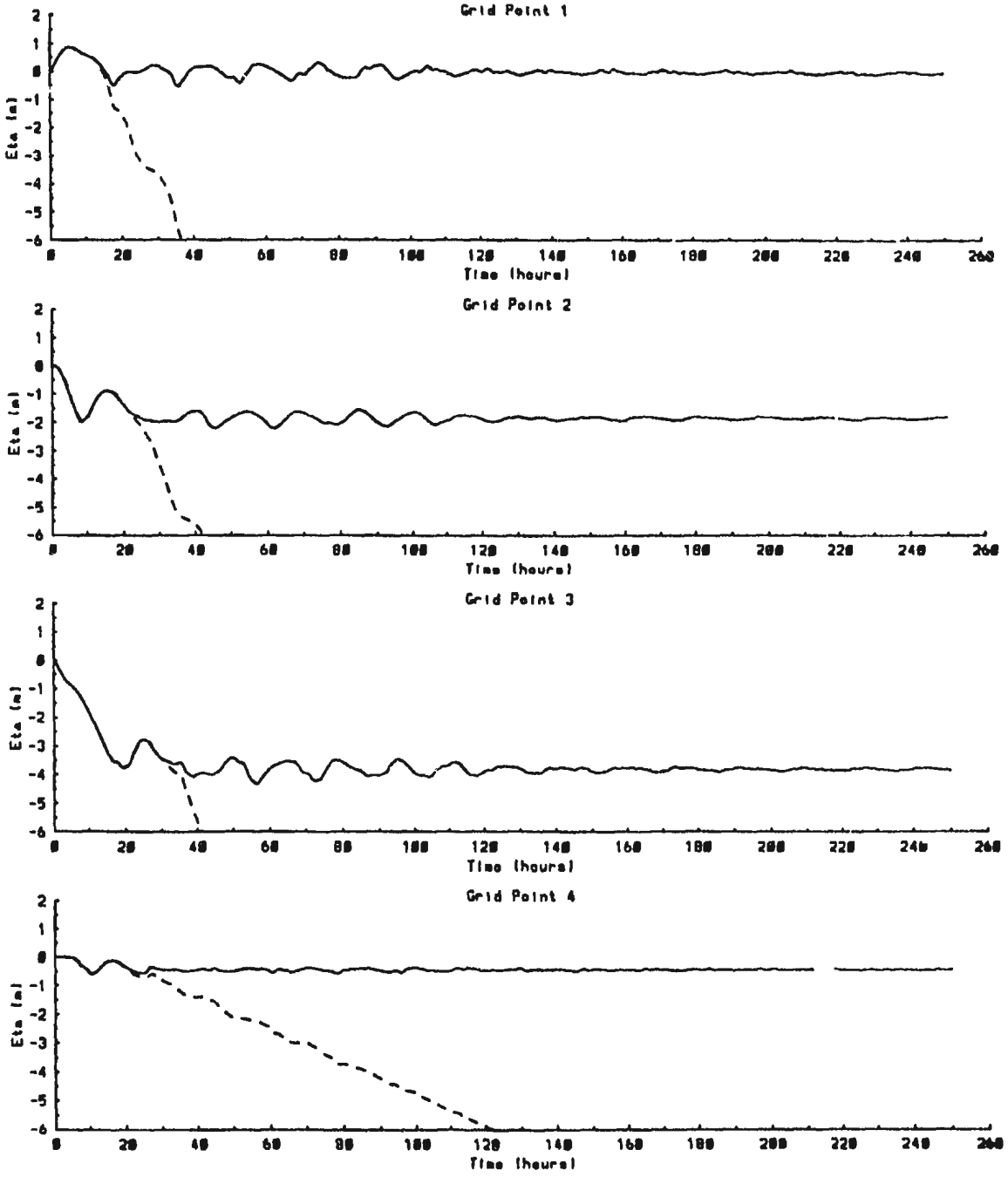

Figure 3.11a Same as Figure 3.10a, except that the model is driven by a westward wind, instead of a northward wind.

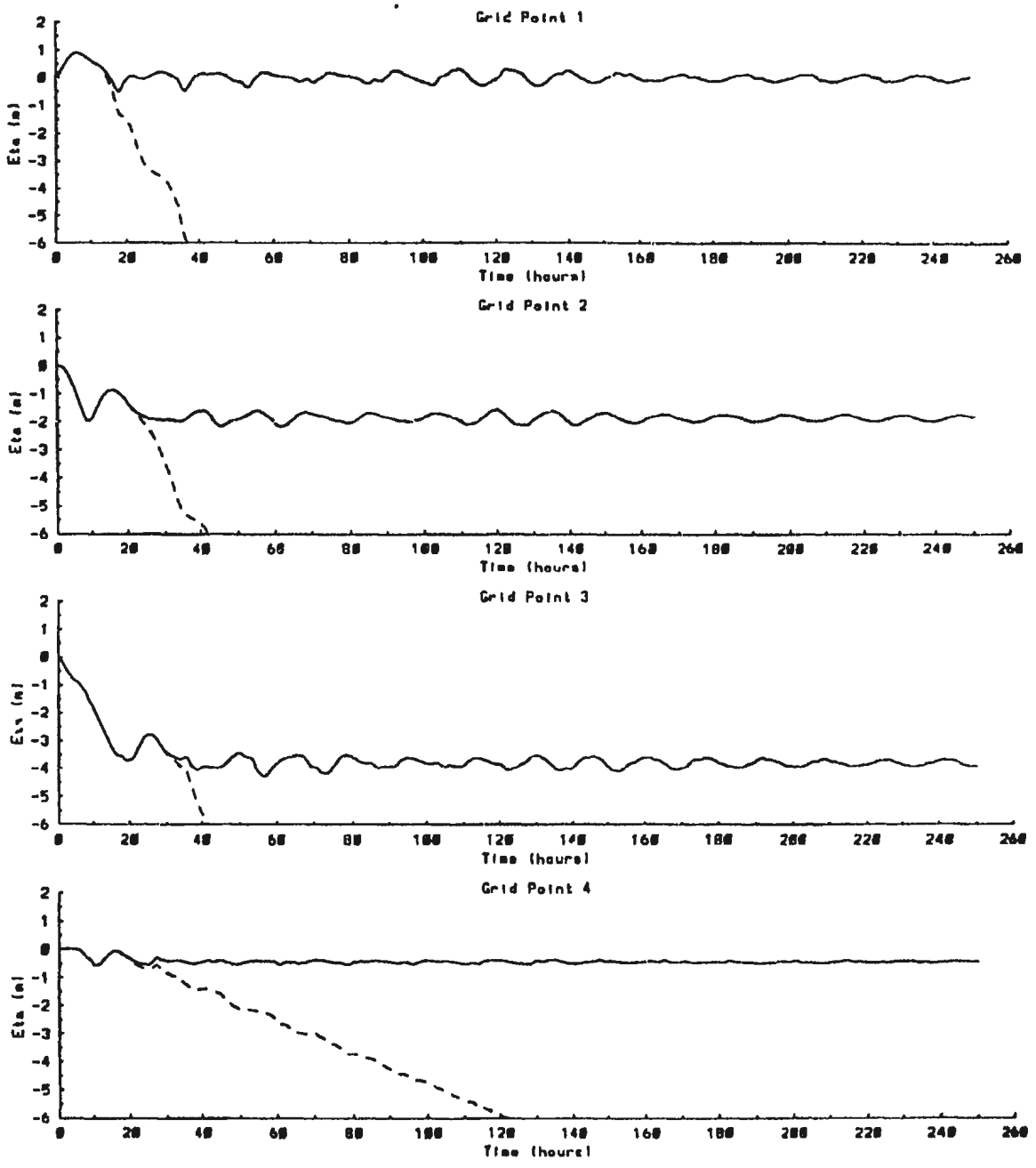

Figure 3.11b Same as Figure 3.10b, except that the model is driven by a westward wind, instead of a northward wind.

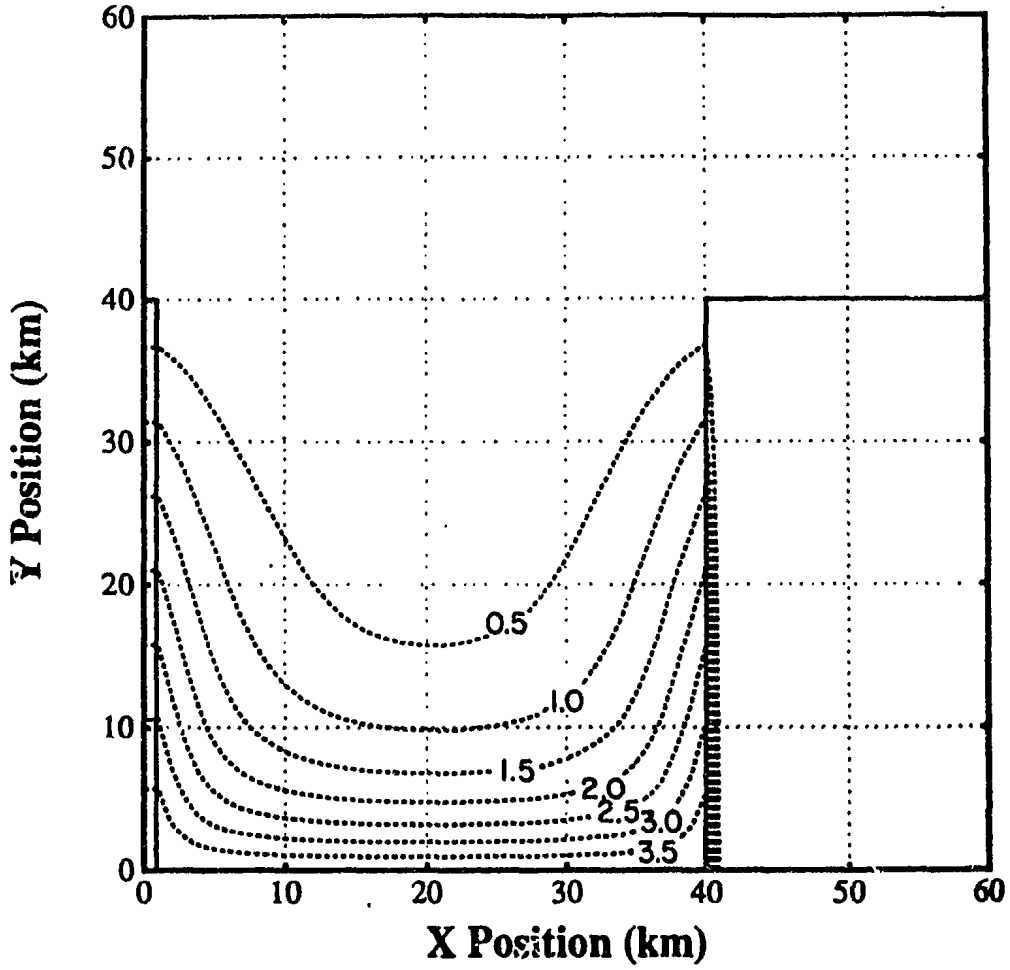

Figure 3.12a Plan view of the interface displacement in the smaller domain case shown in Figure 3.8 417 hours into the integration. The model is driven by a uniform, steady, northward wind. The contour interval is 0.5 m. The dashed lines indicate negative contours.

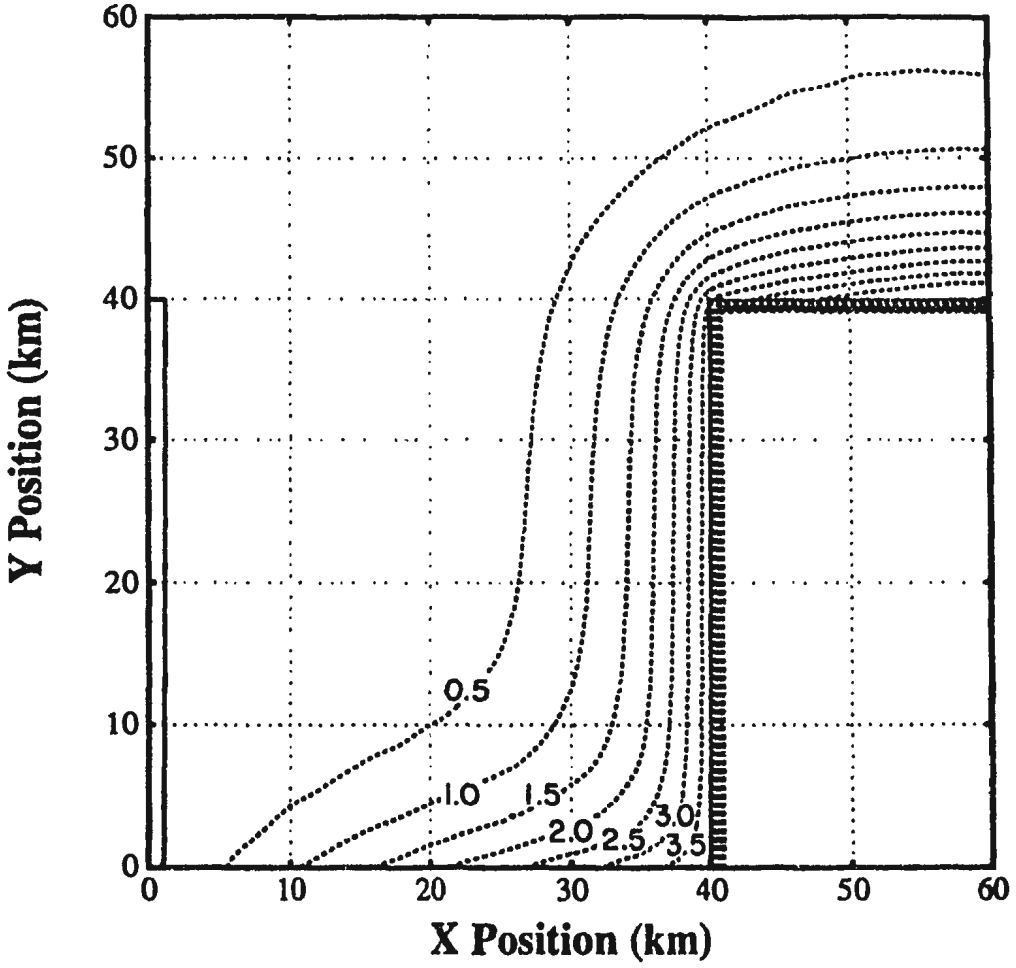

Figure 3.12b Same as Figure 3.12a, except for a uniform, steady, westward wind.

e-folding scale of 2 km. Figure 3.13 shows time series of η at the grid points corresponding to 1 and 3 in Figure 3.8, the dashed line being for the model domain in Figure 3.7 and the solid line for the larger domain in Figure 3.8. For the first 50 hours, the solution at each grid point in the dashed line case is independent of the open boundary formulation. This is because 50 hours is the time it takes for Poincaré waves excited by the initial discontinuity to arrive back at the grid points, having been reflected off the nearest boundary (in this case, the northern boundary). However, during that time, Poincaré waves will interact with the western boundary in the solid line case. Since the two time series are not exactly coincident during this time, it follows that reflection of Poincaré waves off the western boundary is occurring in the solid line case. However, both time series are very similar and, in particular, contain the same events. Given the success that has already been demonstrated by placing $\eta_x = 0$ on the western boundary in the wind-driven case, these dicrepancies are felt to be acceptable.

3.9: The Use of Sponge Layers

In this section, sponge layers on the northern and eastern boundaries are used rather than the radiation condition described in section 3.6. As before, the western boundary must be treated differently from the other open boundaries. This is because if a sponge is applied on the western boundary, information can propagate out of the sponge layer by means of Kelvin waves and contaminate the solution in the interior of the model domain. Therefore, the western boundary is treated exactly as in the last section and the condition $\eta_x = 0$ is implemented there. The model domain is the larger of the two shown in Figure 3.8. Two examples of sponges are considered. In the first, a damping term $-\gamma\eta$ is added

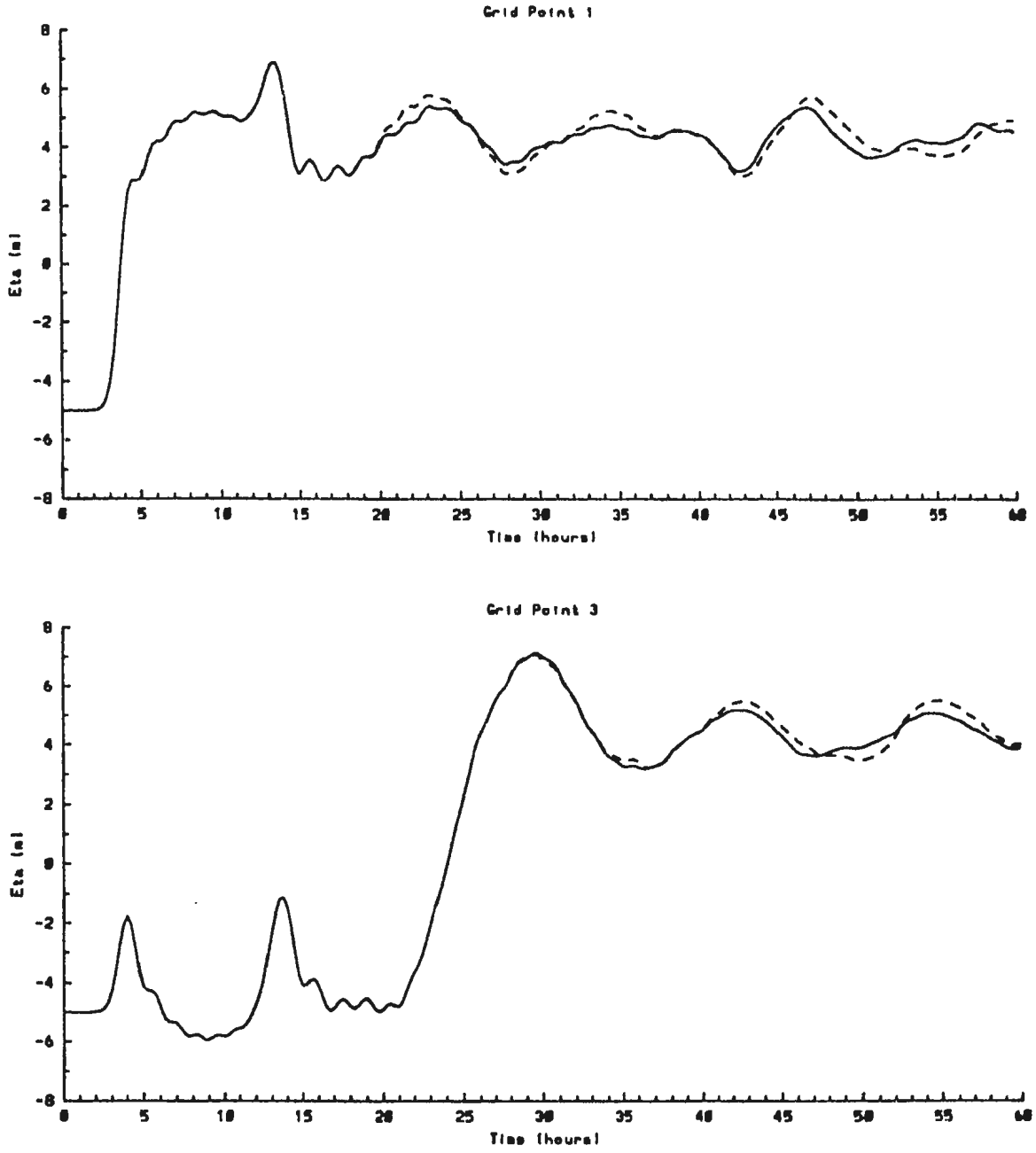

Figure 3.13 Time series of the interface displacement (in meters) at grid points 1 and 3 in Figure 3.8 for the two cases driven by an initial discontinuity in η. The dashed lines are obtained using the model domain shown in Figure 3.7, the solid lines using the larger domain in Figure 3.8.

to equation (3.3) and in the second, terms $-\gamma u$ and $-\gamma v$ are also added to each of equations (3.1) and (3.2), respectively. In all cases, γ decreases exponentially away from the northern and eastern boundaries and is given by

$$\gamma = \gamma_o \left(e^{\frac{(y-y_{max})}{a}} + e^{\frac{(x-x_{max})}{a}} \right), \tag{3.17}$$

where $\gamma_o = 1\ s^{-1}$, y_{max} and x_{max} are the values of y and x at the northern and eastern boundaries, respectively, and a is the e-folding scale, taken to be 1 km. Other e-folding scales were considered, but 1 km proved to give the best results, by minimizing the thickness of the sponge required. The value of γ is so large on the northern and eastern boundaries that η is clamped to the value zero there and in the second case, the velocities are also fixed at zero. In the case with η damping only the velocities are treated essentially as before and, in particular, are free to execute inertial oscillations on the boundary.

The solid line in Figure 3.14 shows time series of η, corresponding to those in Figure 3.10b, when the sponge is applied only to η. In this experiment, a uniform northward wind is suddenly turned on at $t = 0$ and then kept constant. Comparison of the two figures shows that these time series are very similar. The only difference seems to be that the near-inertial Kelvin waves now tend to have slightly larger amplitude. However, when the sponge is also applied to the velocities, the phase of these oscillations is completely changed (see dashed line in Figure 3.14). This is also found in a run in which damping is applied only to the pressure-driven part of the velocities, defined by equation (3.15), in addition to η. It seems, therefore, that sponging velocities may actually be counter-productive and that it is actually better to sponge the density field, i.e., η, alone. Another approach that

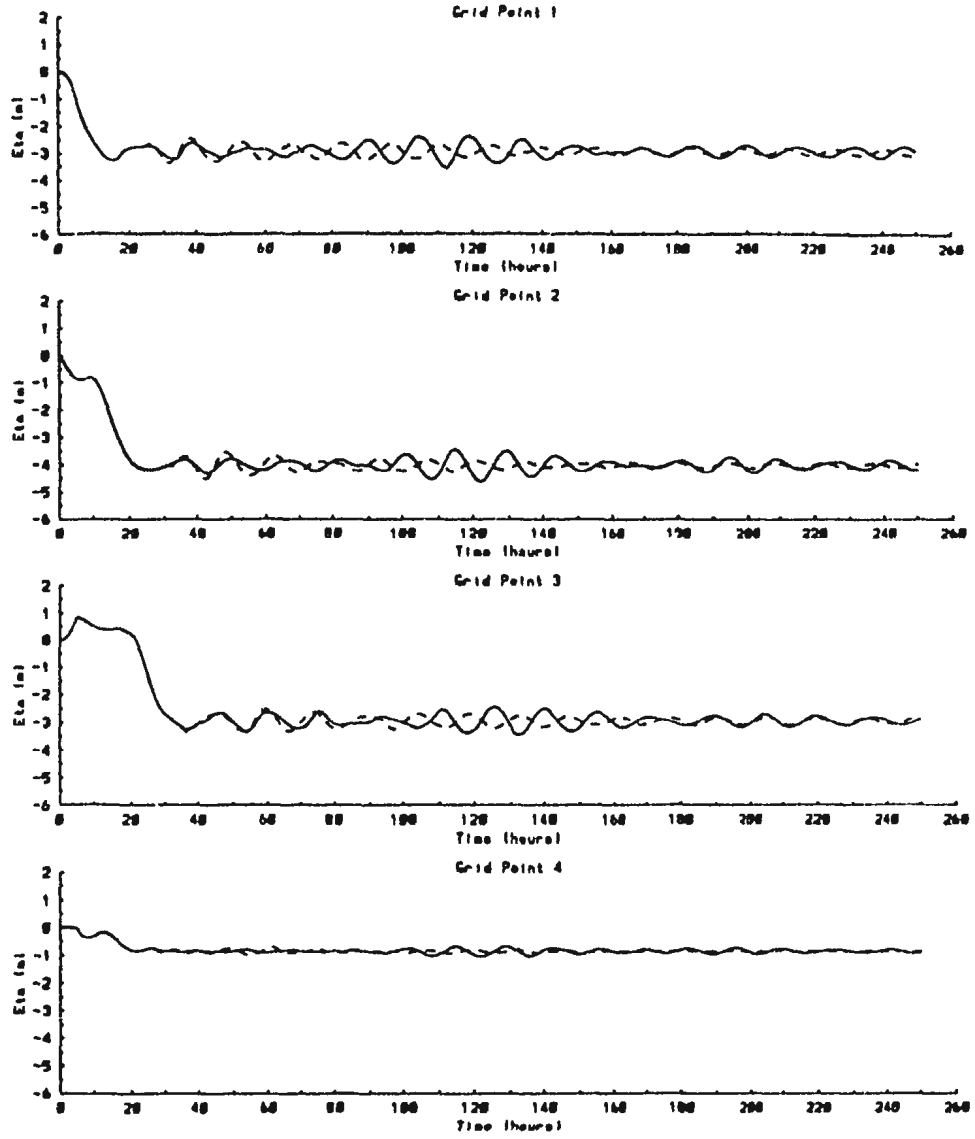

Figure 3.14 Time series of the interface displacement (in meters) when a sponge is applied near the northern and eastern boundaries of the larger domain shown in Figure 3.8. The solid lines represent the case when only interface displacement is damped. The dashed lines represent the case when both velocity and interface displacement are damped. The model is driven by a uniform, steady, northward wind.

has not been tried would be to have a very large sponge region extending many "bay-sizes" beyond the bay mouth so as to ensure that outgoing waves were only gradually attenuated. This, however, would involve using a very large computational domain and considerably greater computational resources than the use of radiation conditions or damping of η alone.

3.10: Applying the Boundary Conditions to Conception Bay

As discussed in previous sections, our aim is to model the response of Conception Bay to wind forcing over the bay. To do this, the methods used to exclude outside effects in the idealized bay case must be applied to the model of Conception Bay. In particular, the condition $\eta_x = 0$ must be properly applied to the "upstream" boundary so that spurious waves and mass fluxes are avoided.

Figure 3.15 shows the coastline used in the model. The coordinate system has been rotated 30° from north into bay coordinates so that the Bay fits more efficiently into a rectangular grid. The "downstream" boundary should be placed a reasonable distance from the mouth to ensure that Kelvin waves exit the model domain perpendicular to the boundary, since, strictly speaking, the radiation condition applies to waves propagating perpendicular to the boundary only (see section 3.6). Therefore, an artificial, straight stretch of coastline is placed to the right of Cape St. Francis on the east side of the mouth so that Kelvin waves leaving the bay will have space to become aligned perpendicular to the boundary.

As demonstrated previously, the proper placement of the condition $\eta_x = 0$ on the left boundary is essential for attaining an acceptable solution. The model must not assume any information about regions "upstream" of the bay. Therefore, an implementation consistent

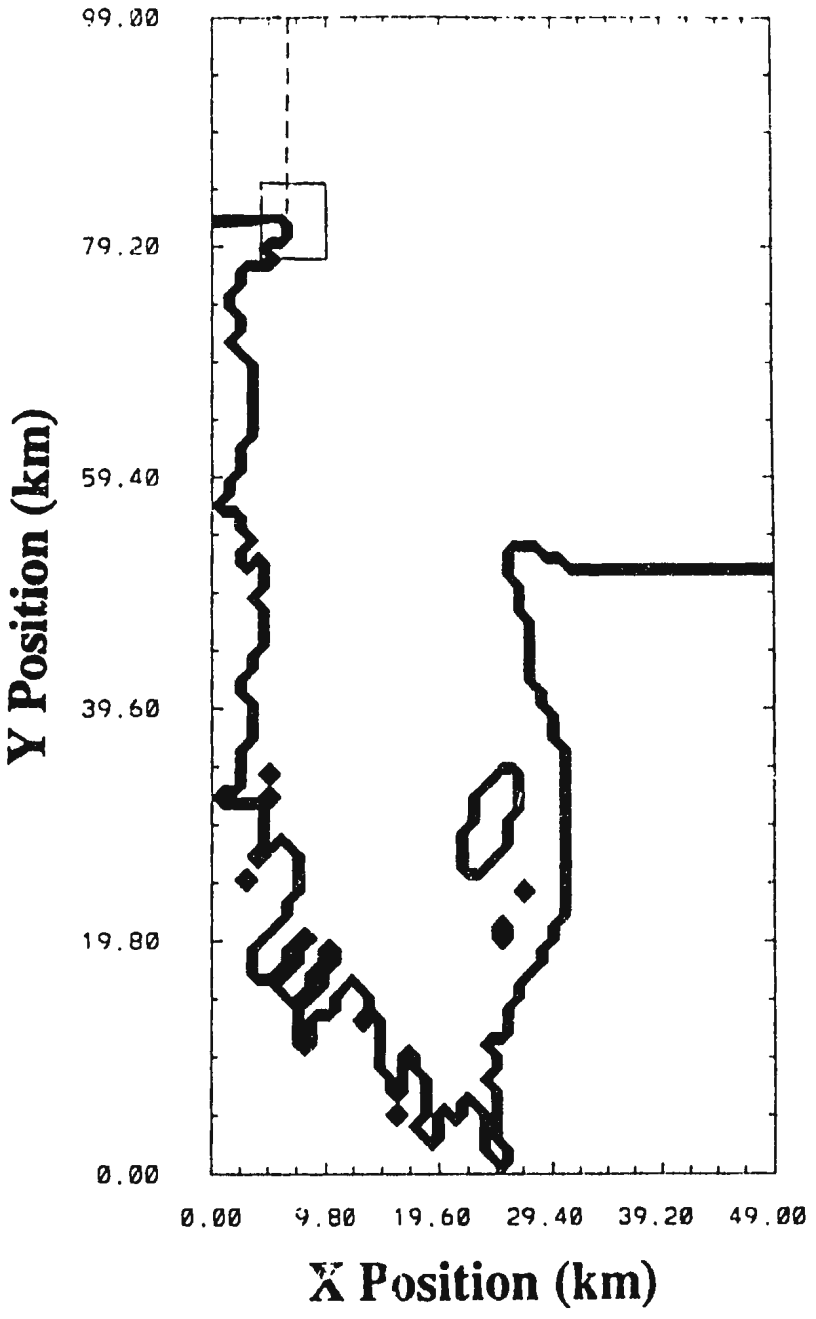

Figure 3.15 Model domain used to simulate Conception Bay. An artificial stretch of straight coastline has been added to the east of Cape St. Francis. North of 82 km on the western shore, the dashed line represents the position of the boundary condition $\eta_x = 0$. An enlargement of the region where the $\eta_x = 0$ boundary condition meets the coastline (denoted by the box) is shown in Figure 3.16.

with that successfully demonstrated in section 3.8 for the idealized bay must be applied to the real coastline. Figure 3.16 shows the C-grid with the H-array for the area where the $\eta_r = 0$ condition will meet the left side of the mouth. The tip of the cape separating Conception Bay and Trinity Bay is located at the H point $(6\frac{1}{2}, 81\frac{1}{2})$. Therefore the condition $\eta_r = 0$ must be applied at this point and upwards to the top open boundary to ensure that effects from Trinity Bay are avoided. Following the numerical implementation discussed in section 3.8 and shown in Figure 3.9, put $\eta_{6,j} = \eta_{7,j}$ and $v_{6,j-\frac{1}{2}} = v_{7,j-\frac{1}{2}}$ for $j \geq 82$, and let $u_{6\frac{1}{2},81}$ be set to zero by the masking. Values of u, v, and η left of $i = 6$ and north of the cape will not influence the solution.

The domain size is chosen to be 100 km long by 50 km wide in order to accomodate the bay which is 83 km long by 32 km wide at a grid resolution of 1 km in each direction. This means that the top and right radiation boundaries will be about 18 km from the mouth. For the case of the idealized bay, the reason for placing the boundaries at least 40 kilometers from the mouth was to include the inertial Kelvin waves that were an important part of the solution. Since the wind stress has been low-pass filtered (see below), the inertial oscillations present in the idealized bay will not be a significant part of the solution after initial transients die away. Experimentation using realistic, filtered wind has shown that moving the boundaries out another 10 km or more has no noticeable effect on the solution.

3.11: Model Wind Stress

As discussed in the previous chapter, wind stress is calculated from wind velocity measurements made at the St. John's airport. Hourly velocity measurements are converted to wind stress following Large and Pond (1981). Stress over the bay is assumed to be uniform

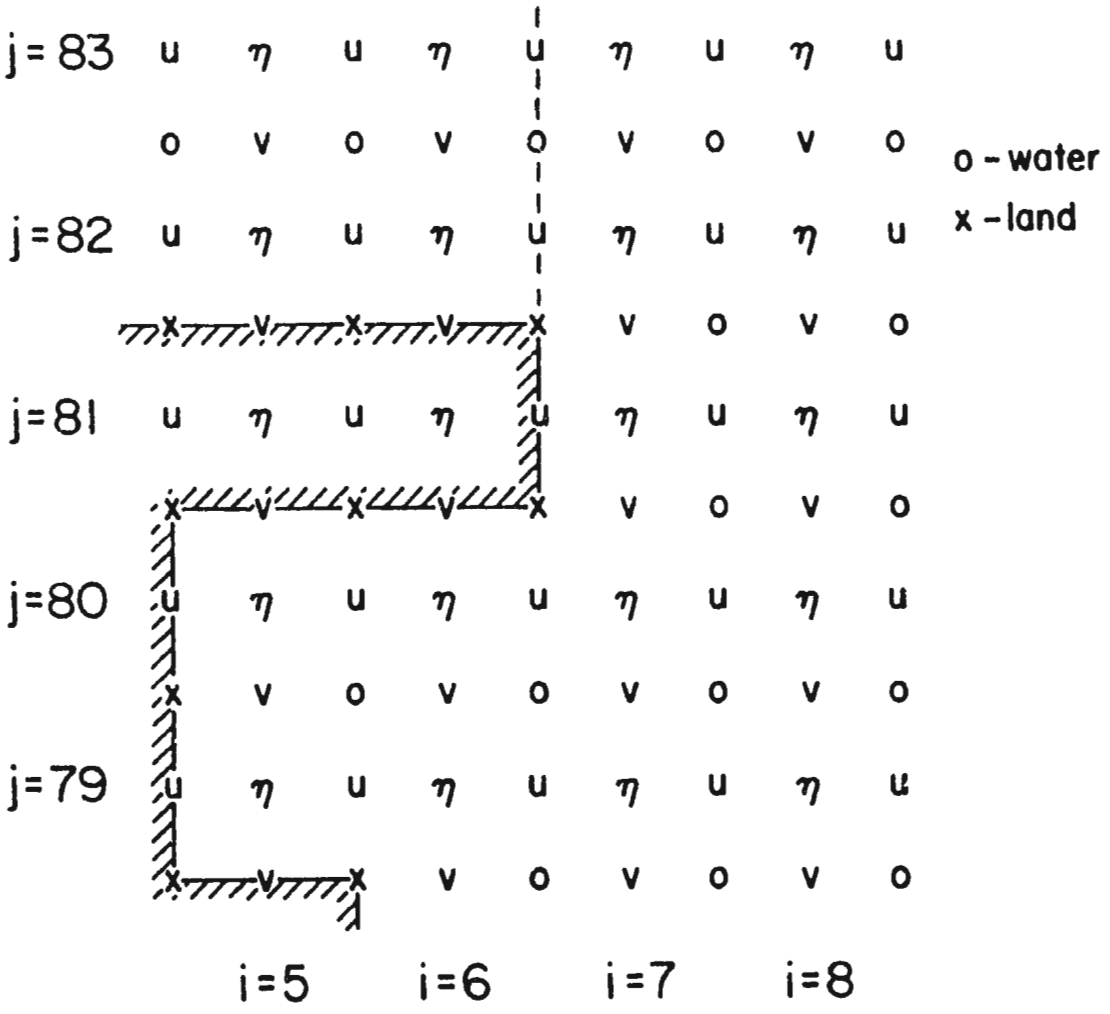

Figure 3.16 C-grid at corner where $\eta_x = 0$ condition meets the land. O is a water // point and × is a land // point. See Figure 3.9 for comparison with the idealized case.

and has not been corrected for orographic or frictional effects. Stress has been filtered to remove all energy with frequencies greater than one cycle per day thereby eliminating the presence of high frequency energy (i.e. frequencies > 1 cpd) in the model, except that energy present due to the initial startup.

3.12: Model Time Step

To allow easy interpolation of the wind stress record for use in the model, a fixed time step should be chosen. The stability criterion (see section 3.3) states that

$$\sqrt{2}c\frac{\Delta t}{\Delta s} \leq 1. \tag{3.18}$$

The maximum propagation speed present in model runs using realistic forcing will be 0.62 ms^{-1}. For Δs = 1 km and c = 0.62 ms^{-1}, the maximum allowable time step is approximately 19 minutes. A time step of 15 minutes is chosen to allow easy interpolation of the hourly wind data.

3.13: Friction and the Effects of Startup

Friction can be added to the model to remove information about the initial conditions. Since we are interested in using friction for this purpose only and not to realistically mimic turbulent mixing processes in the ocean, a simple, linear friction is adequate. As in section 3.9, the terms $-\epsilon u$ and $-\epsilon v$ are added to the right hand sides of (3.1) and (3.2), respectively, and $-\gamma\eta$ is added to the right side of (3.3). ϵ and γ are equal to one another and, unlike the sponge case, uniform over the model domain.

We desire a model such that the solution at a certain time during an integration is not dependent on the time the model was started. The effect of the initial conditions

can be examined by starting the model at different times during the year and comparing the solutions. Figure 3.17 shows model interface displacements at the model grid point corresponding to mooring 1 in 1990 (see Figure 2.12). Each plot shows time series of model runs beginning at 150, 155, and 160 days and ending at approximately 202 days. The models are driven by realistic, filtered wind from the year 1990. For Figure 3.17a, ϵ and γ are zero. The solutions after 165 days are essentially identical except for the presence of high-frequency energy caused by the startup. Friction can be added to the model to remove this high-frequency energy. In Figure 3.17b, the addition of a small amount of friction ($\epsilon = \gamma = 1/10$ days) has removed the high-frequency signal while having a negligible effect on the long-period signal. The high-frequency noise in Figure 3.17a is removed on a time scale set by the friction parameter (i.e. 10 days for this case). The long period signal, however, is hardly affected by friction, since it is associated with Kelvin waves. These waves take only about 3 days to propagate around the Bay and are, therefore, present in the model domain for less than the frictional decay period. The long-period oscillations in Figure 3.17 are associated with the $\sim$8 day period onset and relaxation of a northeastward wind.

As mentioned previously, the friction used in this model is not meant to realistically mimic loss of energy due to mixing. However, we can estimate a realistic value for the linear friction coefficient ϵ necessary to model energy loss due to vertical mixing on the Newfoundland shelf region. By modelling vertical mixing of momentum with a term $\frac{\partial}{\partial z}(\nu\frac{\partial u}{\partial z})$, the

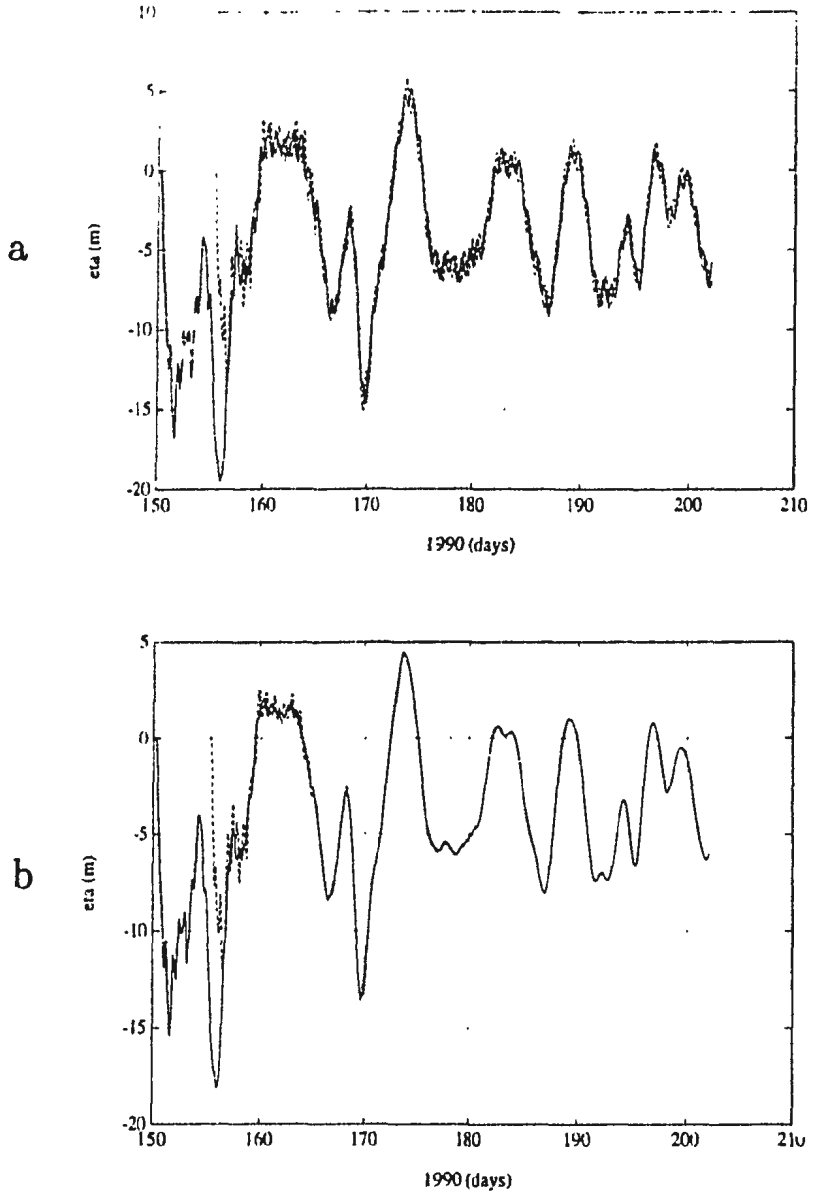

Figure 3.17 Time series of interface displacement (in meters) at the grid point corresponding to mooring 1 in 1990 for model runs used to test the dependence on initial conditions. $g' = 4.8 \times 10^{-3}$ ms^{-2} and $H_1 = 50$ meters. $\epsilon = \gamma = 0$ in Figure 3.17a, and $\epsilon = \gamma = 1/10$ days in Figure 3.17b. The model is forced with wind stress from 1990. Solid lines represent the model run from day 150 to 202, dashed lines represent the model run from day 155 to 202, and the dotted lines represent the model run from day 160 to 202. Note that the dotted lines are difficult to see, since they coincide well with dashed and solid lines.

value of ϵ necessary to have an equivalent amount of mixing can be found by using the concept of vertical normal modes. For the first baroclinic mode, the relation is given by

$$\epsilon = \frac{\nu\pi^2}{H^2}, \tag{3.19}$$

where H is the depth of the bay (Martinsen and Weber, 1981; McCreary, 1981). Following Csanady (1976), we estimate ν using the formula $\nu = C'_D q^2/(200f)$, where C'_D is a drag coefficient and q is a representative velocity. Substituting values of $C'_D = 7 \times 10^{-3}$ and $q = 0.1$ ms^{-1} appropriate to our case, we get ν is equal to 3.5×10^{-3}m^{2}s^{-1}. Using this value of ν and $H = 200$ m, we find ϵ would have to be $\sim 1/13.5$ days days to mimic observed vertical mixing. This value of ϵ is similar to that used in the model and has a decay scale greater than the time it takes an internal Kelvin wave to propagate through the Bay. Therefore, Kelvin waves present in Conception Bay are not expected to be strongly affected by vertical mixing. Scattering by the irregular bottom topography of the Bay is likely to be much more important.

3.14: Linear Nature of the Model

The model described in this chapter is linear; that is, all the non-linear terms are assumed to be small and have been removed from the equations of motion. Removing the non-linear terms simplifies the equations and allows for easier numerical implementation. The assumption that the non-linear terms are small is accurate as long as two criteria are satisfied. The nonlinear continuity equation has been linearized (i.e., equation (3.3) is the linearized version) by assuming $|\eta| \ll H_1$; therefore, the linear equation is valid as long as this criterion is satisfied. The linearized momentum equations (i.e., equations (3.1) and

(3.2)) will be accurate when the non-linear terms (i.e., $(\vec{u} \cdot \nabla)\vec{u}$) are small compared with the rotational and acceleration terms. This is true when $c \gg U$, where $c = (g' H_1)^{1/2}$ and U is a characteristic model velocity. In general, these two criteria are satisfied most of the time, but are violated occasionally.

The behavior of the model is dependent on several different parameters. These include c, f, γ, ϵ, τ^x, τ^y, and the model geometry (including boundary conditions). To explore the dependence of velocity and η upon g', H_1, and wind stress, equations (3.1) - (3.3) can be non-dimensionalized. Since our model response is dominated by low-frequency Kelvin waves, we can look at a bay with a straight coastline at $y = 0$ and a constant τ^x to approximate the response of the Bay. The term containing τ^y can be dropped by setting the cross-shore wind stress to zero. At the coast itself, terms with v can be dropped since flow normal to the boundary is zero. With these simplifications, the equations (3.1) and (3.3) reduce at the coast to

$$\frac{\partial u}{\partial t} = -g' \frac{\partial \eta}{\partial x} + \frac{\tau^x}{\rho_1 H_1}, \tag{3.20}$$

$$\frac{\partial \eta}{\partial t} + H_1 \frac{\partial u}{\partial x} = 0. \tag{3.21}$$

For dimensional analysis, the length of the bay side L is the along-shore length scale, and the time scale is L/c (i.e., the time it takes a Kelvin wave to propagate a length L). Using 3.20 to solve for the scale of u after the passage of the Kelvin wave, we find that

$$\begin{aligned} u &= O\left(\frac{\tau^x L}{\rho H_1 c}\right), \\ \eta &= O\left(\frac{\tau^x L}{\rho c^2}\right), \end{aligned} \tag{3.22}$$

where the relationship for η can be found using (3.21) once an equation for the scale of u is known. The amplitude of the response (i.e., η, u, v) is linearly related to the magnitude of the wind forcing. The interface displacement, η, depends not directly on g' or H_1, but their combination c. The solution of the upper-layer velocity depends on c as well; however, the amplitude is inversely related to H_1 (i.e., doubling H_1, while keeping c constant, reduces u and v by half). These relations have been verified using various values of g', H_1, and wind stress in the model. Therefore, a variety of stratifications can be described by a single value of c, as long as the velocity is scaled properly.

3.15: Effects of Smoothing Coastline

As mentioned in the previous section, the model solution will depend partially on the shape of the coastline. The smoothed coastline in Figure 3.18 can be used to evaluate the influence of the rugged features present in the coastline in Figure 3.15. For a stratification with $g' = 7.2 \times 10^{-3}$ ms^{-2} and $H_1 = 40$ meters, the Rossby radius is approximately 5 km. Since the length scale of the features smoothed is equal to and smaller than the Rossby radius, the general shape of the model response is not expected to be affected by smoothing the coastline. Figure 3.19 shows time series of the interface displacement for the model runs with smoothed and unsmoothed coastlines for $g' = 7.2 \times 10^{-3}$ ms^{-2}, $H_1 = 40$ meters, and $\epsilon = \gamma = 1/10$ days. While the general shape is not changed, smoothing the coastline has affected the signal in two ways. First, the amplitude of the interface displacement is altered slightly, since the position of the grid points relative to the coast has changed. Second, the length of coast which the Kelvin wave must propagate along is reduced by smoothing, and thus, information is transmitted more quickly by Kelvin waves. This results in a phase lag

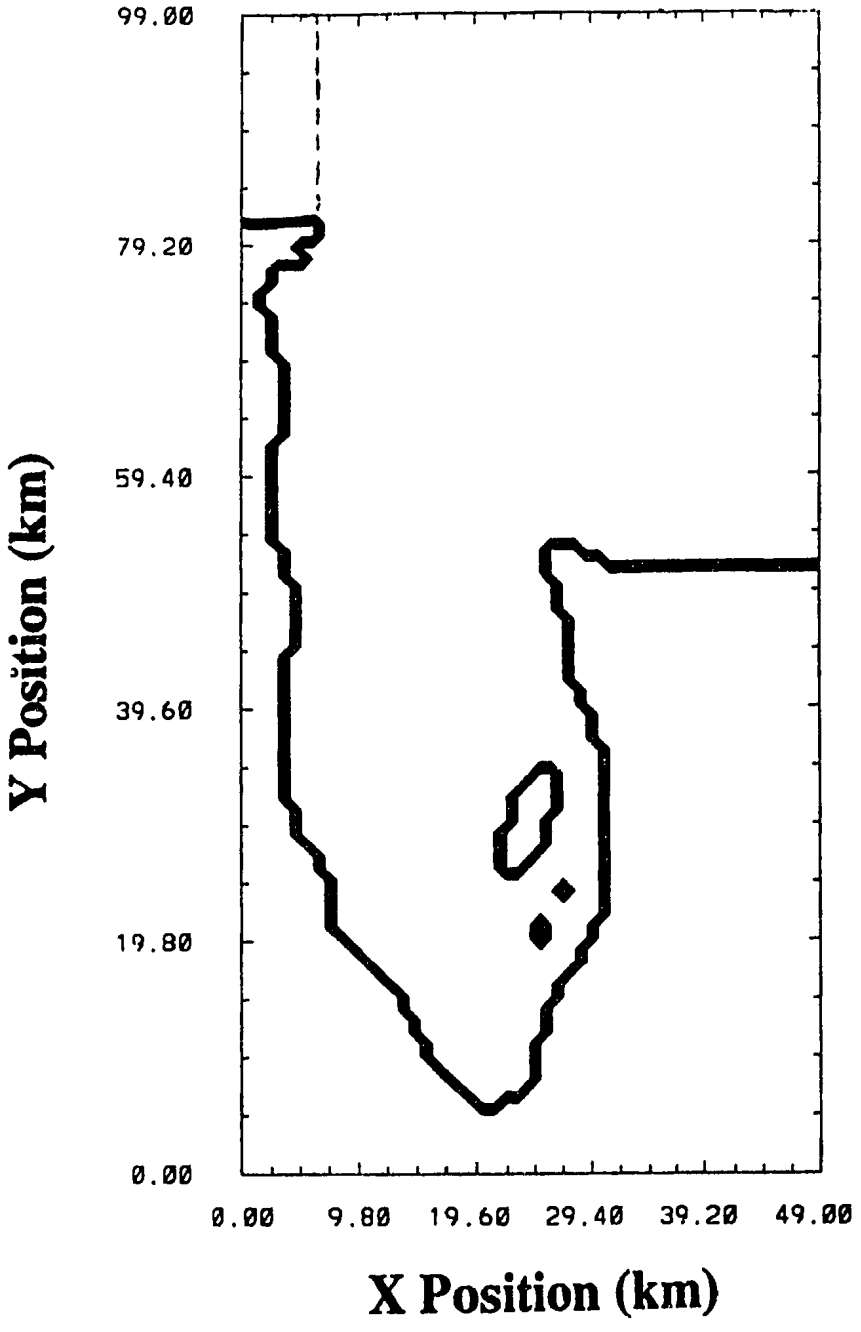

Figure 3.18 Model domain with smoothed coastline

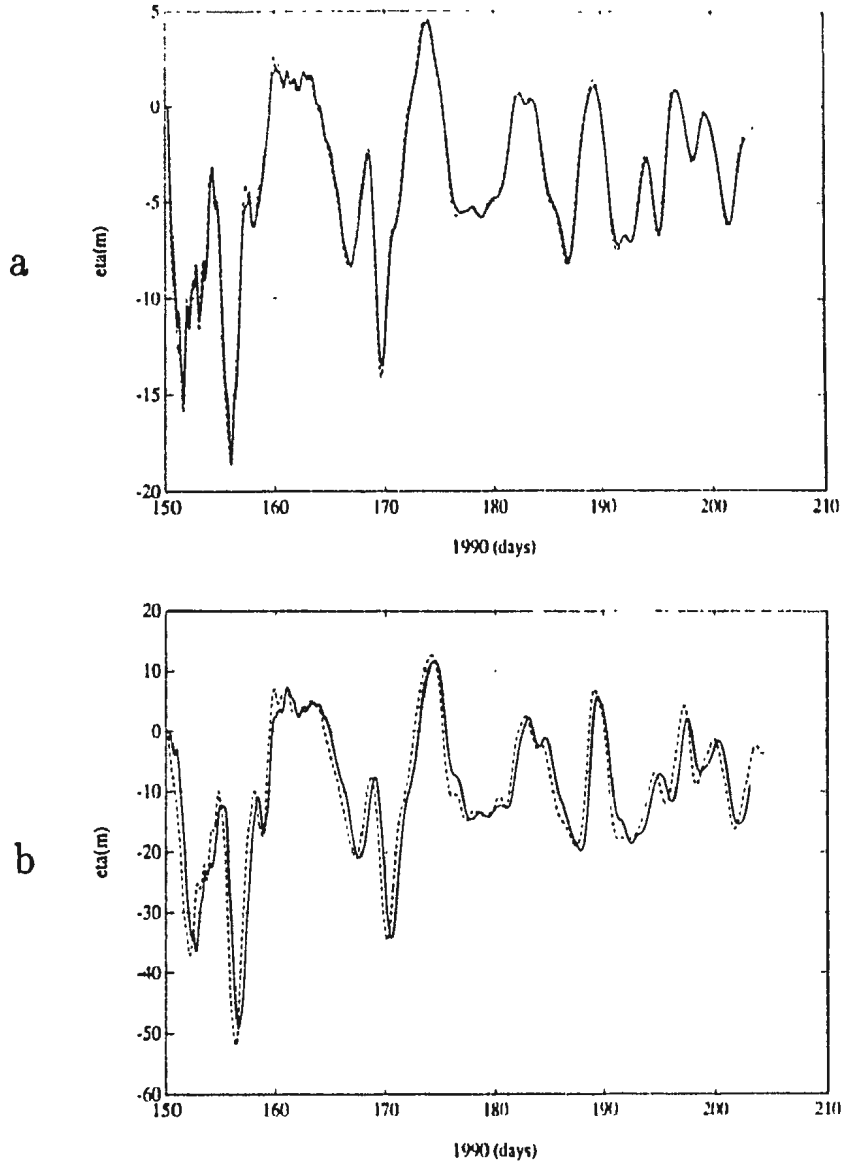

Figure 3.19 Time series of interface displacement (in meters) for the cases of smoothed and unsmoothed coastlines. The model is forced with wind stress from 1990. $g' = 7.2 \times 10^{-3}$ ms^{-2}, $H_1 = 40$ meters, and $\epsilon = \gamma = 1/10$ days. Solid lines represent the unsmoothed case, and dashed lines represent the smoothed case. Displacements at mooring 1 for 1990 are shown in Figure 3.19a, and displacements at mooring 4 for 1990 are shown in Figure 3.19b.

between the smoothed and unsmoothed cases that increases in the "downstream" direction around the head. Both effects are negligible for present purposes.

CHAPTER 4: EVALUATION OF THE WIND-FORCED RESPONSE

The primary goal of this thesis is to determine whether a wind forced 1-1/2 layer model can reproduce the variability in the temperature field in Conception Bay. Comparison between observed temperature data and model output will establish the effectiveness of the model. The structure of the current field and its correlation with the modelled currents and the wind are also examined. These analyses will help determine the response of the Bay to wind forcing. Data have been collected at the mouth (1989 data) and near the head (1990 data). Analysis of these two sets of data will show how differently the two regions behave.

4.1: Initial Startup of the Model

The accuracy of the model can be affected by transients generated at the startup of the integration as was mentioned in section 3.12. Suddenly applying wind forcing to the model will generate energy at all frequencies. This can be a particular problem at the inertial period ($\sim$16 hours), where a large response can be generated since it is a resonance period for the system. The energy generated at startup can be reduced by linearly increasing the wind stress from zero at the start to its actual value after some period. However, applying a linear ramp to the wind is not essential, since the nature of the model is such that most energy is propagated out of the bay as Kelvin and Poincaré waves, thus most of the energy present due to startup will eventually propagate out of the model domain. The model runs shown in Figure 3.17 use a wind turned on suddenly (i.e. without a ramp) at three different times to show the effects of startup. The similarity of the signals at later times shows that the startup noise propagates out of the bay quickly. Relatively weak friction, $\epsilon = \gamma = 1/10$ days, is used to damp out trapped energy present due to startup. Filtering of the wind

also helps to reduce these effects by removing high-frequency events (i.e. periods less than a day).

4.2: Stratification Used in the 1-1/2 Layer Model

The stratification of Conception Bay changes throughout the year, as was shown in Chapter 2. At the beginning of spring, the vertical profiles of temperature, salinity, and density are nearly homogeneous; stratification is weak. Heating at the surface during the spring and summer and an influx of fresh-water reduce the density at the surface, and this less-dense water is mixed downwards. To model Conception Bay as realistically as possible using a 1-1/2 layer model, values of upper layer depth and reduced gravity representative of measured conditions in Conception Bay should be used. Figure 2.8 shows individual vertical density profiles taken at BRLP 5 (see Figure 2.2 for location of BRLP 5) on 5 days in 1989 and 1990. For 1989, the period for which current meter and thermistor chain data are available for comparison is from 107 to 303 Julian days. For 1990, current and temperature were measured from 120 to 203 Julian days. However, since the upper layer does not develop until approximately 150 Julian days, our period of interest begins at about day 150.

Figure 2.8 can be used to estimate the upper- and lower-layer densities and the upper-layer depth during 1989. In all three plots, the lower-layer density, ρ_2, is approximately 1026.5 kgm^{-3}. The upper layer depth and density must be estimated since the pycnocline has significant vertical extent. At 150 Julian days, the upper layer is roughly 10-20 meters deep and has a density of 1025.5-1026.0 kgm^{-3}. For this stratification, the internal Kelvin wave speed c is $\sim$ 0.4 ms^{-1}, and the Rossby radius of deformation is $\sim$4 km meaning that

Kelvin waves are adequately resolved by the 1 km grid used in the model. As the year progresses, the depth of the pycnocline increases, and the pycnocline thickens. At day 181, the upper layer is roughly 20-30 m, and its density is 1025.5-1026.0 kgm^{-3}. By day 250, the pycnocline has deepened to approximately 50 m, and the upper layer density is roughly 1025.5 kgm^{-3}. At this time, the wave speed c is ~ 0.7 ms^{-1}, and the Rossby radius is ~ 7 km and, thus, well-resolved.

Figure 2.8 also shows the density profiles at BRLP 5 at days 148 and 173 in 1990. At day 148, the profile shows two distinct layers that closely resemble the 1-1/2 layer assumption. The period of interest is roughly 50 days in 1990 running from 150 to 203 Julian days. The profile at the center of that period, day 173, shows that the upper-layer density is 1025.5 - 1026 kgm^{-3}, and the upper-layer depth is roughly 25 m. For this stratification, the wave speed c is ~ 0.45 ms^{-1}, and the Rossby radius is ~ 4.5 km. These values of density and upper-layer depth will be used to approximate the stratification in the 1-1/2 layer model. A range of stratifications will be used in the model to determine which values give best agreement with the observations.

4.3: Analysis at the Mouth of the Bay for 1989

We begin by examining data available at the mouth of the Bay for the year 1989. Comparison with model results will show how closely the Bay approximates a wind-forced, 1-1/2 layer ocean. Deviation between the model and the observed data will give an estimate of the degree to which influences other than wind effect the Bay. The upper-layer response may be influenced by Kelvin waves generated in Trinity Bay, or elsewhere outside Conception Bay, that will propagate into the Bay and have the greatest influence near the mouth, especially

closest to shore at mooring 3 (see Figure 2.9). Also, baroclinic instabilities generated by the Labrador Current which have been observed in the Avalon Channel (Anderson, 1986), will certainly affect the upper layer of Conception Bay if they enter the Bay.

A series of model runs were performed starting at several times in the year and for various lengths of time. The model current at M3 is recorded at hourly intervals for comparison with observed current and the wind stress. Model interface displacement at M3, M4, and M5 are recorded at hourly intervals for comparison with temperature measured by the thermistor chains. Measurements of temperature show that temperature decreases with depth in the same manner that density increases with depth: the two are strongly correlated. Upwards (downwards) movement of the pycnocline will result in a decrease (increase) in temperature at a fixed depth. Thus, comparison between model interface displacement and observed temperature provides a means of determining the ability of the model to reproduce variability in the upper layer.

Spectral analysis is used to evaluate the correlation between two scalar time series. (See Jenkins and Watts (1968) for a more complete discussion of spectral analysis.) The spectral analysis used in this thesis employs Fourier transforms to convert a signal in the time domain into its components in the frequency domain. The frequency components can then be compared to determine the similarity of the two signals. The time series must be broken into sections and the spectrum averaged to attain statistically reliable results. The fact that the time series are of finite length places certain limitations on the analysis. Splitting the time series into smaller time series means that the longest resolvable period is reduced. On the other hand, increasing the number of sections increases the reliability

of the final spectrum. Therefore, the analysis must be done to maximize confidence while still resolving the low frequency signal. To attain a reliable time series, the final spectrum must have at least ten degrees of freedom, where the number of degrees of freedom is equal to twice the number of sections into which the time series is divided .

The end results of the spectral analysis are two functions that describe the agreement of the two time series as a function of frequency. One is called (coherence)^2, which measures the correlation at individual frequencies between two signals. The other measures the phase difference between the two time series. A criterion for determining whether a certain value of (coherence)^2 represents agreement between two time series is described by Jenkins and Watts (1968). The value of (coherence)^2 that is significantly different than zero, and therefore represents meaningful (coherence)^2, is a function of the degrees of freedom of the spectrum and the percent confidence desired. Values of (coherence)^2 required for significant coherence decrease with increasing degrees of freedom and decreasing percent confidence.

Comparisons between model interface displacement and observed temperature from the thermistor chains at approximately 25 meters are performed for the 3 stations across the mouth of the Bay for 1989. Note that positive η is measured downwards so decreasing η corresponds to upwelling and that a decrease in temperaure at a fixed depth corresponds to upwelling. Temperatures used for the comparison are taken from thermistor chain measurements at approximately 25 meters depth. Figure 4.1 shows the interface displacement at M3 for the model run from 160 to 266 days ($g' = 9.6 \times 10^{-3}$ ms^{-2}, $H_1 = 40$ m, $\epsilon = \gamma =$ 1/10 days), the temperature at M3, and the cross-spectrum between the two time series. By choosing constant values of g' and H_1, we are assuming that the stratification does not

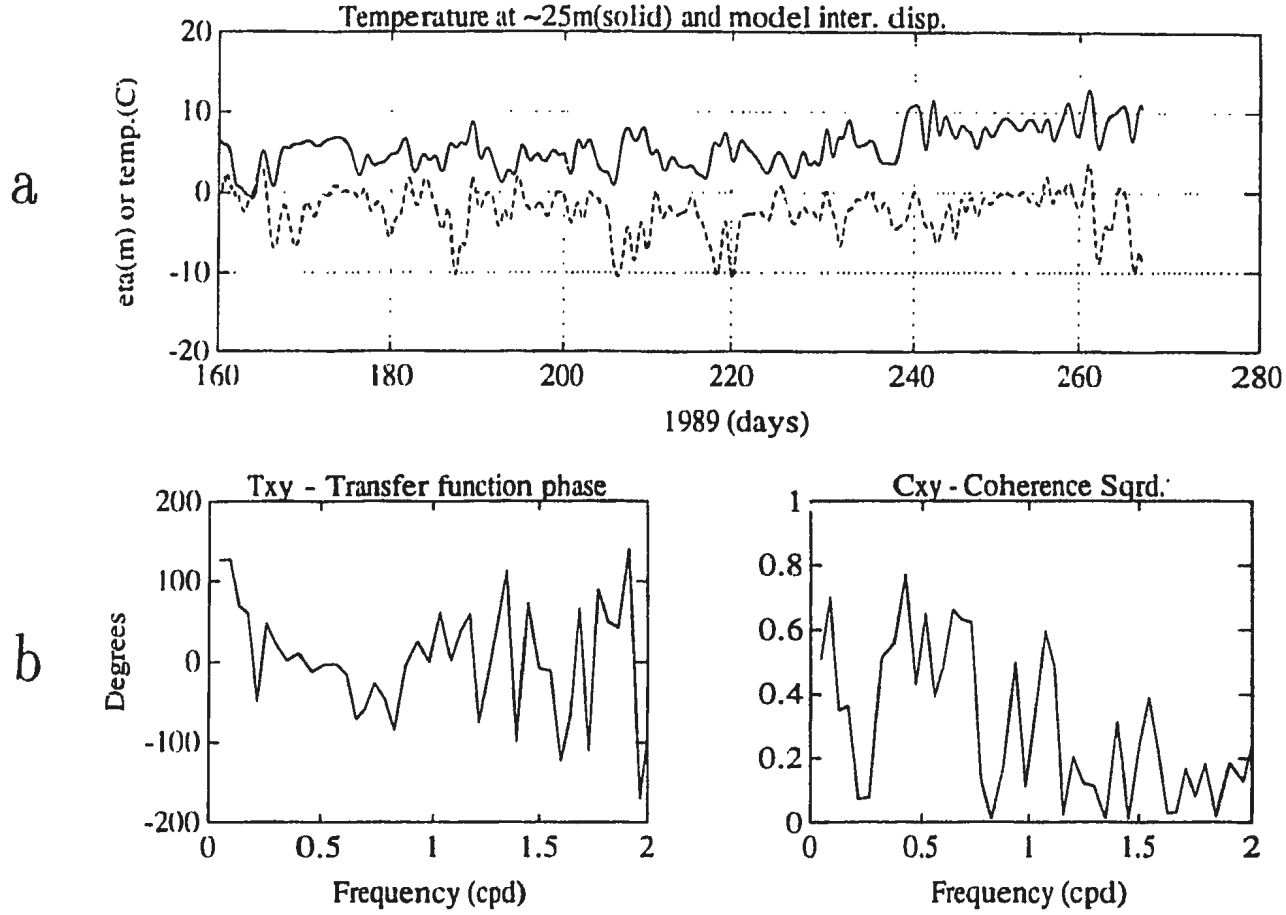

Figure 4.1 (a) Model interface displacement (in meters) at M3, and temperature (in °C) at ~25 meters at M3 (b) Cross-spectral phase difference and cross-spectral (coherence)^2 between interface displacement and temperature. Model is run from 160 to 266 days with $g' = 9.6 \times 10^{-3} \mathrm{ms}^{-2}$, $H_1 = 40$ m, and $\epsilon = \gamma = 1/10$ days. Cross-spectrum has ten degrees of freedom, and values of (coherence)^2 greater than 0.59 are significant at the 90% confidence level.

change during the integration. The stratification does, of course, change with time, as has been shown. A variety of stratifications have been tried, and these values of g' and H_1 provide the best results. Mooring 3 is located three kilometers from the shore and should have the strongest Kelvin wave signal of the three moorings, since the amplitude of Kelvin waves decays exponentially away from the shore on the order of the Rossby radius (~6 km). For this spectral analysis, the time series are divided into 5 sections (also called bins) of 512 hours each so that the longest resolvable period signal is 21.3 days and significant (coherence)^2 for 90% confidence is 0.59. Agreement between the two time series is not great, but there is still significant coherence at 0.1 and 0.5 cpd. At 0.1 cpd, the plot of phase shows that the two signals are out of phase as can be observed in the time series (eg. days 205-225). Near 0.5 cpd, three significant peaks with excellent phase agreement ($< 10°$) are present. A spectrum computed using 20 degrees of freedom also shows significant coherence at 0.5 cpd. The agreement between the two series at a two day period is apparent in the time series in Figure 4.1a.

Figure 4.2 shows the interface displacement at M4 for the same model run, temperature at ~25 meters at M4 and their cross-spectrum. Comparison of the model interface displacements at M3 and M4 show that the two time series are essentially the same with a reduction in amplitude at M4 showing that the model is dominated by Kelvin waves. At this station there appear to be no similarities between the model interface displacement and observed temperature. The cross-spectrum between the two time series has lower coherence than at M3 with no significant coherence at any frequencies, except for a spike of 0.7 at 0.45 cpd. However, since the phase is highly varied at 0.45 cpd, the time series do not agree

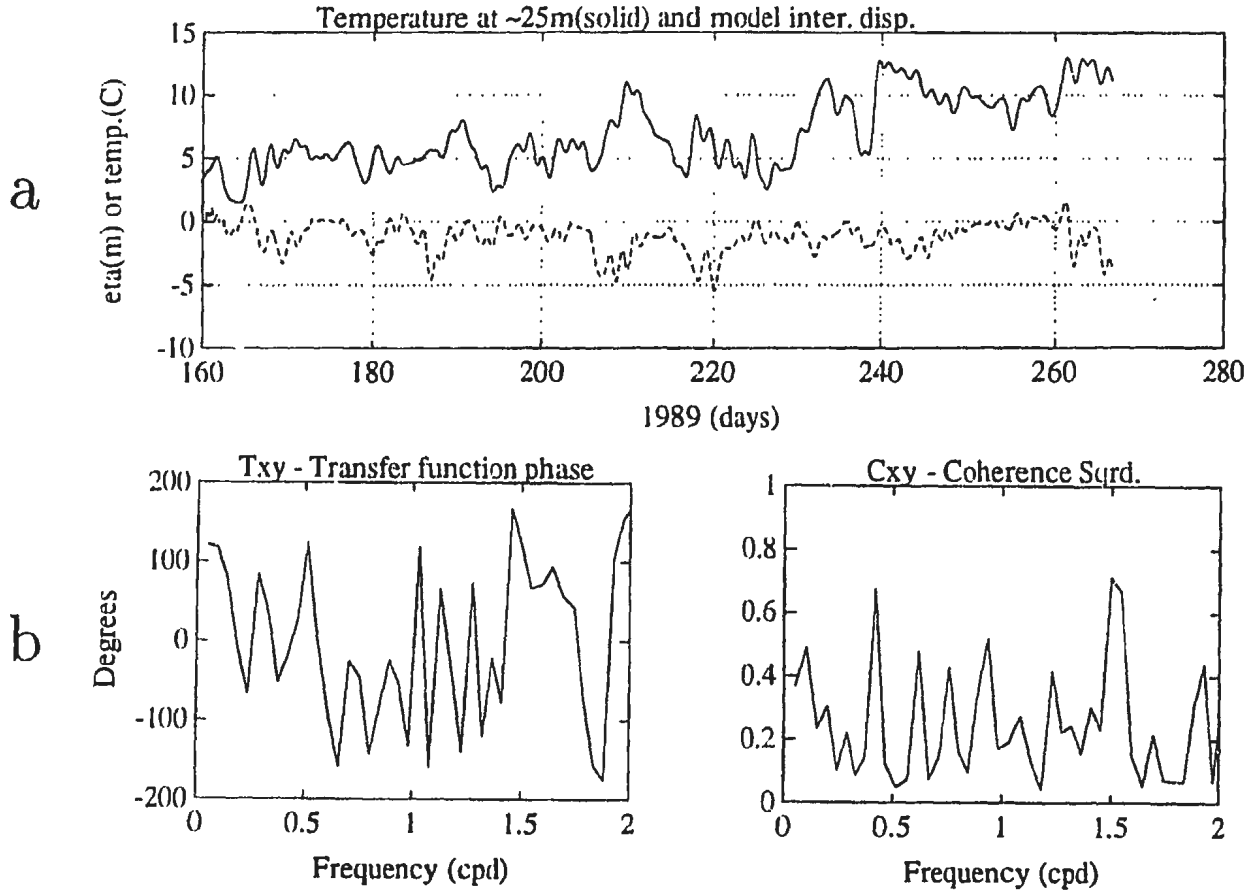

Figure 4.2 Same as Figure 4.1, except that the plots are for M4, instead of M3. Note the different labelling of the ordinate axis in part (a).

at this frequency. In general, significant coherence in cross-spectra is more reliable when it is present over a broad range of frequency and associated with a flat region of phase difference: therefore, a spike in coherence combined with rapidly fluctuating phase as is present in Figure 4.2 at 0.15 cpd does not necessarily represent meaningful agreement.

Model interface displacement at M5, observed temperature at ~25 meters at M5, and their cross-spectrum are shown in Figure 4.3. The two time series are not similar. In the cross-spectrum, the coherence is low, and the phase varies greatly. Significant coherence is limited to one spike of 0.6 at a frequency of 0.5 cpd.

Although coherence between model interface displacement and temperature at M3 is not high, agreement at M4 and M5 is worse. The Kelvin wave signal generated in the Bay will be stronger at M3 than at M4 and M5, since M3 is closer to the shore. This would explain why the model is more successful at reproducing the temperature signal at M3. Differences between the model and observations at all 3 moorings can be ascribed to the likely importance of external forcing, either from upstream as Kelvin waves from Trinity Bay or as baroclinic instabilities from the Labrador Current (Anderson,1986).

Comparison of temperature with model output has already shown that the temperature field at the mouth is not behaving like a wind-forced, 1-1/2 layer ocean. Direct comparison between temperature at M3 and the wind stress can provide another means of deciding whether the wind is forcing temperature variabilility at the mouth. Figure 4.4 shows temperature at M3 and the wind stress from 160 to 266 days. The figure also shows the cross-spectra of temperature versus the y-component of wind and of temperature versus

a

b

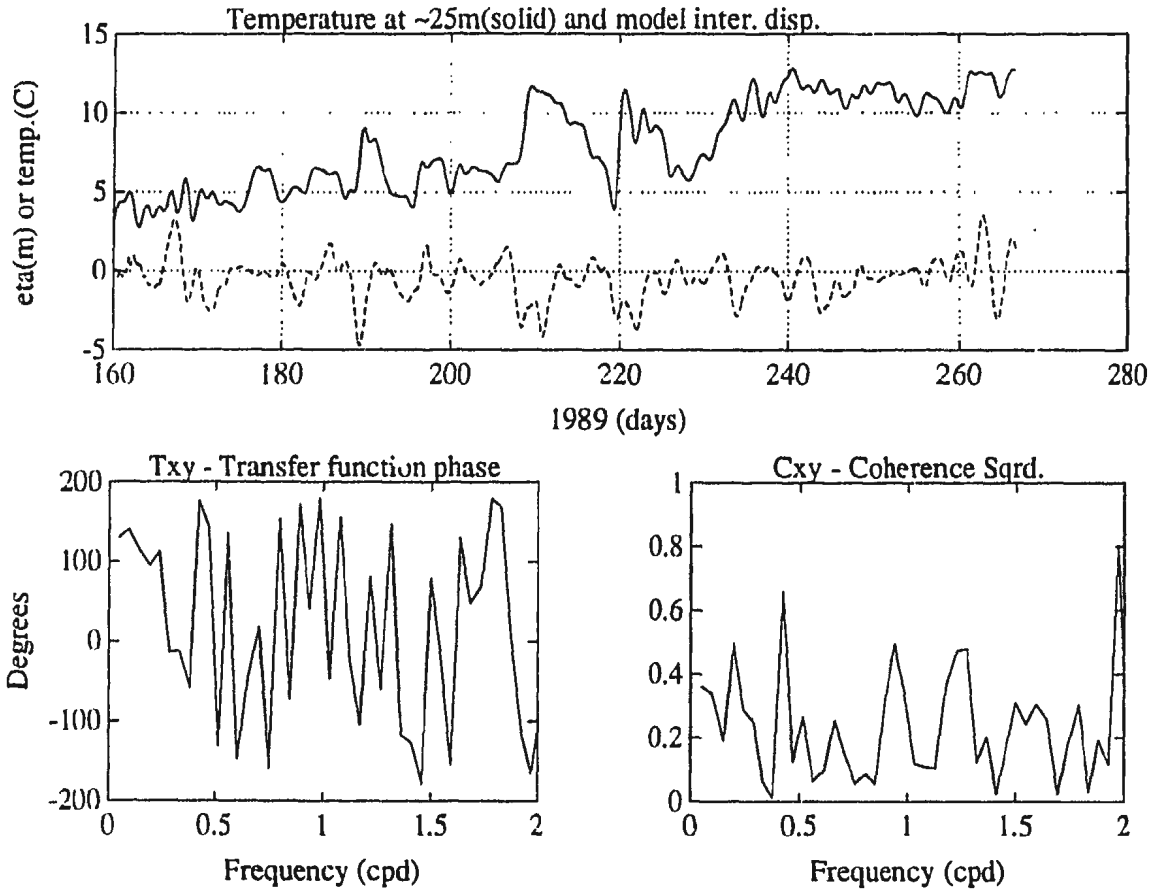

Figure 4.3 Same as Figure 4.2, except that the plots are for M5, instead of M4.

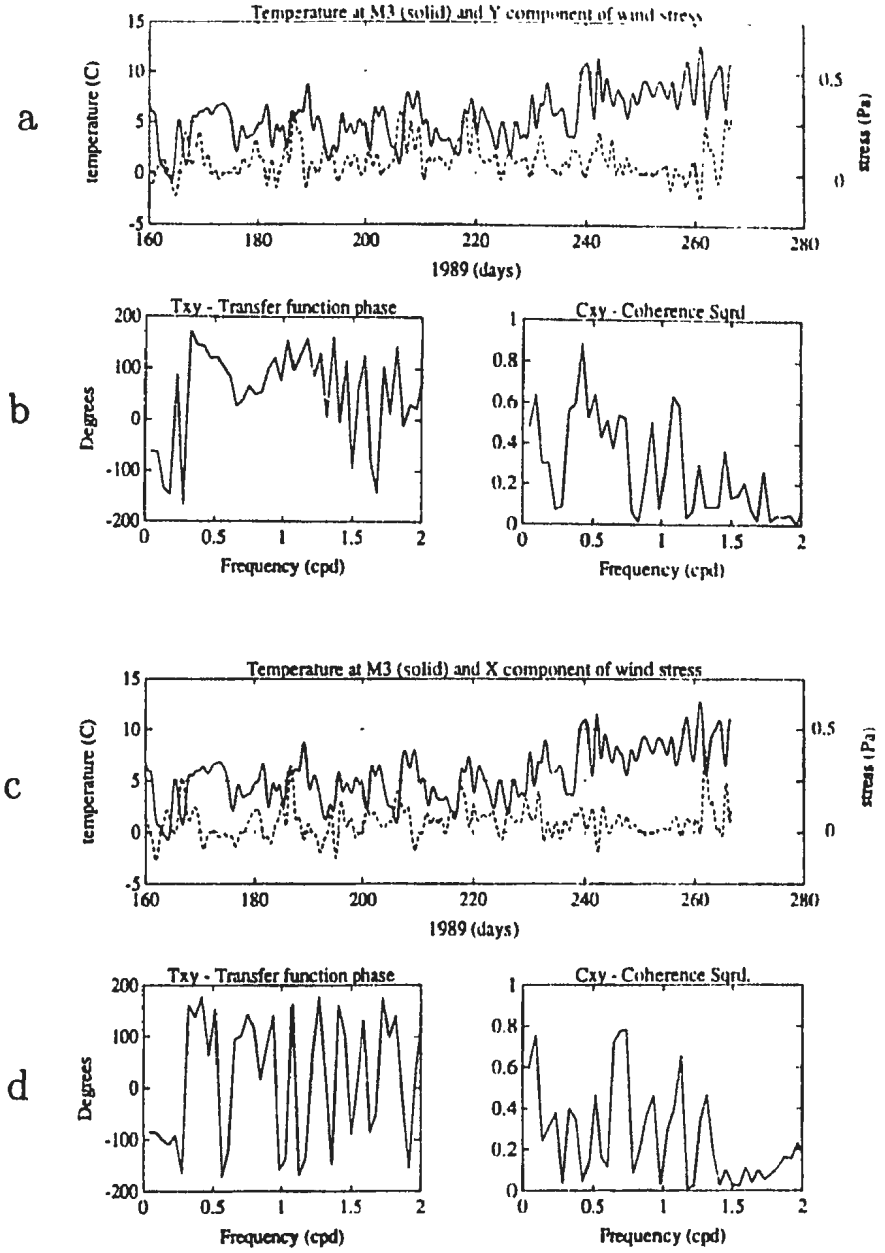

Figure 4.4 (a) Temperature (in °C) at ~25 meters at M3 and the y-component of wind stress (in Pa). (b) Cross-spectrum between temperature and y-component of wind stress. (c) Temperature (in °C) at ~25 meters at M3 and the x-component of wind stress (in Pa). (d) Cross-spectrum between temperature and x-component of wind stress. Spectra have ten degrees of freedom, and values of (coherence)^2 greater than 0.59 are significant at the 90% confidence level.

the *x*-component of wind. The *y*-component is nearly the along-shore wind stress ("along-shore wind stress" means the component of wind stress parallel to the shore near M3) and will correspond inversely to temperature if the Bay behaves as a 1-1/2 layer, wind-forced ocean. The cross-spectra have 10 ten degrees of freedom, and values of (coherence)^2 greater than 0.59 are significant at the 90% confidence level. The cross-spectrum between τ^y and temperature has significant coherence at 0.45 cpd. At 0.45 cpd, the temperature and the wind stress are out of phase as they would be if the Bay was responding as a 1-1/2 layer ocean. The cross-spectrum between temperature and τ^x has significant coherence at 0.1 and 0.75 cpd. The peak at 0.75 cpd is questionable, since 0.75 cpd is the cut-off frequency for the filter. Comparison between wind stress and temperature at M4 and M5 reveal no significant coherence. The cross-spectrum between τ^y and temperature shows remarkable similarity with the spectrum in Figure 4.1. Both have the highest coherence at ~0.5 cpd. Figures 4.1 and 4.4 indicate that a significant part of the temperature signal at frequencies near 0.5 cpd at the western side of the mouth is driven by the wind, while the response at other frequencies cannot be directly related to the wind.

The thermistor chain data can be used to provide another way of measuring the thermocline/pycnocline movement. Since the thermistor chain measures temperature at roughly 5 meter depth increments, the vertical position of an individual isotherm can be determined throughout the year. The depth of an individual value of temperature is found by starting at the bottom of the thermistor chain and searching up the column until a depth with the desired temperature is reached. This process is repeated for each time throughout the year, and the result is similar to the trace of an individual isotherm in Figure 2.11. The method

has its weaknesses in that the isotherm may be located above or below the vertical range of the thermistor chain and, also, the greatest depth with the desired temperature will always be chosen. Figure 4.5 shows the model interface displacement at M3 for the same run as in Figures 4.1, 4.2, and 4.3 ($g' = 9.6 \times 10^{-3}$ ms^{-2}, $H_1 = 40$ m, $\epsilon = \gamma = 1/10$ days), the position of the 1°C isotherm, and their cross-spectrum. The 1°C isotherm was chosen because it left the vertical range of the thermistor chain less often than other values of temperature. The flat regions at 50 meters on the plot are times when the 1°C isotherm went below the bottom of the thermistor chain. The 2° or 0°C isotherms could have been used since the motion of the isotherms is nearly identical as is apparent in Figure 2.11. The vertical motion of the isotherm is many times larger than the model interface movement. The spectrum has 10 degrees of freedom, and values of (coherence)^2 greater than 0.59 are significant at the 90% confidence level. Once again, the cross-spectrum reveals that the 0.5 cpd signal present in the temperature data is reproduced by the model. The only two significant peaks are at about 0.5 cpd with good phase agreement ($< 50°$). At lower frequencies, the signals become out of phase and coherence is poor.

Three different methods have shown that the temperature signal at M3 is significantly correlated with the wind forcing at a two day period. Direct comparison of wind stress and temperature as well as comparison of the model output with temperature at fixed depth in the pycnocline and with movement of an individual isotherm show best agreement at 0.5 cpd.

To determine the horizontal scale of temperature variability at the mouth of the Bay, spectral analysis between the temperature signals at the three moorings can be performed.

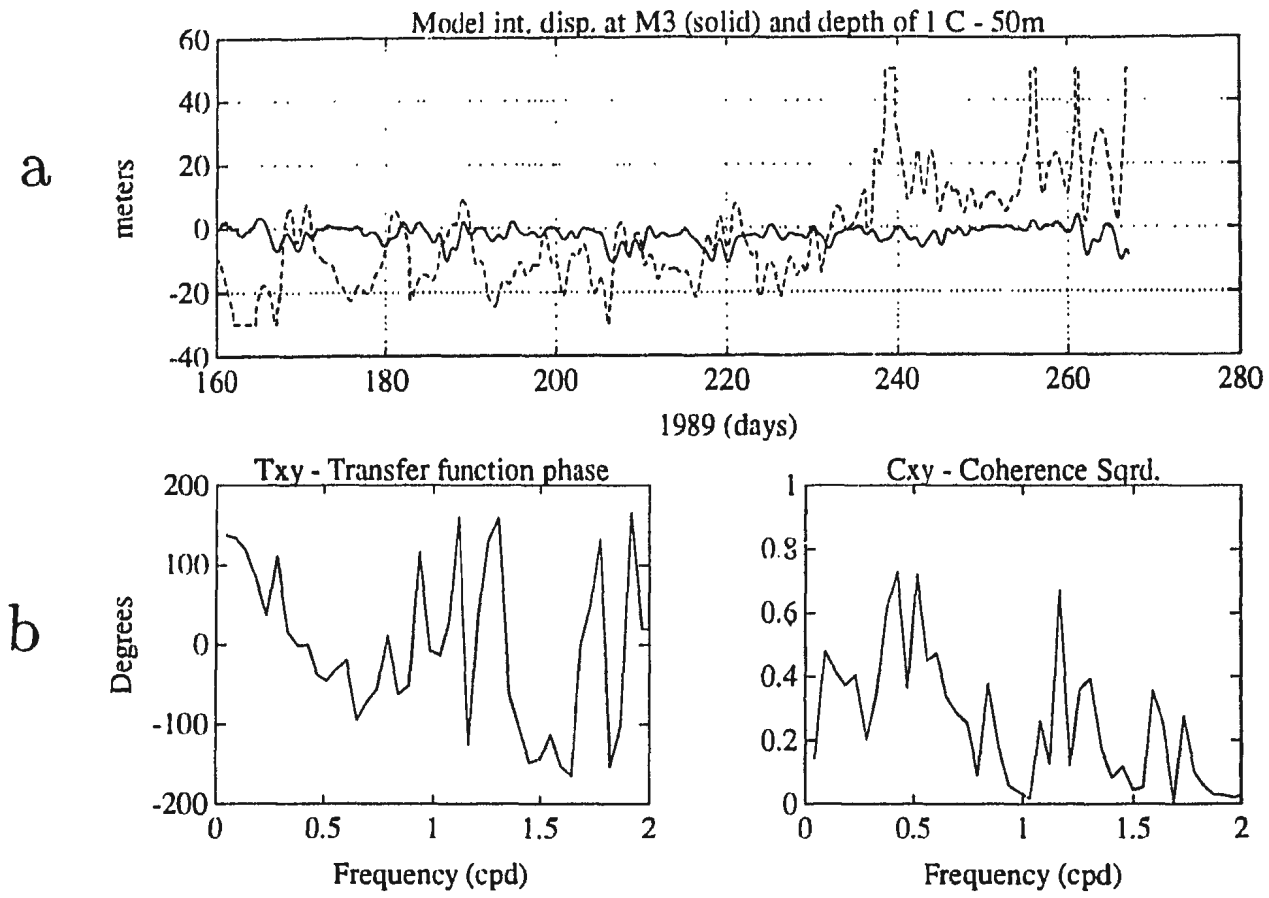

Figure 4.5 (a) Interface displacement (in meters) at M3 for the same model run in Figure 4.1 and depth of the 1°C isotherm (in meters) at M3 minus 50 meters (b) Cross-spectrum between the two time series in (a). Cross-spectrum has 10 degrees of freedom, and values of (coherence)^2 greater than 0.59 are significant at the 90% confidence level.

Temperatures at the three stations across the bay mouth from 160 to 266 days are shown in Figure 4.6. The stations are separated by roughly 5 kilometers (see Figure 2.9), a distance comparable to the Rossby radius of deformation. Agreement between temperature at M3 and M4 is good over certain periods. From 190 to 240 days, the two signals are very similar. Temperatures at M4 and M5 agree over certain periods, but not as well as M3 and M4 do. Temperature at M3 and M5 show poorer agreement than the previous two plots as expected, since the two moorings are twice as far apart. Figure 4.7 shows cross-spectra of the temperatures at the three moorings. There are ten degrees of freedom, and values of (coherence)^2 greater than 0.59 are significant at the 90% confidence level. The cross spectra reflect the statements made about the time series. Coherence is significant between temperatures at M3 and M4 at 0.1 and 0.45 cpd with phase difference less than 50°. Between M4 and M5, significant coherence is present at 0.1 and 0.45 cpd with phase difference less than 50°. Coherence between temperature at M3 and M5 is marginally significant at 0.1 and 0.45 cpd and out of phase. Therefore, it appears that temperature varies on scales of about 5 kilometers. An interesting feature is present in all three time series in Figure 4.6. At 208 days, temperature at three stations rapidly rises and then decreases over about 5 days. The similarity of the signals at all three moorings shows that this feature has a length scale of at least 10 kilometers. This event is associated with a strong southwesterly wind that would be correlated with a reduction in temperature if the Bay were behaving as a 1-1/2 layer bay. The fact that the drop in temperature is not predicted by the model (see the model interface displacement in Figures 4.1, 4.2, and 4.3), and is actually the opposite of what the model predicts, means that this rapid rise in temperature is not part of the

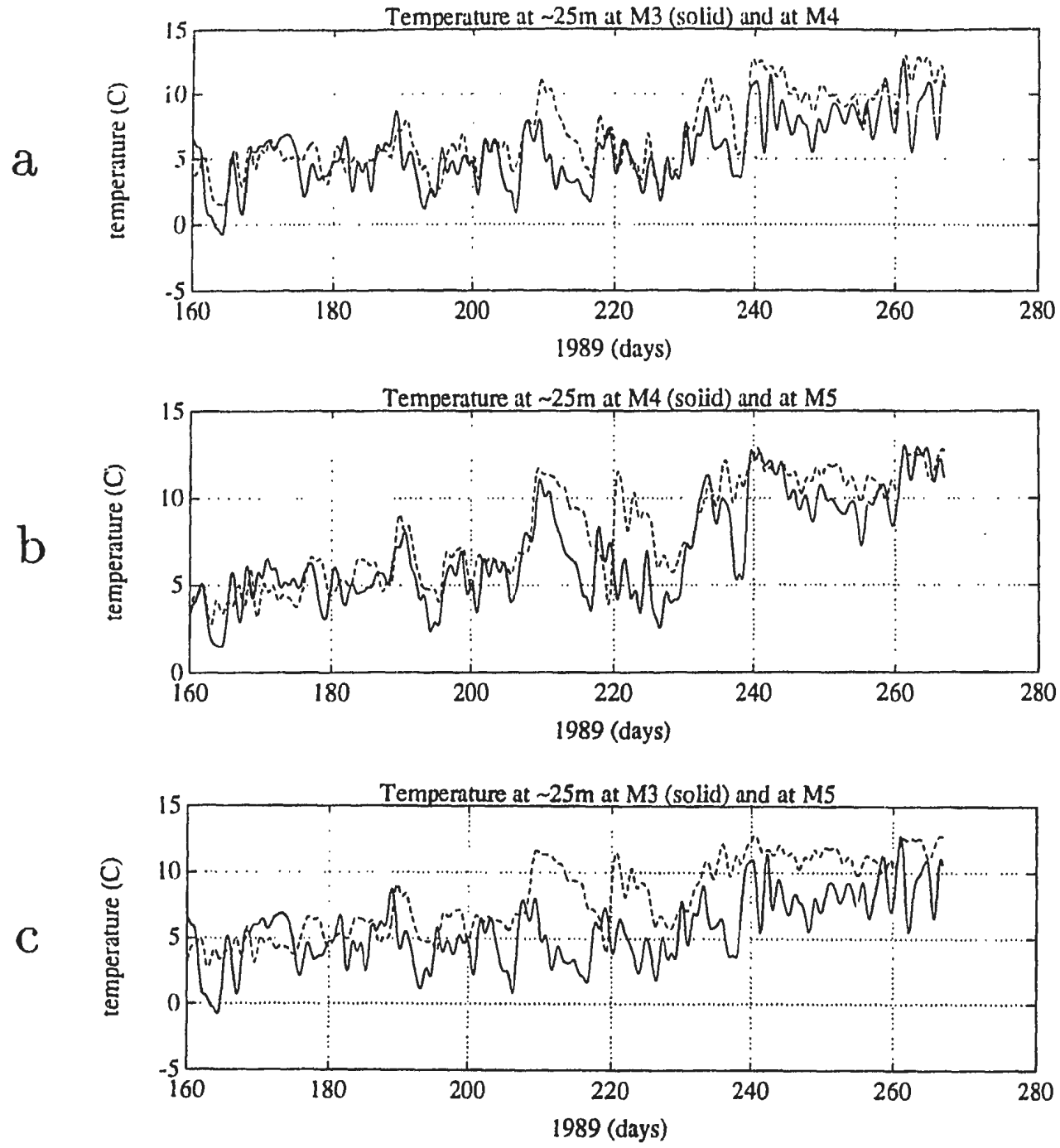

Figure 4.6 (a) Temperature (in °C) at ~25 meters at M3 (solid line) and M4 (dashed line) (b) Temperature (in °C) at ~25 meters at M4 (solid) and M5 (dashed) (c) Temperature (in °C) at ~25 meters at M3 (solid) and M5 (dashed)

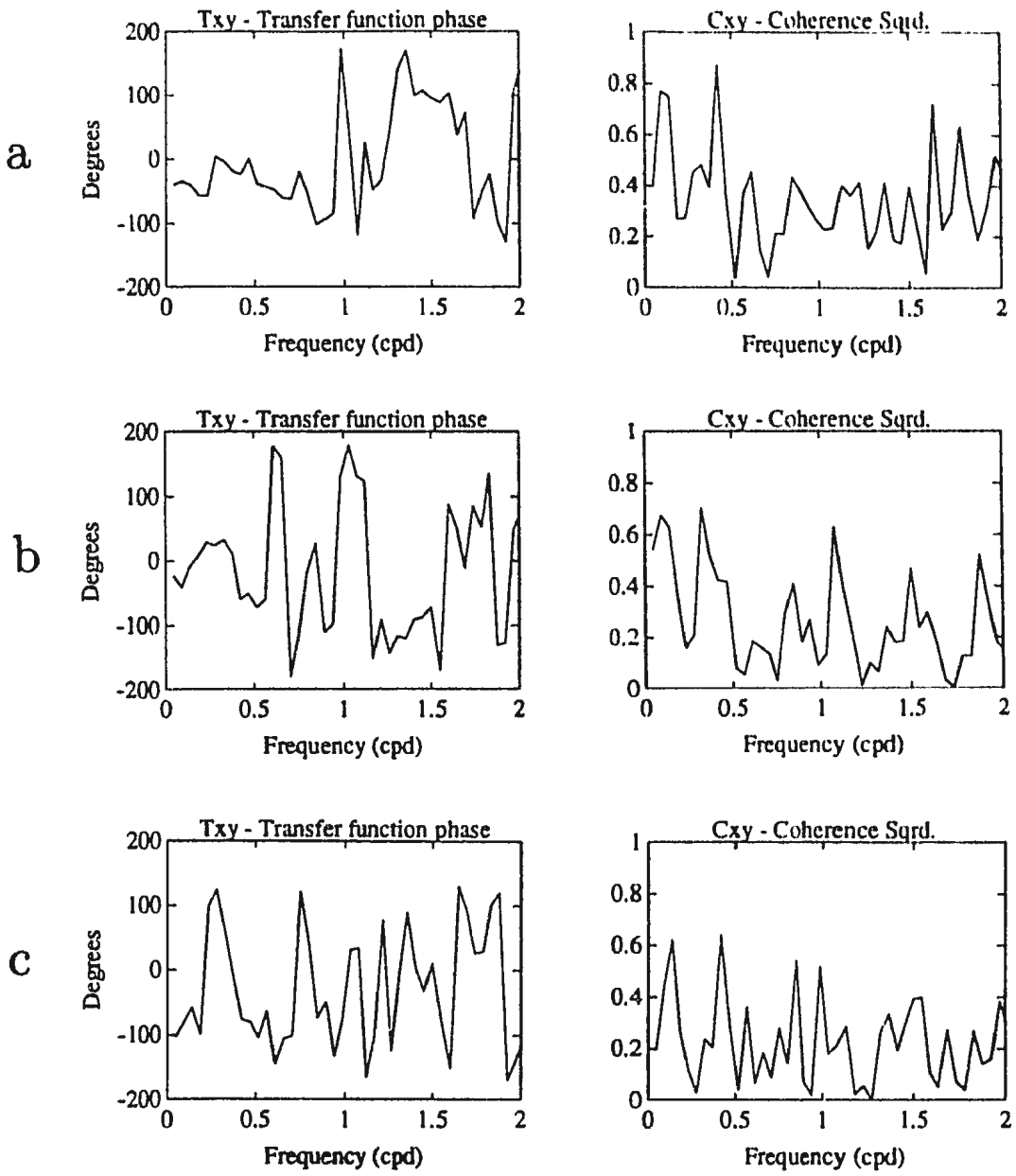

Figure 4.7 (a) Cross-spectrum between temperatures at ~25 meters at M3 and M4 from days 160 to 266 (b) Cross-spectrum between temperatures at ~25 meters at M4 and M5 from days 160 to 266 (c) Cross-spectrum between temperatures at ~25 meters at M3 and M5 from days 160 to 266. Cross-spectrum has 10 degrees of freedom, and values of (coherence)^2 greater than 0.59 are significant at the 90% confidence level.

local wind-forced response. Similar temperature variations were shown by Anderson (1986) to be related to baroclinic eddies shed from the Labrador Current.

Spectral analysis of observed and modelled currents can be used to determine the extent to which the model reproduces observed currents. Spectral analysis was performed using a rotary-spectral technique. The vectors are transformed from Cartesian coordinates into polar coordinates to remove coherence dependence on the choice of coordinate system. Spectra are then computed for like-rotating vectors (inner spectra) and for vectors rotating in opposite directions (outer spectra) (Gonella, 1972; Mooers, 1973). Significant coherence is determined in the same manner as in scalar spectral analysis.

The observed current at ~25 meters at M3 (the only surface meter successfully recovered in 1989) and the current in a model run ($g' = 9.6 \times 10^{-3} \mathrm{ms}^{-2}$, $H_1 = 40$ m, $\epsilon = \gamma =$ 1/10 days) from 170 to 303 days as well as the wind stress are plotted in Figure 4.8. (The currents and wind stress are in bay coordinates so that $+v$ points out the mouth.) The obvious difference between the two currents is that the observed current has no directional bias, while the model current is dominated by the alongshore component, v. Notice that the alongshore component of model velocity is essentially identical to the y-component of wind stress.

Rotary-spectral analysis comparing the observed and modelled currents in Figure 4.8 is shown in Figure 4.9. The lowest resolvable frequency is 0.047 cpd (a period of 21.3 days), and there are 12 degrees of freedom. Values of (coherence)^2 greater than 0.56 are significant at the 90% confidence level. For the inner spectrum, positive frequency represents counter-clockwise rotating vectors, and negative frequency represents clockwise rotating vectors.

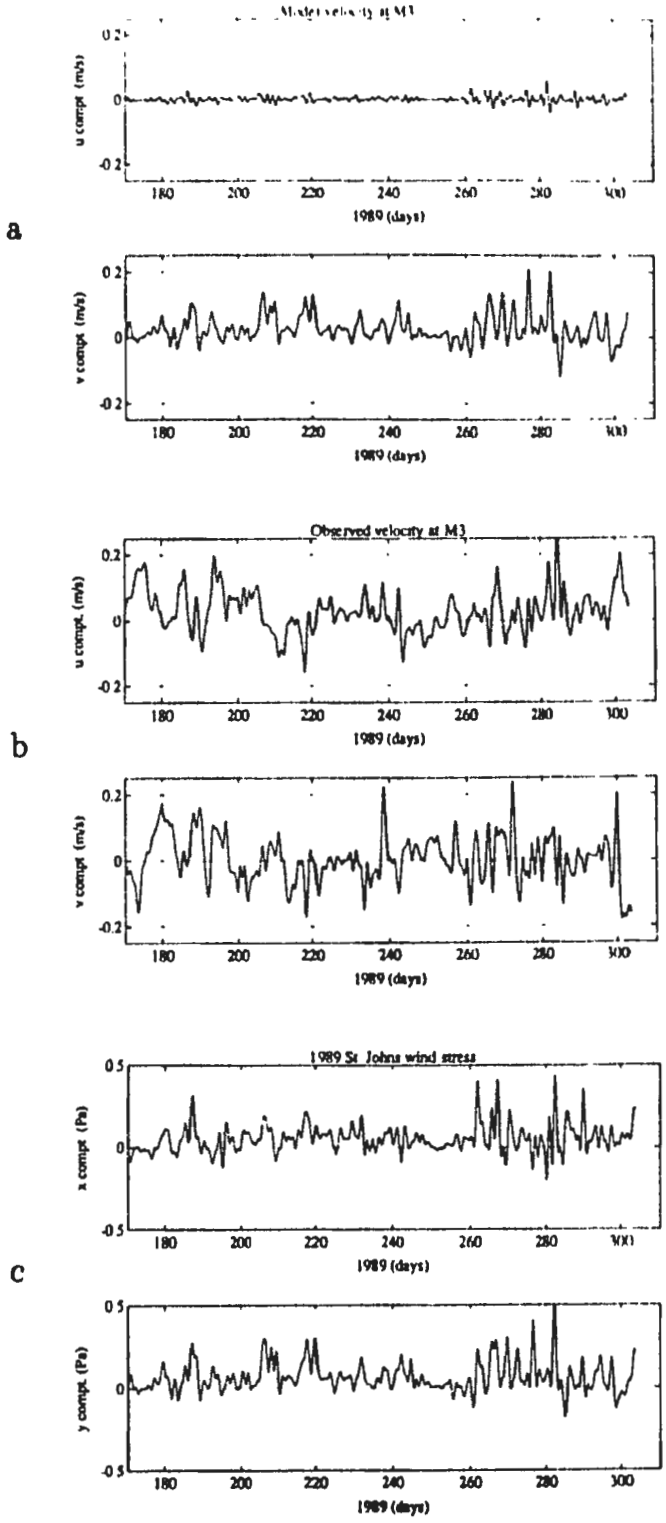

Figure 4.8 (a) Observed current (in ms^{-1}) at ~25 meters at M3 (b) Current (in ms^{-1}) at M3 for a model run from days 170 to 303. $g' = 9.6 \times 10^{-3}$ ms^{-2}, $H_1 = 40$ m, and $\epsilon = \gamma = 1/10$ days (c) Wind stress (in Pascals) for the same period

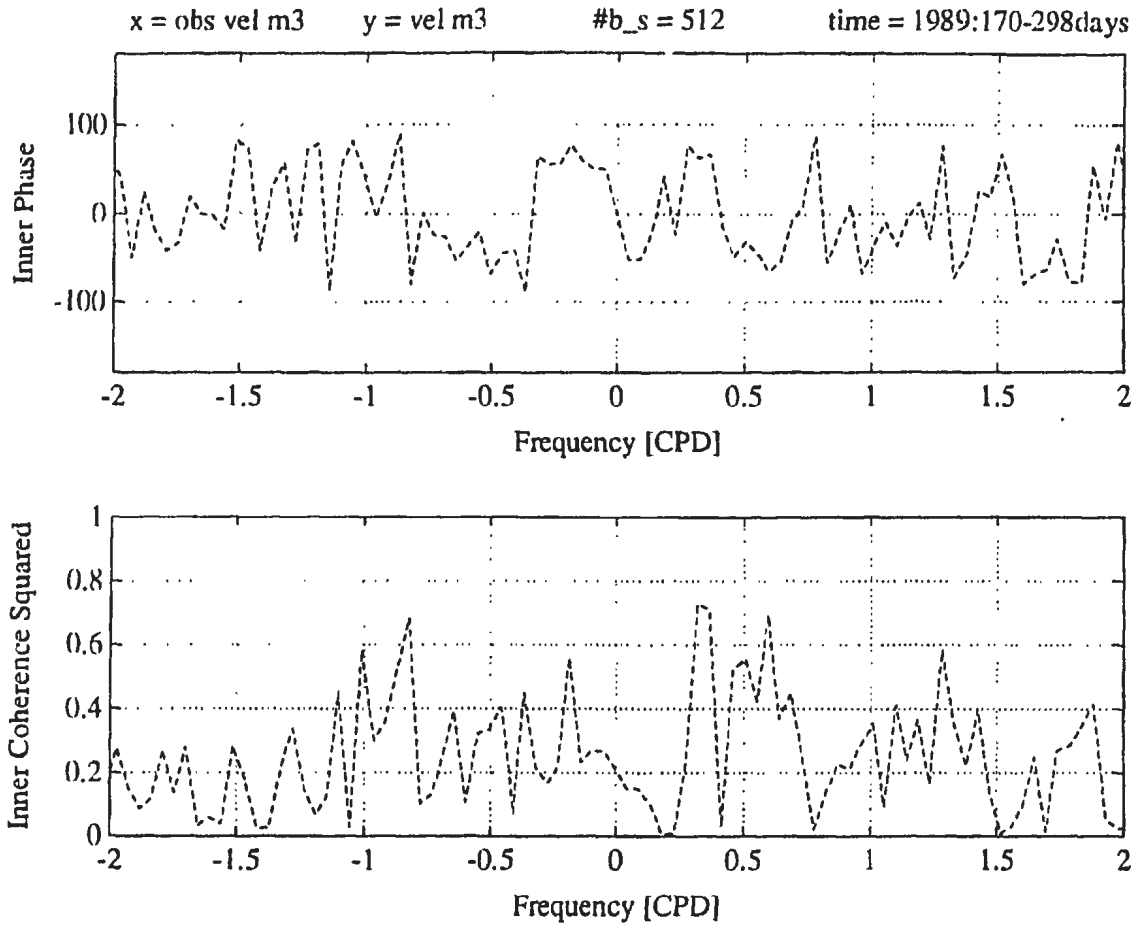

Figure 4.9 Rotary cross-spectrum between the modelled and observed current in Figure 4.8 at M3 from 170 to 298 days. Only the inner spectrum is shown. Spectrum has 12 degrees of freedom, and values of (coherence)^2 greater than 0.56 are significant at the 90% confidence level.

Since we are only interested in like rotating currents, the outer spectrum is not shown. In general, the agreement is poor. Significant coherence is present in the inner spectrum at 0.3 cpd with 80° phase offset and at 0.6 cpd with −50° phase offset. Except for those two frequencies, the coherence is not significant. Therefore, the model does not reproduce the observed current at the mouth well.

Rotary-spectral analysis of the wind versus the current can be used to further investigate whether the current at M3 is forced by the wind. The rotary cross-spectrum between the wind and the observed current at M3 from 170 to 298 days shown in Figure 4.10 reveals marginal agreement at around 2 days. Coherence is not significant. For comparison, the rotary-spectrum between the wind and model current at M3 reveals significant coherence (coherence squared varies from 0.5 to 0.8) for frequencies between 0.35 and -0.5 cpd (spectrum is not shown). This direct comparison of wind stress and observed current substantiates the conclusion that the wind stress is not strongly correlated to the current at ~25 meters depth at the mouth.

In general, the observations (i.e. temperature and velocity) at the mouth do not agree well with the 1-1/2 layer model; however, the 2 day period temperature signal appears to be wind-forced. Comparison of temperature at neighboring stations across the mouth show that the horizontal scale of temperature is ~5 to 10 km and indicate the presence of baroclinic eddies. Analysis of the current at ~25 m at M3 shows weak coherence with the model current.

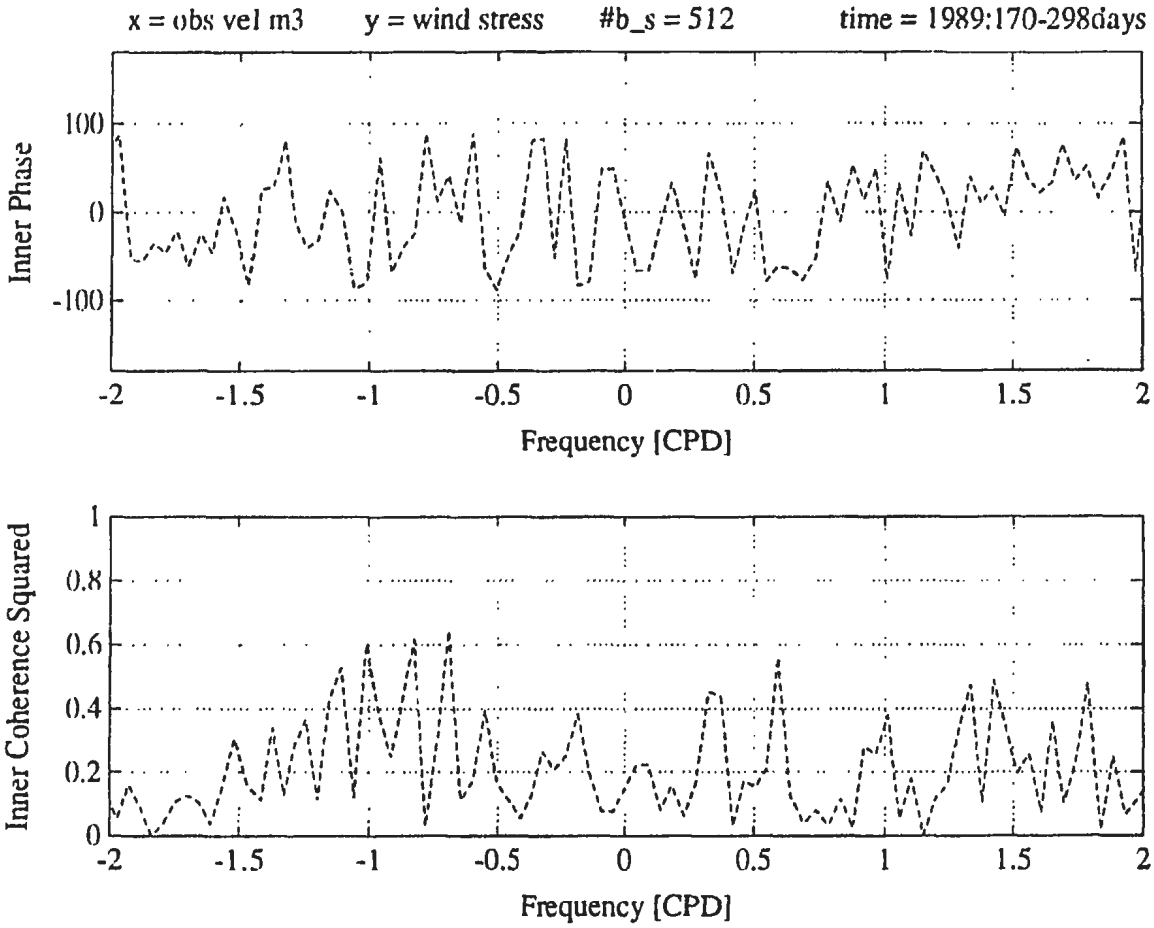

Figure 4.10 Inner spectrum between the wind stress and observed current from 170 to 298 days. Spectrum has 12 degrees of freedom, and values of (coherence)^2 greater than 0.56 are significant at the 90% confidence level.

4.4: Analysis near the Head of the Bay for 1990

The 1990 data collected near the head of the Bay are expected to have different characteristics from the 1989 data collected across the mouth. The effect of outside influences, such as Kelvin waves generated in Trinity Bay and eddies shed from the inshore branch of the Labrador Current, are expected to be reduced near the head, as a result of dissipation or scattering by bottom topography, in comparison to the mouth. The dominant effect near the head may be from the local upwelling, because the upwelling amplitude due to winds from the southwest will be larger at the head since the amplitude increases linearly toward the head, as can be seen in Figure 3.12 for a steady wind and as described by equation (3.9).

As shown in Chapter 2, the temperature signals at the six moorings in 1990 have remarkable similarity that implies an upwelling response to wind forcing. Figure 4.11 shows the temperature measured at the six current meters at ~25 m depth at moorings 1 through 6 and the wind stress from day 170 to 205. The wind stress is predominantly positive in both the x and y directions indicating an east-northeastward wind. As demonstrated in Chapter 3, a steady wind blowing out the bay will generate an upwelled Kelvin wave on the western side that will propagate the upwelling signal around the head of the bay (see Figure 3.12a). Therefore, long-period northeastward winds, like the one from day 175 to 180, are expected to cause upwelling around the head in Conception Bay. The rapid decrease in temperature at moorings 1 through 4 at the onset of the wind at day 175 is evidence of an upwelling event. Once the wind stress has relaxed, the temperature returns to its pre-upwelling value

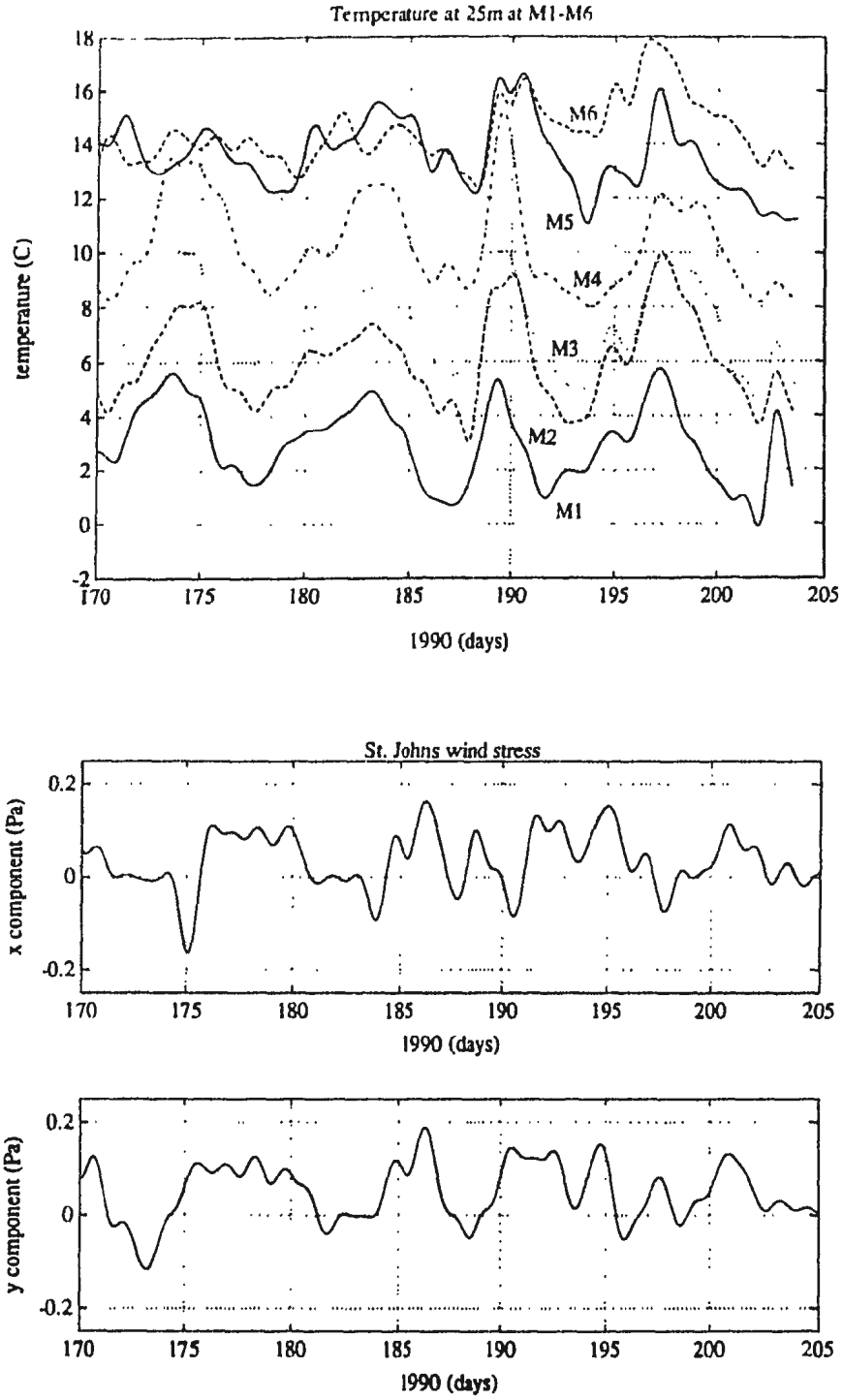

Figure 4.11 Temperatures (in °C) at ~25 m at the 6 current meters for 1990 and wind stress (in Pa). For easier comparison, 2°C has been added to the temperature at M2, 4°C added to the temperature at M3, and so on.

indicating that the upwelling signal has propagated out of the bay as a Kelvin wave. This upwelling and relaxation is initiated again at days 183, 190, and 197 as seen in Figure 4.11.

The pycnocline/thermocline motion at the head of the Bay can also be measured by tracking a particular isotherm as was done for the 1989 data across the mouth. Figure 4.12 shows the depth of the 1°C isotherm at the four moorings where the thermistor chains were successfully recovered. For comparison, a plot of temperature at the six moorings for the entire period of data acquisition is shown in Figure 2.20. Figures 4.11 and 4.12 show essentially the same events except that Figure 4.12 resolves thermocline movement better in the spring when the water column is weakly stratified (see Figures 2.16, 2.17, and 2.18 for vertical temperature profiles). Figure 4.13 shows the temperature at ~25 meters at M4, the 1°C isotherm position at M4, and the wind stress. Any mooring could be used since they are all similar. The similarity of signal at the moorings at the head of the Bay can be seen by comparing temperature at ~25 m at moorings 1, 3, and 5 in Figure 4.11, for example. Even though the moorings are separated by ~15 km, the signal at all three moorings is quite similar. Before day 135 in Figure 4.13, the 1°C isotherm is above the top of the thermistor chain. At day 135, a negative wind stress in the y-direction appears to cause downwelling of the pycnocline. The wind reverses at day 145 causing upwelling. At this time of year, the reduced gravity is small resulting in large pycnocline movements. Throughout the time series in Figure 4.13b, the amplitude of the isotherm movement decreases. A likely reason for this is that the reduced gravity is increasing throughout the year, as stratification develops, and thus reducing the amplitude of the vertical motion of the pycnocline. At early times, the temperature change at a particular depth during an upwelling event is small, because

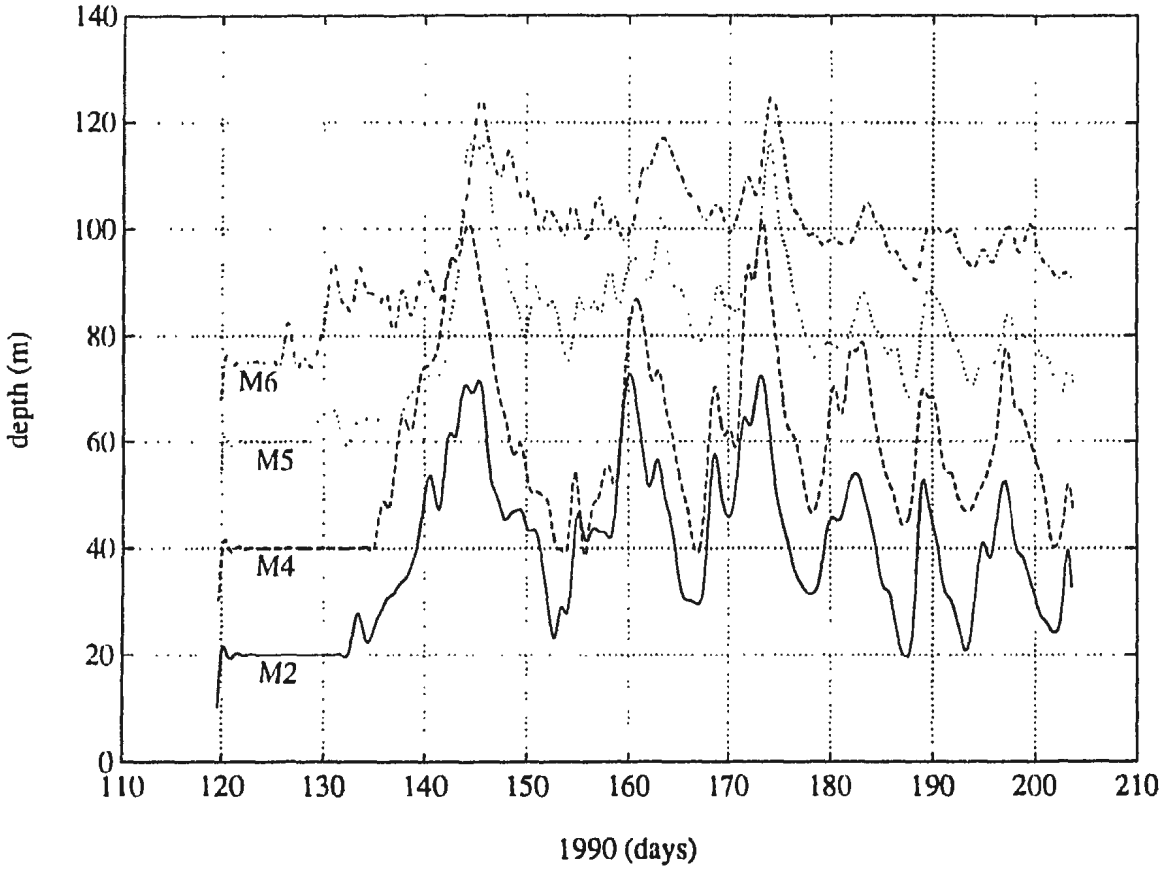

Figure 4.12 Depth of the 1°C isotherm (in meters) at moorings M2, M4, M5, and M6. For easier comparison, 20 m has been added to the isotherm depth at M4, 40 m has been added to the isotherm depth at M5, and 60 m has been added to the isotherm depth at M6.

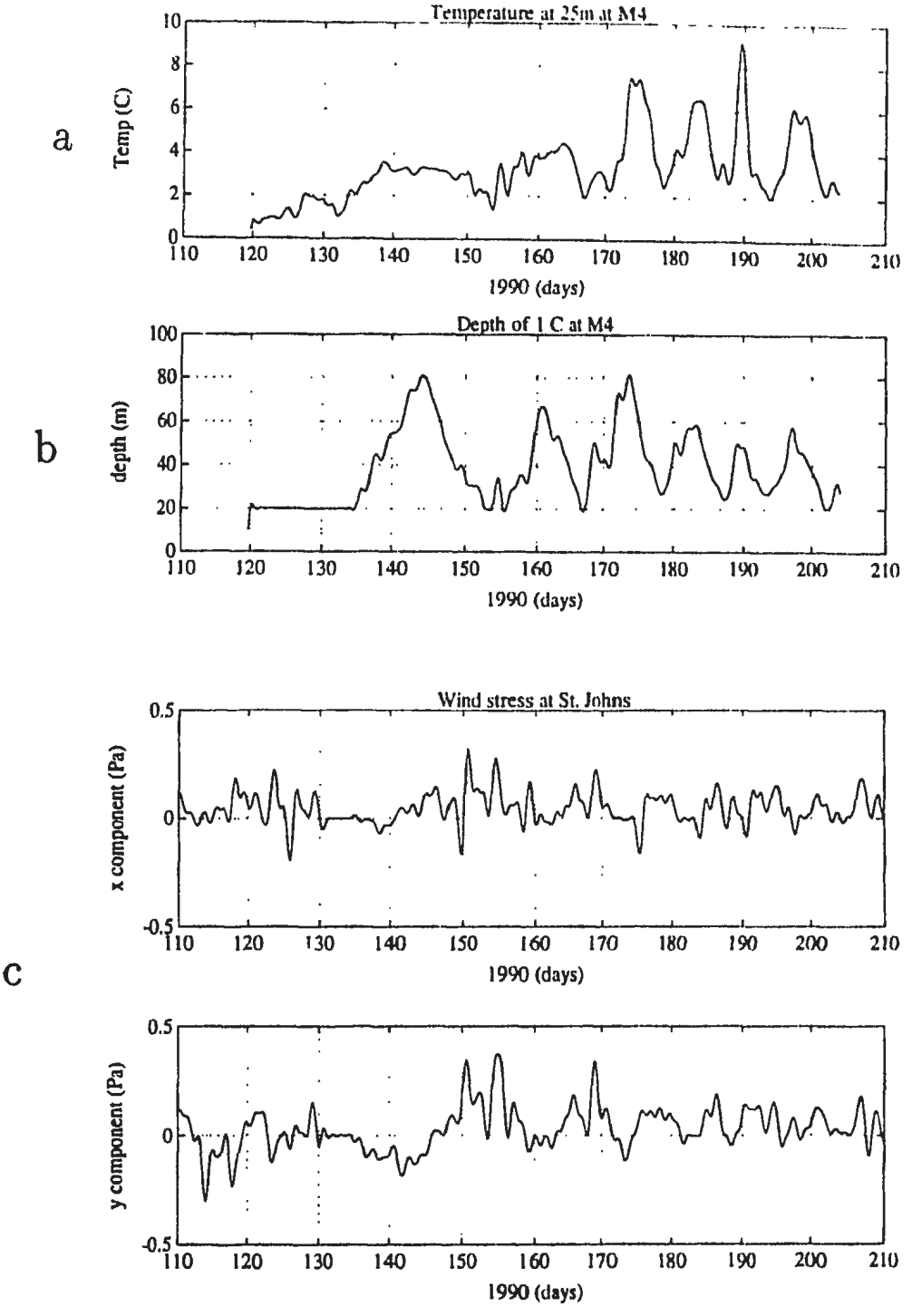

Figure 4.13 (a) Temperature (in °C) at ~25 m at M4 (b) Depth of the 1°C isotherm (in meters) at M4 (c) St. John's wind stress (in Pa)

the water column is weakly stratified. The amplitude of temperature variation in Figure 4.13a increases with time as the temperature gradient increases. In the time series in Figures 4.13a and 4.13b, the upwelling and downwelling events correlate to the wind stress. The first noticeable event is the downwelling event at day 135 due to negative τ^y. As the y-component of wind stress relaxes to zero and becomes positive, the downwelling signal leaves the Bay and upwelling occurs at the head. Upwelling events related to the onset of positive τ^y are observed at days 162, 173, 183, 190, and to a lesser extent day 197.

The spectral analysis used to compare the observed 1989 temperature data with modelled data can also be applied to the 1990 data. The period 170-203 days is used to evaluate the data because the upwelling events are strongest and the reliabilty of the temperature at M1 from day 160 to 168 is questionable. Unfortunately, the briefness of the usable time period (approximately 30 days) places constraints on the lowest frequency resolvable by spectral analysis. As discussed previously, the time series must be divided into five sections to attain reliable spectra. Thus the longest period signal that could be resolved would be 6 days, which is shorter than the roughly 8 day period cycle apparent in Figures 4.11-4.13.

Several numerical integrations were performed for the period 150-203 days using a friction of $\epsilon = \gamma = 1/10$ days. The model runs use a common upper layer depth of 40 meters and values for g' of 4.8, 7.2 and 9.6 $\times 10^{-3}$ ms^{-2} which give Rossby radii of 4.4, 5.4, and 6.2 km. (Note that c is the important parameter when η is the prime concern, and that, since only the magnitude of velocity is changed by varying H_1 while keeping c constant, varying H_1 will not affect spectral analysis of the velocity.) Figure 4.14 shows that doubling g' has little affect except to change the amplitude η. The plot shows that,

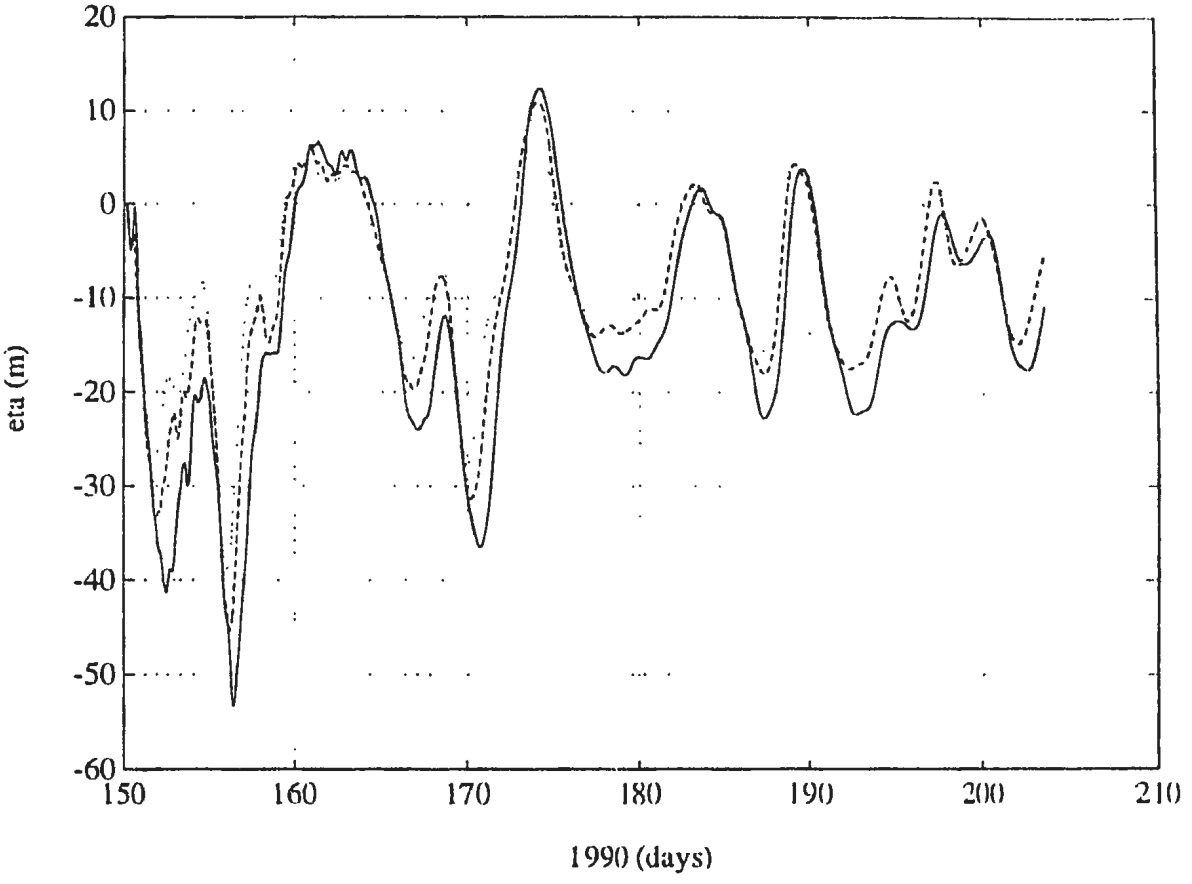

Figure 4.14 Model interface displacement (in meters) at M1 for three sample runs using different values of g'. H_1 is fixed at 40 meters while g' is 1.8×10^{-3} ms^{-2} in the solid-line case, 7.2×10^{-3} ms^{-2} in the dashed-line case, and 9.6×10^{-3} ms^{-2} in the dotted-line case.

although the effect of increasing c is noticeable in changing the phase of the signal by a day or so, the wind is the primary factor in determining the nature of the solution.

To determine which value of c applied to the model best reproduces the temperature variability, lagged correlations between observed temperatures and model interface displacements for the three values of c were calculated at the six mooring positions. Figure 4.15 shows the model interface displacement at M1 for part of the model run using $g' = 7.2\times10^{-3}$ ms^{-2}, $H_1 = 10$ m, and $\epsilon = \gamma = 1/10$ days, and the corresponding observed temperature at $\sim$25 meters. The correlation between temperature and interface displacement is computed by removing the mean from the two time series and summing the product for different offsets in time as given by the following equation

$$R(\tau) = \int_{t_1}^{t_2} x_1(t)x_2(t+\tau)dt \qquad (4.1)$$

R is calculated from day 171.67 to 201.33 for τ ranging from -40 to +40 hours, where x_1 is temperature and x_2 is η. If x_1 leads x_2, the maximum $R(\tau)$ will occur at $\tau > 0$. If x_2 leads x_1, the maximum $R(\tau)$ will occur at $\tau < 0$. The value of c used in the model that gives the largest maximum value of R is the one that best fits the data.

The correlations were calculated for g'= 4.8, 7.2 and 9.6 $\times10^{-3}$ ms^{-2} while keeping H_1 fixed at 40 meters. The case with $g' = 7.2 \times 10^{-3}$ ms^{-2}, and thus $c = 0.53$ ms^{-1}, gives the best overall agreement between model and observed temperature for all six moorings. Maximum values of R occurred within 5 hours of zero lag at all six moorings. For the other cases, the correlations show that η led temperature for values of c greater than 0.53 ms^{-1} and that temperature led η for c less than 0.53 ms^{-1} as expected.

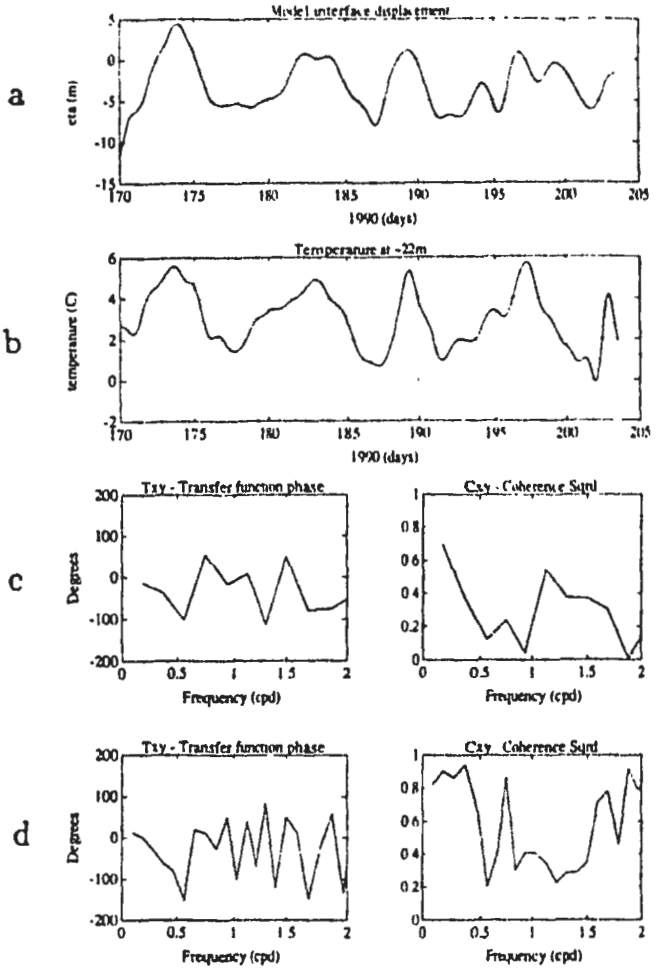

Figure 4.15 (a) Interface displacement (in meters) at M1 for part of the run from 150 to 203 days. Model parameters are $g' = 7.2 \times 10^{-3}$ ms^{-2}, $H_1 = 40$ m, and $\epsilon = \gamma = 1/10$ days. (b) Observed temperature (in °C) at ~25 meters at M1. (c) Cross-spectrum between model interface displacement and temperature from 170 to 202 days. Spectrum has 12 degrees of freedom, and values of (coherence)^2 greater than 0.56 are significant at the 90% confidence level. (d) Cross-spectrum between model interface displacement and temperature using 6 degrees of freedom such that values of (coherence)^2 greater than 0.68 are significant at the 90% confidence level.

The model has considerable success in reproducing the long period upwelling events at the head of the Bay (see Figure 4.15). The model interface displacement and temperature are strongly correlated between 170-192 days. (Note that model output for 1990 is stored every half hour to coincide with the temperature and current sampling frequencies.) At day 173 (corresponding to the peak in temperature), the temperature shows an upwelling event that is related to a lifting of the model interface. At day 180, the temperature relaxes back to near its pre-upwelling value as the model interface returns to its undisturbed state. The upwelling cycle is repeated again at days 183 and 190. At day 197, the temperature signal shows an upwelling event that the model reproduces to some extent but not as well as the previous events. Figure 4.15 also shows the cross-spectrum for the two time series from day 170 to 202. In Figure 4.15c, the time series are divided into six bins of 256 points so that the longest resolvable period is 5.3 days and significant (coherence)^2 is 0.56 at the 90% confidence level. The figure shows significant coherence and phase agreement at frequencies less than 0.25 cpd. Unfortunately the low-frequency signal (i.e. periods > 5.3 days) cannot be resolved, but it is obvious from the time series that the longer period signal of the model and temperature agree quite well. The cross-spectrum for the same two time series is plotted in Figure 4.15d using 3 bins of 512 points. This allows periods of 10.6 days to be resolved while reducing the reliabilty of the spectrum. (Coherence)^2 greater than 0.68 is significant at the 90% confidence level. The figure shows that coherence is high (> 0.8) and the phase difference less than 50° at frequencies less than 0.3 cpd.

Interface displacement for the same model run and temperature at moorings 2, 3, and 4 are shown in Figure 4.16. As at M1, the model reproduces the long-period signal well

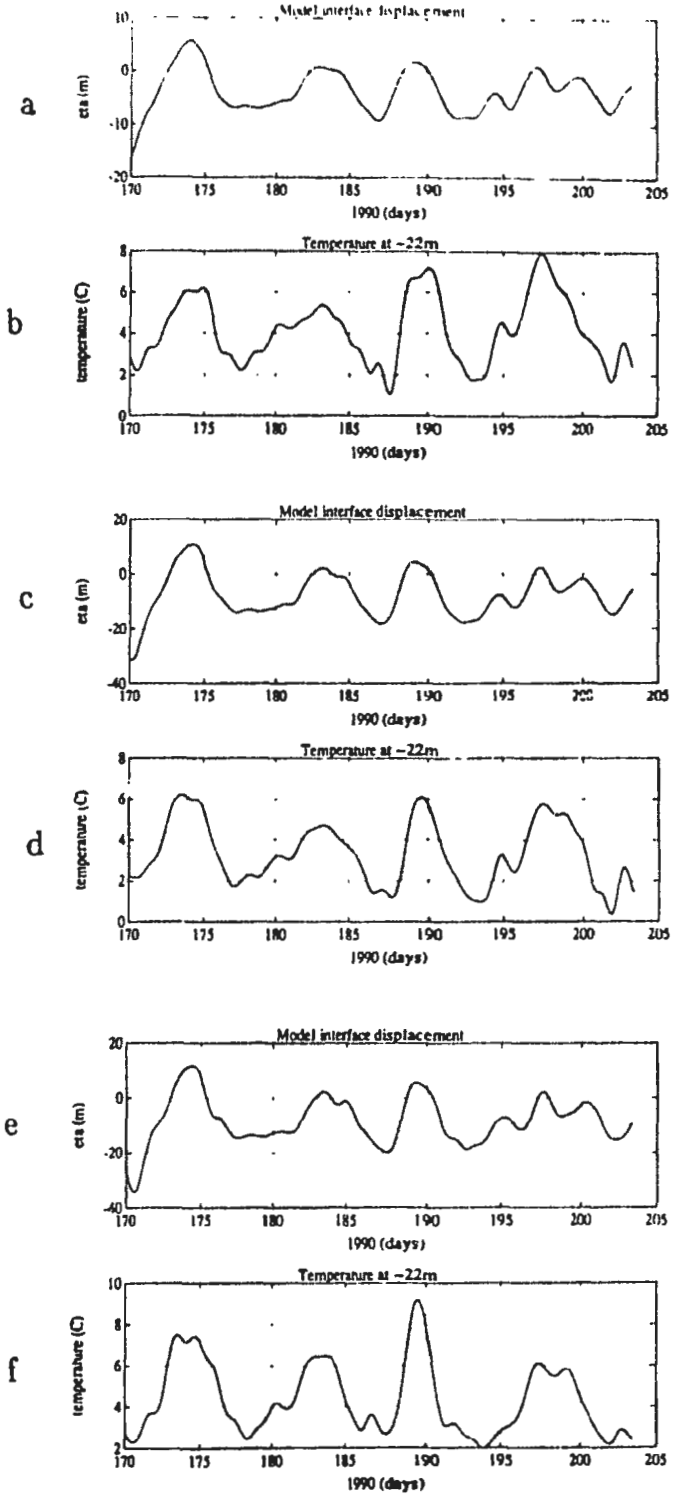

Figure 4.16 (a) Interface displacement (in meters) at M2 for the same model run as in Figure 4.15 (b) Temperature (in °C) at ~25 meters at M2 (c) Interface displacement (in meters) at M3 (d) Temperature (in °C) at ~25 meters at M3 (e) Interface displacement (in meters) at M4 (f) Temperature (in °C) at ~25 meters at M4

at all three moorings. The upwelling events in the temperature signal starting at 175, 183 and 190 are clearly apparent in the interface displacement, while the event starting at day 197 is to a lesser extent. Moorings 1, 2, 3, and 4 are located in deeper water (~150 meters) meaning that the wind-forced response should be less affected by topographic scattering. Cross-spectra between temperature and interface displacement at the three moorings are essentially the same as in Figure 4.15 and are not shown.

Moorings 5 and 6 are located "downstream" (in the sense of Kelvin wave propagation) of the shallow region between Bell Island and the shoreline (see Figure 1.2 for bottom topography of Conception Bay). Internal Kelvin waves propagating around the head of Conception Bay are expected to be corrupted to some extent by the topography when they reach Bell Island Tickle. Figures 4.11 and 4.12 can be used to determine the extent to which Kelvin waves are distorted by the topography. If topography is important, the signals in Figures 4.11 and 4.12 should be altered as the Kelvin wave propagates around the head with the largest distortion occurring at the shallow region between M4 and M5. In Figure 4.12, the upwelling events present at M2 and M4 are also seen at M5 and M6. The magnitude of the thermocline movement is smaller at M5 and M6 possibly due to their position farther from the shoreline. The general upwelling signal is present at all moorings indicating that topographic effects are not, in general, strong. In Figure 4.11, which shows temperature rather than isotherm displacement, the upwelling events are clearly seen at M5 and M6 after day 180. Before day 170, the lack of vertical stratification makes comparison of temperature difficult. The one event at day 173 is not seen as clearly at M5 and M6 in Figure 4.11, but this is probably due to a lack of temperature stratification.

One difference between the observed temperature at moorings 5 and 6 and the other four moorings at the head is the presence of an oscillation with roughly 2 day period at moorings 5 and 6. The oscillation could be a trapped Kelvin wave that propagates around Bell Island. In the shallow region of Bell Island Tickle, the wave speed of the first mode is reduced to ~ 0.25 ms^{-1}. The circumference of Bell Island is ~ 25 km; however, Kelvin waves propagating around an island will travel a distance a Rossby radius or two larger than the actual circumference. For an effective circumference of 35 km and a wave speed of 0.25 ms^{-1}, the period of a trapped wave is 1.6 days. Thus, trapped Kelvin waves could be the source of the 2 day period signal detected at moorings 5 and 6.

Interface displacement and temperature at M5 and M6 are shown in Figure 4.17. The model successfully reproduces the temperature signal from 185 to 195 days. Before day 185, the model and temperature have the same trends, but the temperature signal is small due to weak stratification. After day 195, the model reproduces the general trend of relaxation and upwelling, but is no more successful at reproducing the abruptness of the upwelling than it was at moorings 1-4.

In Figure 4.18, plots of the 1°C isotherm depth and the model interface displacement for the entire run from 150 to 203 days are shown at the four moorings where the thermistor chains were successfully recovered. All major upwelling events are captured by the model with M4 having the best agreement in both shape and amplitude.

The speed of an internal Kelvin wave was estimated to be 0.53 ms^{-1}, previously, by correlating temperature with model output. The phase speed can also be estimated from lagged correlations between temperatures at different moorings (see Figure 4.11). Since

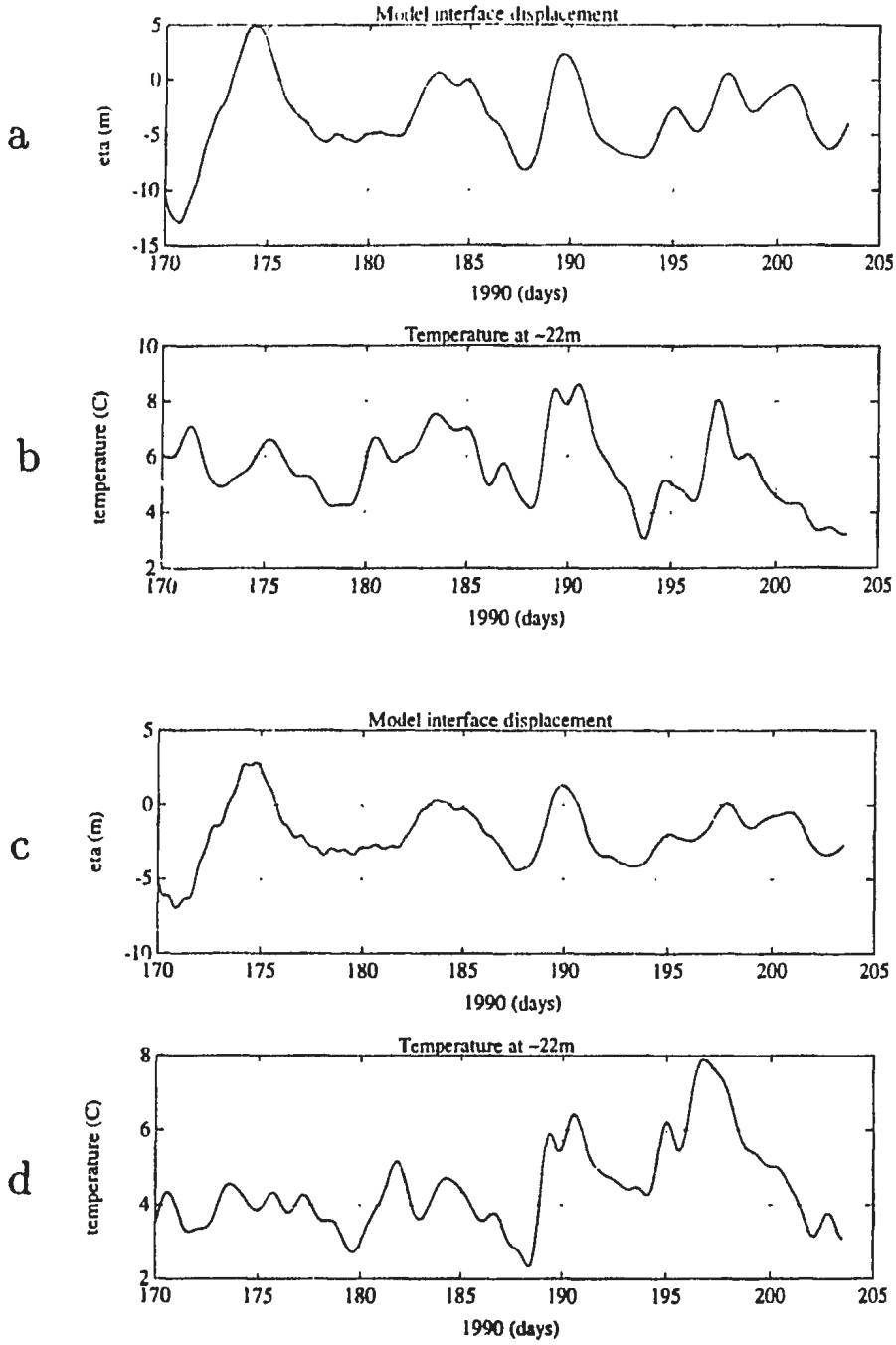

Figure 4.17 (a) Interface displacement (in meters) at M5 for the same model run as in Figure 4.15 (b) Temperature (in °C) at ~25 meters at M5 (c) Interface displacement (in meters) at M6 (d) Temperature (in °C) at ~25 meters at M6

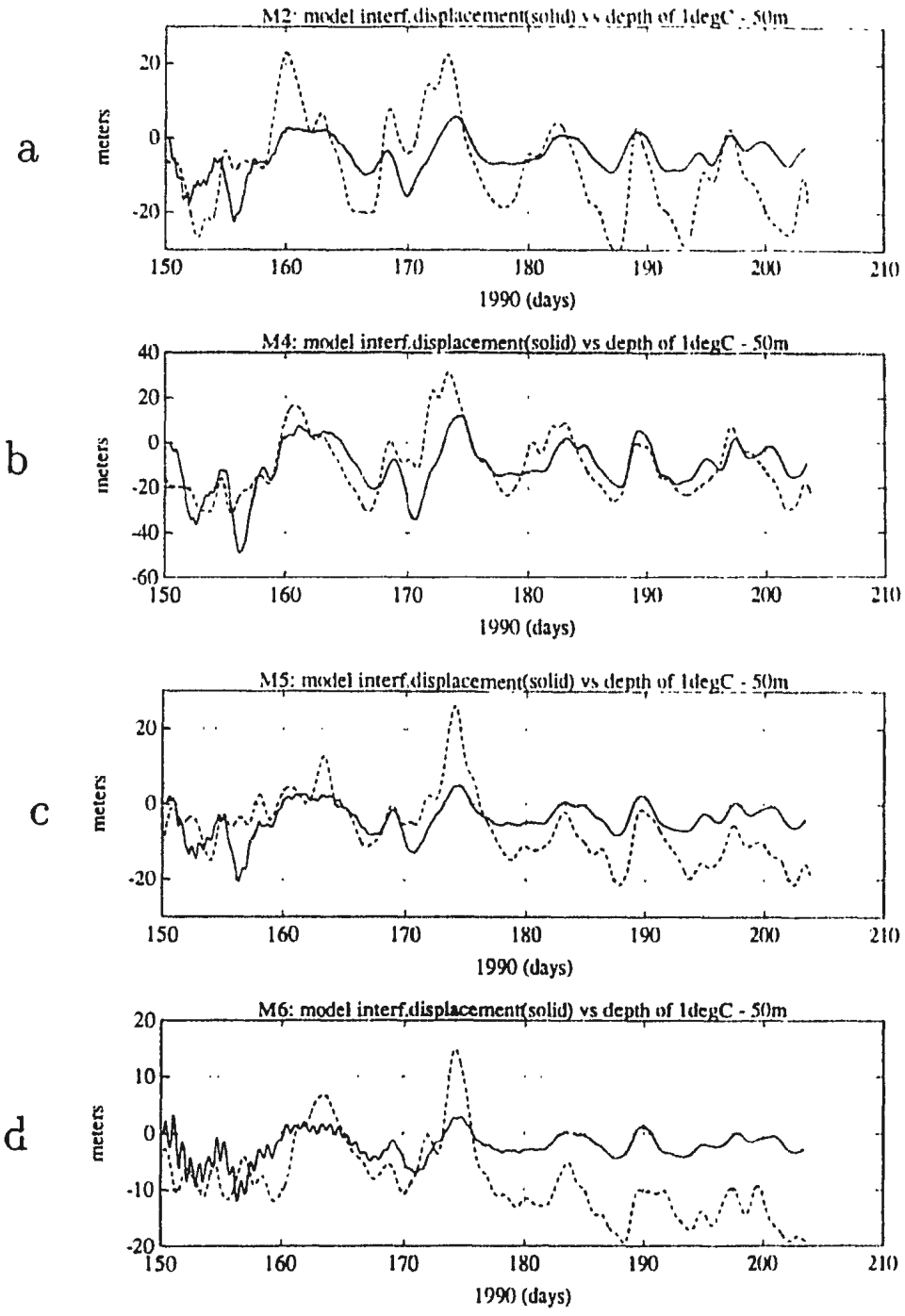

Figure 4.18 Interface displacement (in meters) for the same model run as in Figure 4.15 and depth of the 1°C isotherm (in meters) at (a) M2, (b) M4, (c) M5, and (d) M6.

the distance between moorings is known, the speed of propagation can be calculated from the time lag at maximum correlation between two moorings. Correlations between the six stations show that the thermocline/pycnocline motion is propagating in the same direction as Kelvin waves, but the values of c vary from 0.23 to 1.07 ms^{-1}. c equals 0.23 ms^{-1} between M1 and M2, 0.93 between M2 and M3, 1.07 between M3 and M4, 0.35 between M4 and M5, and 0.93 between M5 and M6. Error bars on the individual estimates are probably large, hence we shall only consider the mean of these values. The average of the 5 values is 0.7 ms^{-1}, which is a reasonable value for the observed stratification and close to that calculated using correlations with varying c in the model.

The analysis of the 1990 data shows that the pycnocline movement at the head of the Bay is controlled by wind forcing. Analysis of the 1989 data showed that neither the temperature nor the velocity field at the mouth were strongly related to the wind stress, except at the 2 day period for the temperature at M3. Comparison of modelled and observed velocities at the head can be performed to assess the ability of the model to reproduce observed currents. In addition, velocities of neighboring stations can be used to estimate the horizontal scale of the velocity field at the head and to determine signal propagation in the velocity field.

To establish how well the model reproduces measured data, observed velocities at ~25 meters will be compared with modelled velocities from the same model run used to evaluate the pycnocline response (i.e. H_1 = 40 meters, $g' = 7.2 \times 10^{-3}$ ms^{-2}, $\epsilon = \gamma = 1/10$ days, and the model is run from 150 to 203 days). Figures 4.19 and 4.20 show the observed and modelled currents at moorings 2 and 3 for the period of strongest upwelling, 170-203 days.

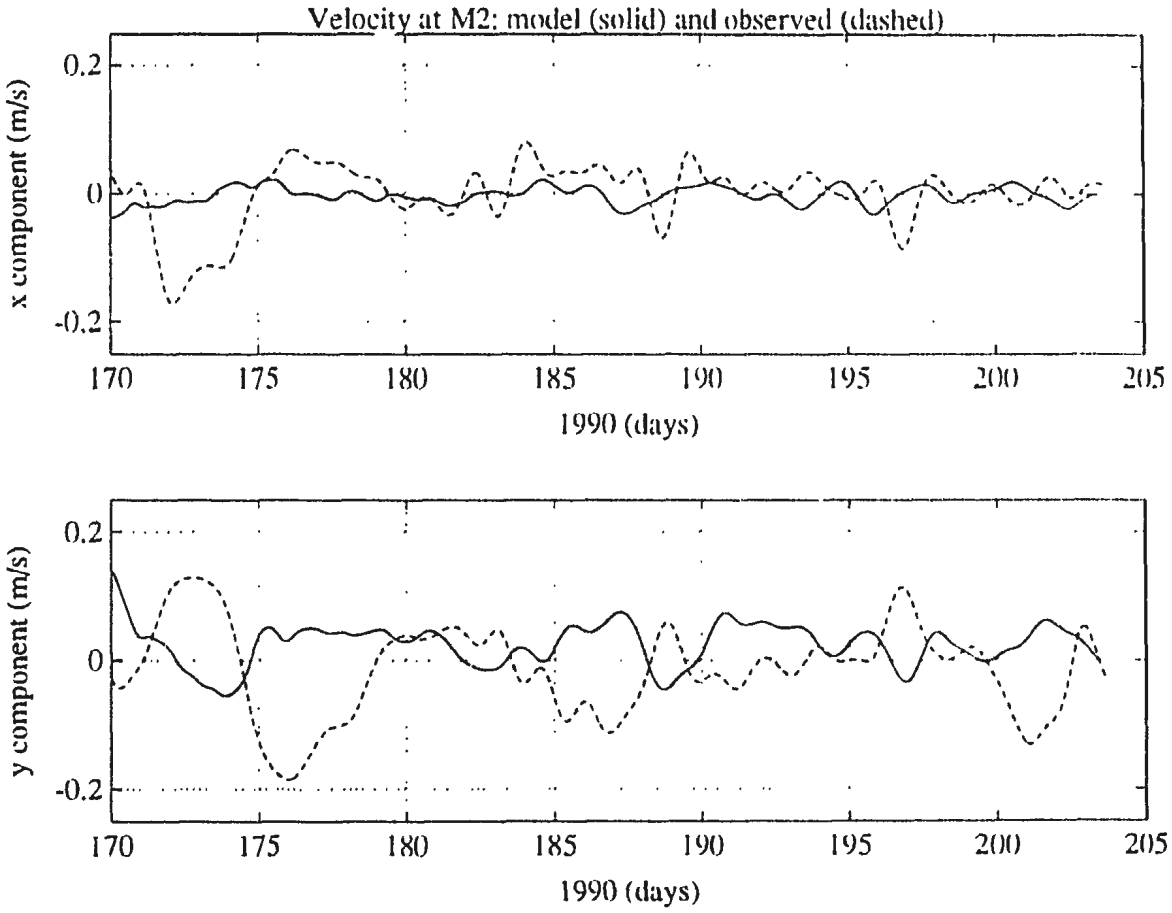

Figure 4.19 Observed (dashed lines) and modelled (solid lines) currents (in ms^{-1}) at M2.

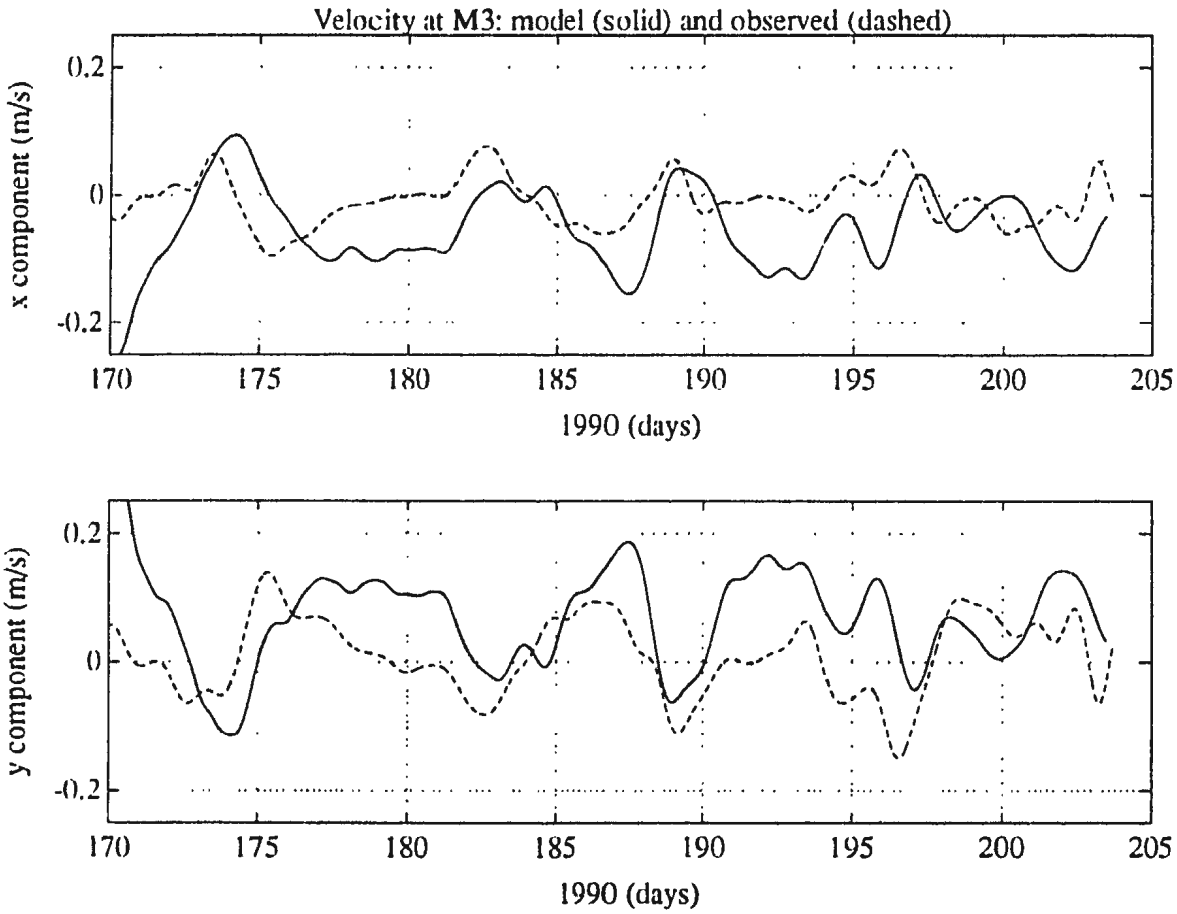

Figure 4.20 Observed (dashed lines) and modelled (solid lines) currents (in ms^{-1}) at M3.

The agreement between the observed and modelled current is obviously not as good as the agreement between temperature and model interface displacement; however, certain periods show reasonable agreement, especially at M3.

Rotary cross-spectra between the observed and modelled currents at moorings 2 and 3 are given in Figure 4.21. Spectra are computed for the period 170 to 203 days using 6 bins of 256 points each so that the longest resolvable period is 5.3 days. Significant (coherence)^2 is 0.56 at the 90% confidence level. Figure 4.21 can be compared with the rotary spectra computed for the 1989 velocity at the mouth (see Figure 4.9). (Note that Figure 4.9 has finer resolution in the frequency domain than the 1990 data due to the longer time series.) Cross-spectra between modelled and observed currents at moorings 2 and 3 have the highest coherence of the 6 moorings. Marginally significant coherence is seen (not reproduced here) between observed and modelled currents from -0.2 to -0.5 cpd at M1, from 0.2 to 0.4 cpd at M4, and no significant coherence is seen at M5 and M6. At mooring 3, agreement is highest from 0 to -0.75 cpd where coherence is significant and the phase difference is zero. For M2, coherence is significant from 0.5 to -0.5 cpd with a phase difference less than 50°. Agreement for these two moorings is certainly better than for the 1989 mooring at the mouth.

As with the scalar cross-spectral analysis of the 1990 temperature data, the rotary cross-spectra are unable to resolve periods greater 5.3 days and thus miss a significant part of the response (see Figure 4.20). To better analyze the wind-forced response of the current, the observed and modelled currents can be rotated into their principal components so that the alongshore components, which are nearly the pressure-driven parts, can be

a

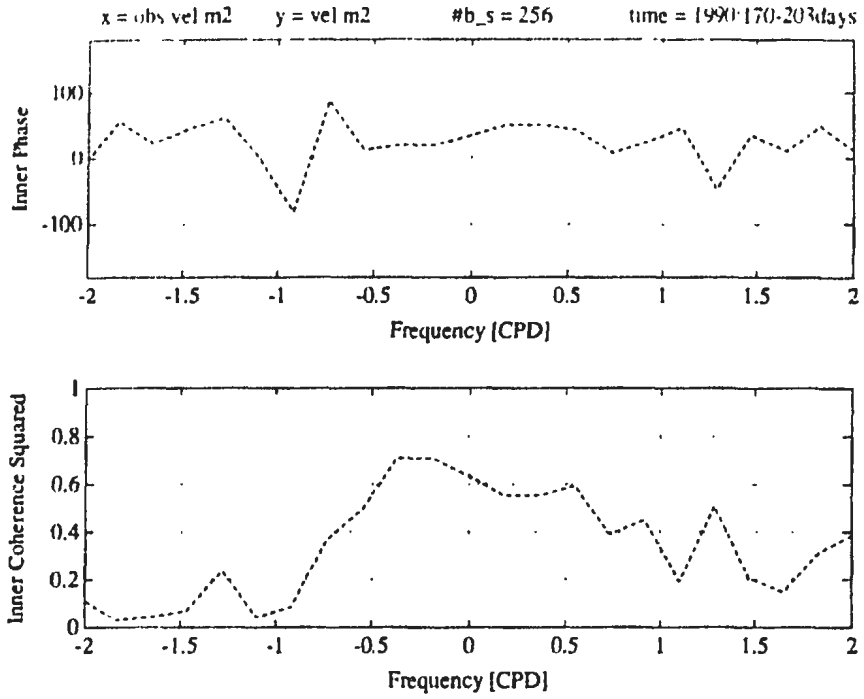

b

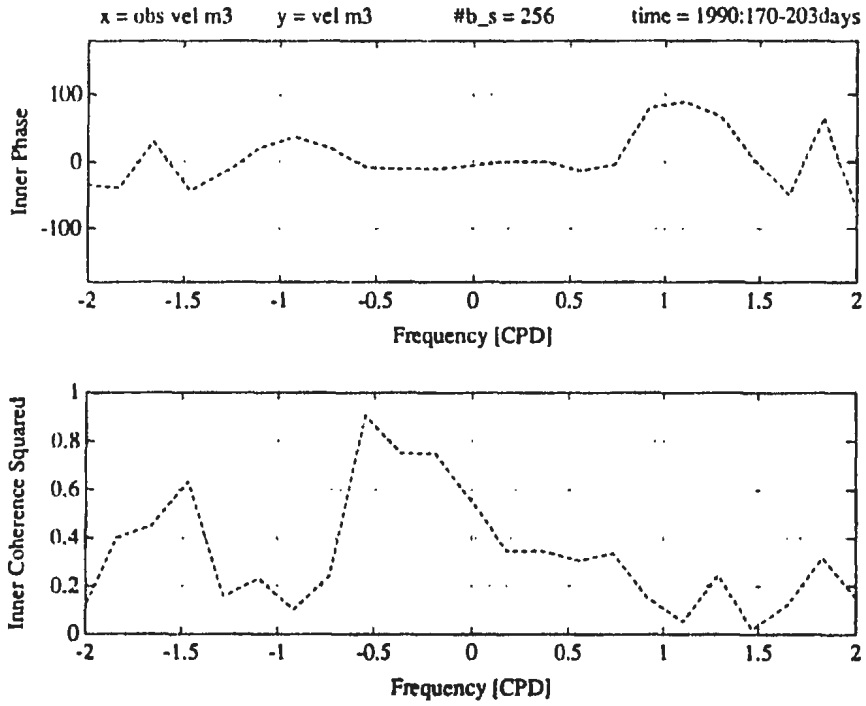

Figure 4.21 Inner spectra between observed and modelled currents at (a) M2 and (b) M3. Spectra have 12 degrees of freedom, and values of (coherence)^2 greater than 0.56 are significant at the 90% confidence level.

compared. As was mentioned in Chapter 2, the velocities at moorings 1, 2, and 3 have a strong alongshore component, while moorings 4, 5, and 6 do not. Observed and modelled alongshore components at moorings 1, 2, and 3 are shown in Figure 4.22. Agreement between the modelled and observed alongshore current at M3 is quite good. At M2, modelled and observed alongshore current are inversely correlated at times. At M1, agreement is poor. The fact that agreement at M3 is high while at the same time alongshore currents at M3 and M2 are in opposite directions is peculiar and shows the small horizontal scale of agreement in the current field in the Bay. These comparisons cast some doubt on the direction measurement at M2.

The 1989 data show reasonable coherence in temperature between stations 5 kilometers apart. However, the 1990 temperature data are very similar all around the head. Currents at neighboring stations can be compared to see if the current field has agreement on scales of 10 kilometers or more. Rotary cross-spectra between model velocities at neighboring stations show good agreement. Figure 4.23 shows a typical spectrum between modelled velocities at two neighboring stations. Values of (coherence)^2 greater than 0.56 are significant at the 90% confidence level. As expected, the inner spectrum shows high coherence and almost no phase difference at all frequencies. Figure 4.24 shows the cross-spectrum of observed velocity at the 2 moorings with best agreement, M3 and M4. At no frequency is the coherence significant in the inner spectrum. Again, rotary spectra are limited to resolving periods less than 5 days. For longer time scales Figure 4.22 shows that agreement in velocity between neighboring stations is poor and can be negatively correlated as it is between M2 and M3.

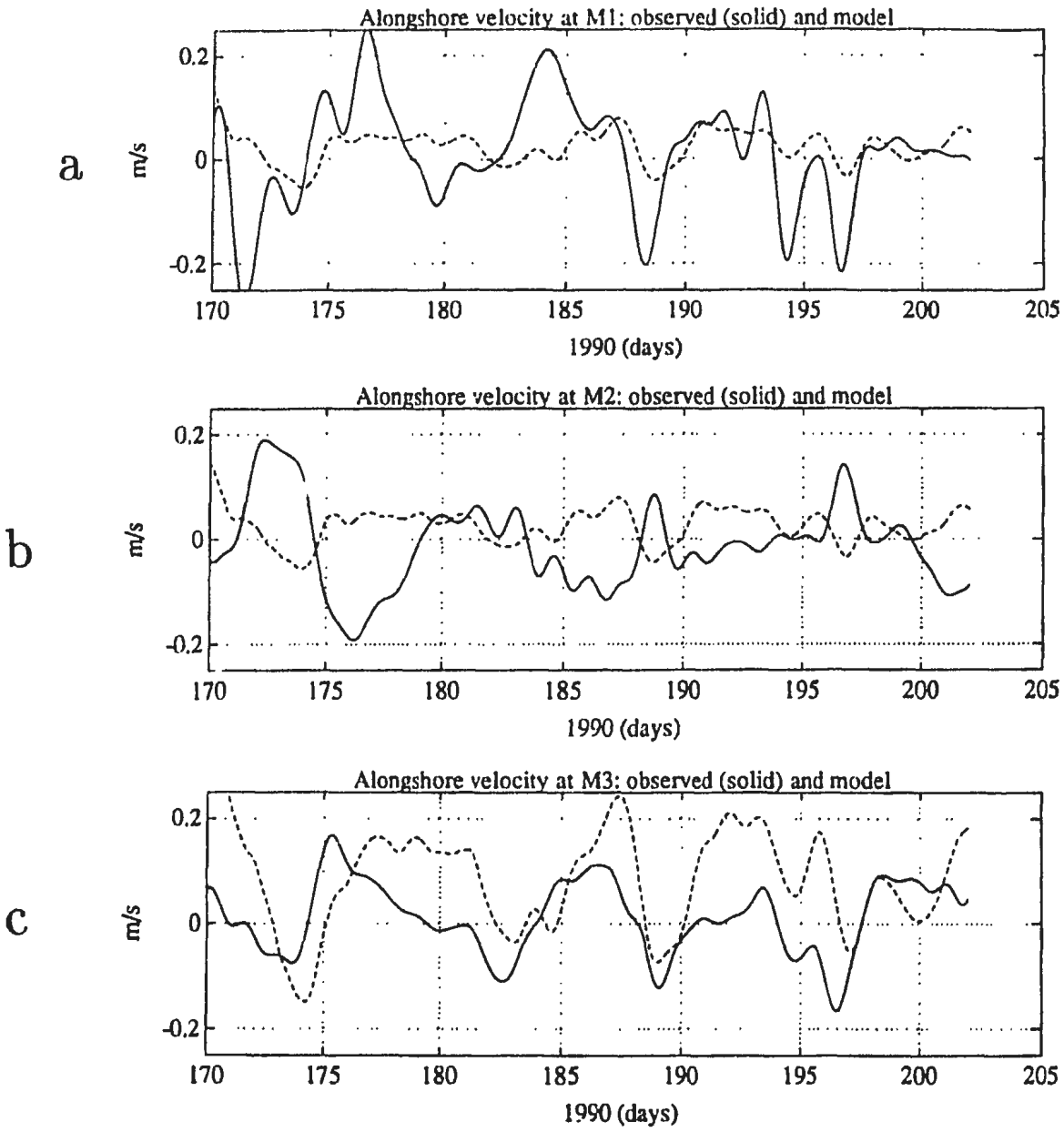

Figure 4.22 Alongshore currents (in ms^{-1}) at moorings 1, 2, and 3 (a) The solid line is the observed alongshore current at M1, and the dashed line is the modelled alongshore current (b) The solid line is the observed alongshore current at M2, and the dashed line is the modelled alongshore current. (c) The solid line is the observed alongshore current at M3, and the dashed line is the modelled alongshore current.

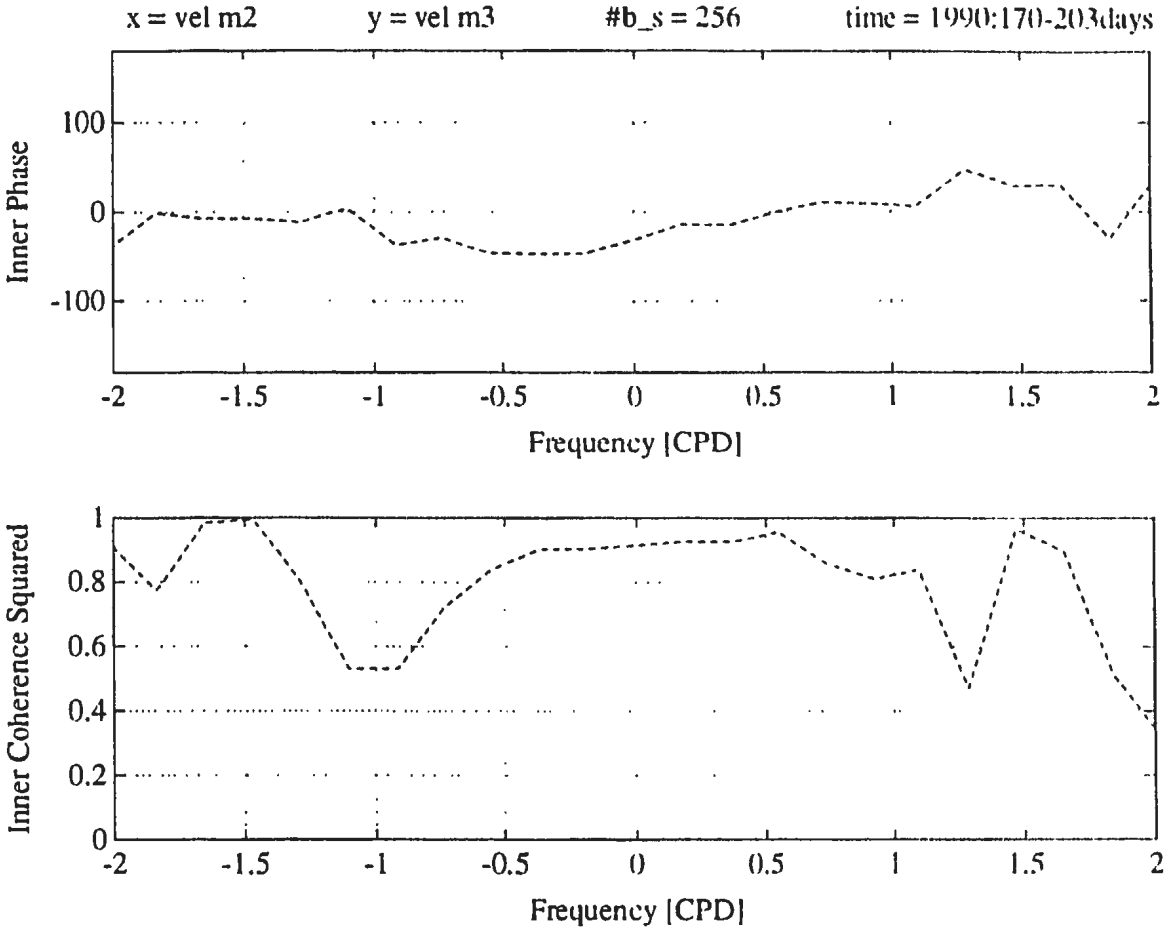

Figure 4.23 Inner spectrum between model currents at M2 and M3 from day 170 to 202. Spectrum has 12 degrees of freedom, and values of $(\text{coherence})^2$ greater than 0.56 are significant at the 90% confidence level.

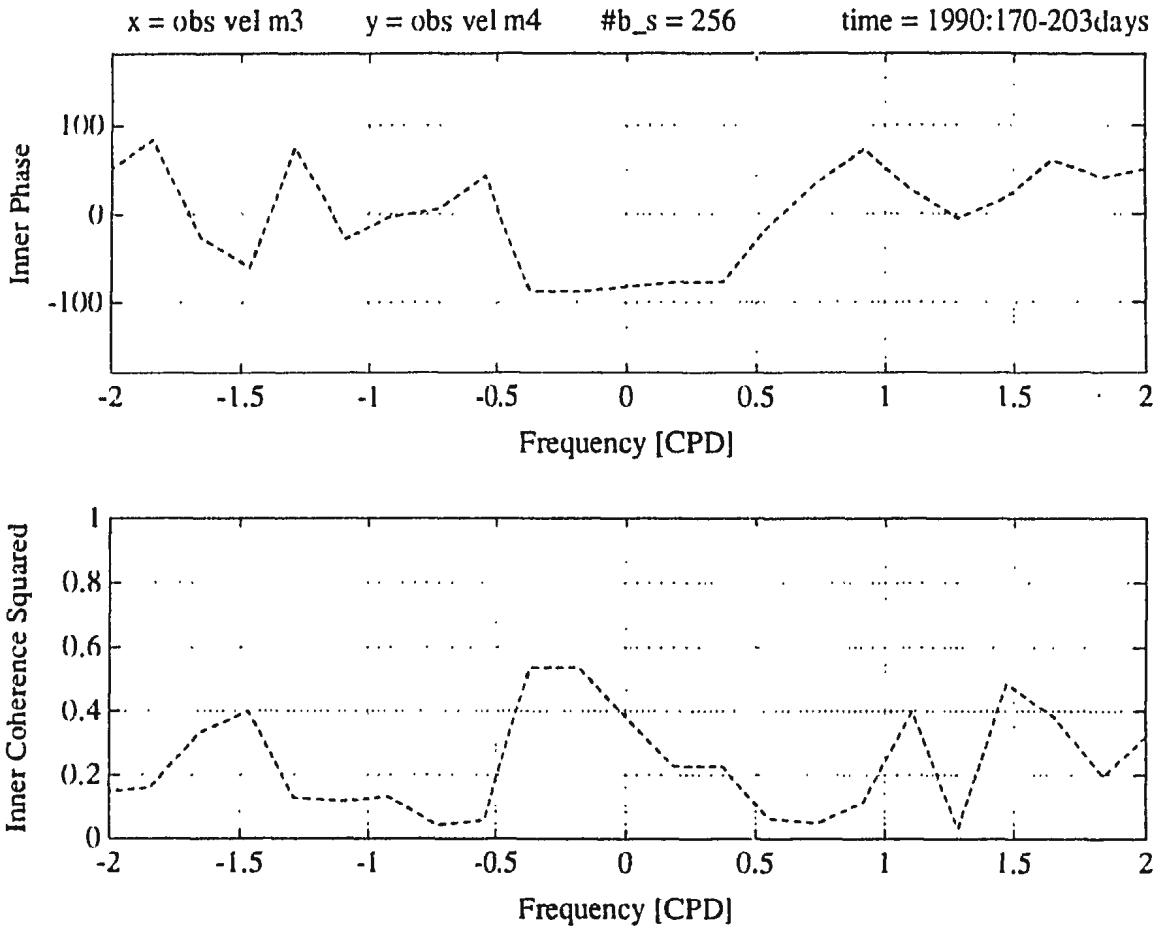

Figure 4.24 Inner spectrum between observed currents at M3 and M4 from day 170 to 202. Spectrum has 12 degrees of freedom, and values of (coherence)^2 greater than 0.56 are significant at the 90% confidence level.

Rotary cross-spectra between the observed current and wind stress show significant, but not exceptional, coherence. Since the wind stress is sampled hourly, a longer time series is required in order to have five bins of enough length to attain reliable spectra. Spectra are calculated for 150 to 203 days. Five bins of 256 points were used making significant $(\text{coherence})^2$ equal to 0.59 and the longest resolvable period 10.6 days. Figure 1.25 shows the inner spectrum between wind stress and current at the mooring with the best agreement, M3. In the inner spectrum, two significant peaks are present at -0.2 cpd with 50° and at 0.5 cpd with 80° phase difference. Similar spectra are found at moorings 1, 2, 4, and 5. Once again, spectra should not be relied upon solely for determining coherence. Direct comparison of the wind stress with the observed alongshore velocities in Figure 1.22 shows that only M3 is highly correlated with τ^y.

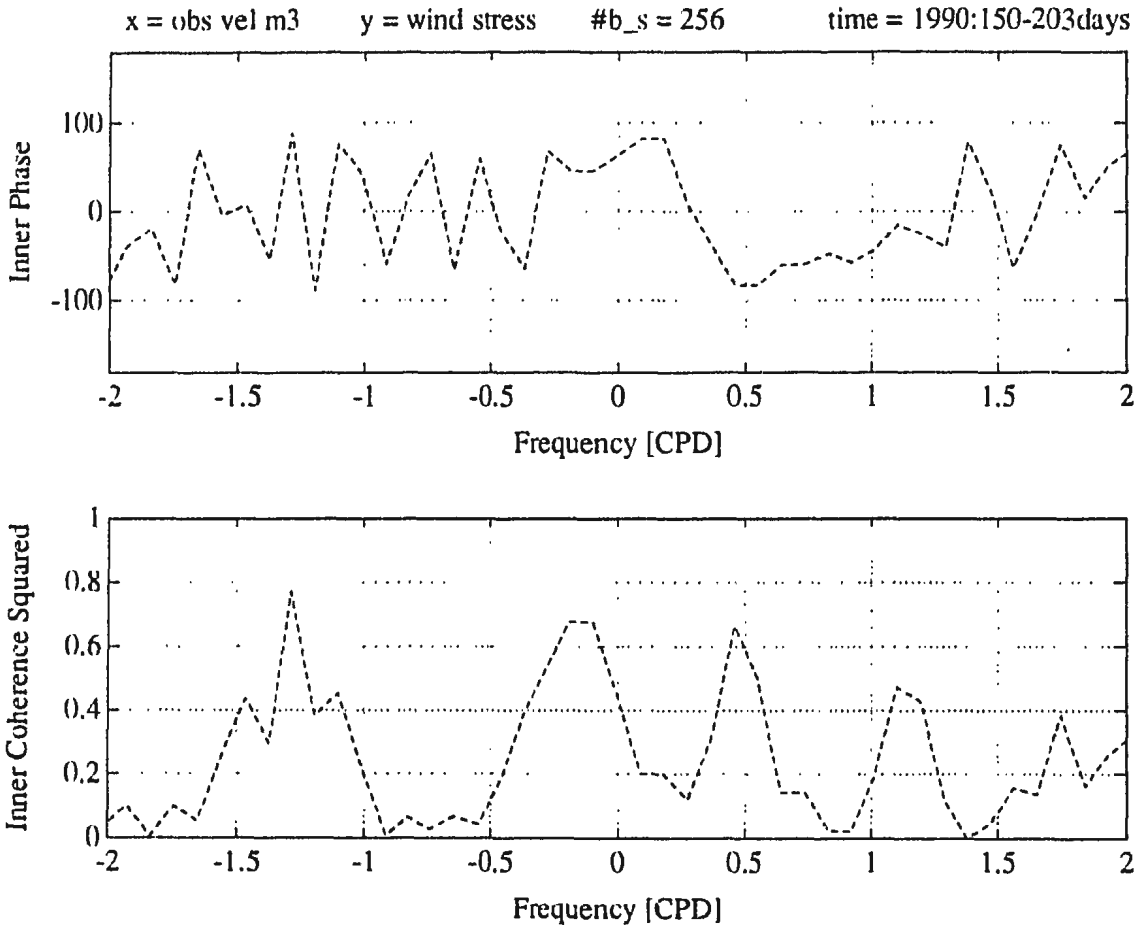

Figure 4.25 Inner spectrum between observed current at M3 and wind stress from day 150 to 202. Spectrum has 10 degrees of freedom, and values of (coherence)^2 greater than 0.59 are significant at the 90% confidence level.

CHAPTER 5: SUMMARY AND CONCLUSIONS

In this thesis, the wind-forced response of Conception Bay is evaluated. In order to accomplish this task, we have developed the simplest possible numerical model that can be used for this purpose; namely, the reduced-gravity, shallow water model. Our objective is to calculate the pycnocline response in Conception Bay to wind forcing over the Bay. The modelled response is compared with temperature and velocity measurements collected using sub-surface moorings at the mouth of the Bay in 1989 and near the head in 1990.

In order to achieve an accurate solution in the numerical model, the open boundary conditions at the mouth must be formulated in such a way as to allow disturbances generated in the bay to propagate out while at the same time preventing the inference of spurious information about the nature of the region beyond the model domain. This requires treating open boundaries from which coastal Kelvin waves can propagate into the model (i.e. "upstream" boundaries) with care. In particular, we have identified two problems which can arise when a radiation condition is applied to an "upstream" boundary which is perpendicular to the coast. First, in a case with Ekman transport away from the coast immediately "downstream" from the boundary, upwelling occurred indefinitely and propagated into the solution domain by means of Kelvin waves, completely dominating the model response. The rate of upwelling was found to be too low, however, to correspond to the case in which the coastline in the "upstream" direction is straight and extends to infinity. In another case, a radiation condition was found to generate Kelvin waves of near-inertial period which contaminated the solution. In order to deal with these problems, we extended the coastline out to sea on the "upstream" side of the mouth of the bay and applied a condition of

zero normal gradient in interface displacement on the artificial part of the boundary. This ensures that Kelvin waves cannot propagate along this stretch of the model boundary and eliminates the problems without being unduly reflective to Poincaré waves generated in the bay. It is important, however, that the other open boundaries are placed sufficiently far out from the bay, as can be shown by experimentation.

The radiation condition we have used is essentially the same as that proposed by Orlanski (1976). In our model, however, it is applied only to the interface displacement (i.e., the pressure) and not to the velocities. The velocities have their values on the boundary set equal to those at the first grid point inside. Experimentation showed that this led to less noisy solutions than if a radiation condition is applied to the velocities as well as η. Applying the radiation condition to the velocities resulted in noisier solutions even though in applying the radiation condition we were careful to separate the velocities into "free" and "forced" parts in a manner similar to that proposed by Roed and Smedstad (1984). We also experimented with using sponge layers rather than radiation conditions. Applying a sponge only to the interface displacement gave results comparable to those obtained with radiation conditions. Applying the sponge to the velocities as well gave significantly different results even when the sponge was applied to the "free" part of the velocities only and the "forced" (or Ekman) part was left undamped.

The conclusions we have drawn about the boundary condition requirements are directly applicable to three-dimensional, general circulation type models (e.g. Bryan, 1969). We noted in chapters 2 and 3 that our equations can be interpreted as those for a single baroclinic mode in a flat-bottomed, continuously stratified ocean. Even in a model which

includes bottom topography, our conclusions will apply directly if the model response along the coastal wave-guide has a strong component associated with baroclinic Kelvin waves (the Pacific coast of North America is one such location where this is likely to be the case, as demonstrated by the work of Pares-Sierra and O'Brien (989)). In a three dimensional setting, applying a condition of zero normal gradient in interface displacement across a boundary (such as on our western boundary) corresponds to setting the normal gradient of density equal to zero. Similarly, our experiments with sponge layers suggest that implementing high viscosity layers around the open boundaries of models can actually be counter-productive. It may actually be better to constrain the density field near the boundaries and leave the velocities undamped. Finally, our conclusions also apply to systems involving waves other than baroclinic Kelvin waves. As an example, Hukuda et al., (1989) and Greatbatch and Goulding (1992) have pointed out that it is unwise to run a model in which two open boundaries, or two parts of the same open boundary, are connected by f/H contours, where here H is the depth of the ocean. This is because the model then assumes that these f/H contours continue to infinity in the "upstream" direction in the sense of topographic Rossby wave propagation, leading to the establishment of large, spurious flows along these contours. The remedy in this case is to make sure that the barotropic streamfunction is specified on all "upstream" boundaries. This boundary condition problem is similar to the one addressed in this thesis.

The 1-1/2 layer model was used to simulate the wind-forced response of Conception Bay. Filtered wind stress calculated from wind measured at St. John's airport was used to drive the model. The model output was compared with temperature and velocity measurements

collected from moorings at the mouth of the Bay in 1989 and near the head in 1990. The model was able to reproduce the temperature variability (i.e. thermocline/pycnocline movement) at the head accurately but was unable to reproduce temperature at the mouth except at a period of 2 days at the mooring closest to the western shore. Observed velocity at 25 meters depth was not as well reproduced by the model as the thermocline motion; however, at the mooring closest to the coast at the head of the Bay, M3, the model current correlates well with the observed current.

The temperature signals measured at the head of the Bay in 1990 were coherent between all six moorings. Coherence in temperature between the four moorings along the western shore was highest, while coherence between the two moorings next to Bell Island and the other four moorings was slightly less but still significant. Temperature decreases present in the time series are indicative of upwelling of the thermocline and correlate well to the onset of west-southwesterly winds. Thermocline/pycnocline movement was measured using temperature at fixed depth and also by tracking an isotherm position measured by a thermistor chain. Both methods correlate well with each other. The latter method works better in the early spring when very weak stratification makes the former method ineffective.

A model simulation using an upper-layer depth of 40 meters, $g' = 7.2 \times 10^{-3}$ ms^{-2}, and a weak friction of $\epsilon = \gamma = 1/10$ days was run from day 150 to 203 in 1990. Model interface displacement correlated well with observed thermocline motion. Upwelling events were reproduced at days 173, 184, 193 and 197. Spectral analysis between the model interface displacement and temperature observed by the current meters at ~25 meters depth showed significant coherence and phase agreement at the head for frequencies less than 0.25 cpd.

Comparison between model interface displacement and the depth of the 1°C isotherm taken from the thermsistor chain data similarly showed good agreement.

Agreement between observations and the model was not as high at moorings 5 and 6 located next to Bell Island as it was at moorings 1-4. In a moderately stratified bay with large variations in bottom topography, like Conception Bay, Kelvin waves are expected to be scattered by topography as they propagate through the Bay, with the most intense scattering occurring in shallow regions with sloping bottom topography. This can be observed to some extent in the difference in temperature signals between moorings 1-4 and moorings 5 and 6. However, the upwelling signals at days 173, 183, 190 and 197 observed at moorings 1-4 are also present at moorings 5 and 6 with the signals being quite similar after about day 180. The fact that the 1-1/2 layer model, with its assumption of weak bottom velocities, reproduces the upwelling signal shows that the effects of bottom topography do not dominate this aspect of the solution.

The model was less successful at reproducing the velocity field at the head of the Bay. Rotary spectral analysis, which was limited to periods less than 5 days, showed significant coherence from -0.6 to -0.2 cpd at M3 and from -0.4 to -0.2 cpd at M2 (negative cpd indicating clockwise rotation). Visual comparison of the alongshore velocity components showed that the model and observations at M3 were strongly correlated, while the model and observations at M2 were often inversely related. Of all the moorings, M3 is located closest to the shore and along a relatively straight section of coast; therefore, one would expect the pressure part of the velocity signal to be the strongest at M3. This is shown by the high correlation between the modelled and observed velocities at M3 alone. The

fact that the long period velocity signal at M3 is opposite to the signal at M2 shows that the velocity field in the Bay has small spatial structure and is more complicated than this simple model can resolve.

The reason why the pycnocline movement was reproduced by the model while the current was not is not entirely clear. However, it should be remembered that the velocity field in the model has a very simple vertical structure, whereas in reality this structure is complicated by the presence of a turbulent surface Ekman layer and a pressure-driven velocity field below. For a current meter fixed at 25 meters depth, large vertical movement of the pycnocline could mean that sometimes the current meter is in the Ekman layer and sometimes it is not. The model velocity, on the other hand, which has only one value at each horizontal location, is an integrated representation of both the pressure driven velocity and that within the Ekman layer. Indeed, it seems likely that the primary reason why the pycnocline movement is better reproduced than velocity is that the vertical movements of the thermocline are controlled by the integral of horizontal current gradients as shown by equation 5.1:

$$w = \int_{-z}^{0} \left(\frac{\partial u}{\partial x} + \frac{\partial v}{\partial y} \right) dz. \tag{5.1}$$

Thus the thermocline field may average out a great deal of the structure of the current field.

Data collected at the mouth were found to have poorer agreement with the model than data at the head. Agreement between model and data at the mouth was seen only at 0.5 cpd at the mooring closest to the western side. The horizontal scale of temperature variations across the mouth was estimated to be ~6 km. Observed current at the mouth was found to be weakly correlated with the model.

Temperature variations at the 3 moorings across the mouth were shown to be poorly correlated with the wind. Only the 2 day period signal at the mooring closest to the western shore had significant agreement with the model. Linear theory predicts that a northeastward wind (i.e. the dominant wind in summer) will produce an upwelling signal that increases towards the head, as shown in Figure 3.12a and by the steady solution of equations (3.9) and (1.7) with $\eta \simeq 0$ at the mouth. Thus, the amplitude of the temperature variability in response to wind is expected to be smaller toward the mouth. In addition, the influence of external forcing, particularly in the form of baroclinic instabilities generated just outside Conception Bay in the Avalon Channel (Anderson, 1986) and Kelvin waves from "upstream," will be larger at the mouth. The combination of these two phenomenon provides a likely explanation for why the thermocline response is reproduced so well at the head and so poorly at the mouth.

Comparison of temperature at the 3 moorings across the mouth shows significant agreement between neighboring stations that are ~5 km apart and weaker agreement between the two stations ~10 km apart implying that the horizontal scale of temperature variation is somewhere between 5 and 10 km. All three time series show sharp increases in temperature similar to ones attributed by Anderson (1986) to baroclinic instabilities. The presence of baroclinic instabilities generated by the Labrador Current would provide another reason for the poor agreement between model and observations near the mouth.

At the mouth as at the head, the observed velocity was found to be only weakly correlated with model velocity.

REFERENCES

Aggett, D., H. S. Gaskill, D. Finlayson, S. May, C. Campbell and J. Bobbitt, 1987: A study of factors influencing availability of cod in Conception Bay, Newfoundland, in 1985. Canadian Technical Report of Fisheries and Aquatic Sciences #1562.

Anderson, C., 1986: Motions driven by buoyancy forces and atmospheric stresses in the Avalon Channel, Newfoundland, Canada. Ph. D. Thesis. Institute of Oceanography, McGill University, Montreal, Quebec, Canada.

Anderson, D. L. T., and R. A. Corry, 1985: Ocean response to low frequency wind forcing with application to the seasonal variation in the Florida Straits-Gulf Stream transport. *Prog. Oceanog.*, **14**, 7-40.

Bryan, K., 1969: A numerical method for the study of the circulation of the world ocean. *J. Comput. Phys.*, **4**, 347-376.

Buchwald, V. T., 1968: The diffraction of Kelvin waves at a corner. *J. Fluid Mech.*, **31**, 193-205.

Busalacchi, A. J., and J. J. O'Brien, 1980: The seasonal variablity in a model of the tropical Pacific. *J. Phys. Oceanogr.*, **10**, 1929-1951.

Camerlengo, A. L. and J. J. O'Brien, 1980: Open boundary conditions in rotating fluids. *J. Comp. Phys.*, **35**, 12-35.

Chapman, D. C., 1985: Numerical treatment of cross-shelf open boundaries in a barotropic coastal ocean model. *J. Phys. Oceanogr.*, **15**, 1060-1075.

Charney, J. G., R. Fjørtoft, and J. von Neumann, 1950: Numerical integration of the barotropic vorticity equation. *Tellus*, **2**, 237-254.

Csanady, G. T., 1976: Mean circulation in shallow seas. *J. Geophys. Res.*, **81**, 5389-5399.

deYoung, B., and B. Sanderson, 1992: Seasonal cycles and mean circulation in Conception Bay, Newfoundland (to be published).

Ekman, V. W., 1905: On the influence of the earth's rotation on ocean currents. *Arch. Math. Astron. Phys.*, **2**, No. 11.

Garrett, C. J. R., and D. A. Greenberg, 1977: Predicting changes in tidal regime: The open boundary problem. *J. Phys. Oceanogr.*, **7**, 171-181.

Gill, A. E., 1982: *Atmosphere-ocean dynamics*. Academic Press, 662 pp.

——, and A. J. Clarke, 1974: Wind-induced upwelling, coastal currents, and sea-level changes. *Deep-Sea Res.*, **21**, 325-345.

Gonella, J., 1972: A rotary-component method for analysing meteorological and oceanographic vector time series. *Deep-Sea Res.*, **19**, 833-846.

Greatbatch, R. J., 1983: On the response of the ocean to a moving storm: the nonlinear dynamics. *J. Phys. Oceanogr.*, **13**, 357-367.

——, and A. Goulding, 1992: A long-time-scale, density-stratified shelf circulation model. *Cont. Shelf Res.*, JONSMOD '90 issue, in press.

——, and T. Otterson, 1991: On the formulation of open boundary conditions at the mouth of a bay. *J. Geophys. Res.*, **96(C10)**, 18,431-18,445.

Hammond, T. M., Pattiaratchi, C. B., Osborne, M. J., and M. Collins, 1986: Field and flume comparisons of the modified and standard (Savonius-rotor) Aanderaa self-recording current meters. *Dt. hydrogr. Z.*, **39**, 41-63.

Heaps, N. S., 1971: On the numerical solution of the three-dimensional hydrodynamical

equations for tides and storm surges. *Mem. Soc. R. Sci. Liege*, Series 6, 143-180.

Hidaka, K., 1954: A contribution to the theory of upwelling and coastal currents. *Trans. Am. Geophys. Un.*, **35**, 431-444.

Hsieh, W. W., M. K. Davey and R. C. Wajsowicz, 1983: The free Kelvin wave in finite-difference numerical models. *J. Phys. Oceanogr.*, **13**, 1383-1397.

Hukuda, H., R. J. Greatbatch and A. E. Hay, 1989: A simple 3-D model of the circulation off Newfoundland. *J. Geophys. Res.*, **94(C9)**,12,607-12,618.

Jenkins, G. M., and D. G. Watts, 1968: *Spectral analysis and its applications*. Holden-Day, 525 pp.

Jensen, T., 1990: A numerical study of the seasonal variability of the Somali Current. Ph. D. Thesis. Mesoscale Air-Sea Interaction Group, Florida State University, Tallahassee, Florida, U.S.A., 32306.

Johnson, M. A., and J. J. O'Brien, 1990: The northeast Pacific Ocean response to the 1982-1983 El Niño. *J. Geophys. Res.*, **95(C5)**, 7155-7166.

–, and –, 1990: The role of coastal Kelvin waves on the northeast Pacific Ocean. *J. Mar. Syst.*, **1**, 29-38.

Keeley, J. R., 1981: Temperature, salinity and sigma-t at Station 27 (47°33'N, 52°35'W) an analysis of historical data. Mar. Environ. Data Serv. Tech. Rep. No. 8, Dep. of Fisheries and Oceans, Ottawa, Canada.

Kraus, E. B. and J. S. Turner, 1967: A one-dimensional model of the seasonal thermocline II. The general theory and its consequences. *Tellus*, **19**, 98-105.

Large, W. G., and S. Pond, 1981: Open ocean momentum flux measurements in moderate

to strong winds. *J. Phys. Oceanogr.*, 11, 324-336.

McCreary, J. P., 1981: A linear stratified ocean model of the equatorial undercurrent. *Philos. Trans. R. Soc. London, Ser. A*, **298**, 603-635.

Martinsen, E. A., and J. E. Weber, 1981: Frictional influence on internal Kelvin waves. *Tellus*, **33**, 402-410.

Mesinger, F., and A. Arakawa, 1976: *Numerical methods used in atmospheric models*, GARP Publ. Ser. No. 17, Vol. 1, World Meteorol. Organ. Int. Counc. Sci. Unions, Geneva.

Miller, M. J., and A. J. Thorpe, 1981: Radiation conditions for the lateral boundaries of limited-area numerical models. *Quart. J. R. Met. Soc.*, **107**, 615-628.

Mooers, C. N. K., 1973: A technique for the cross spectrum analysis of pairs of complex valued time series, with emphasis on properties of polarized components and rotational invariants. *Deep-Sea Res.*, **20**, 1129-1141.

Orlanski, I., 1976: A simple boundary condition for unbounded hyperbolic flows. *J. Comp. Phys.*, **21**, 251-269.

Packham, B. A., and W. E. Williams, 1968: Diffraction of Kelvin waves at a sharp bend. *J. Fluid Mech.*, **34**, 517-529.

Pares-Sierra, A., and J. J. O'Brien, 1989: The seasonal and interannual variability of the California Current system: A numerical model. *J. Geophys. Res.*, **94(C4)**, 3159-3180.

Petrie, B. and C. Anderson, 1983: Circulation on the Newfoundland continental shelf. *Atmosphere-Ocean*, **21**, 207-226.

. Loder, J.W., Akenhead, S., and J. Lazier, 1990: Temperature and salinity variability on the eastern Newfoundland shelf: The annual harmonic. *Atmosphere-ocean*, **29**, 14-36.

Philander, S. G. H., and Pacanowski, R. C., 1980: The generation of equatorial currents. *J. Geophys. Res.*, **85(C2)**, 1123-1136.

Pickard, G. L., and W. J. Emery, 1982: *Descriptive physical oceanography.* Pergamon Press, 249 pp.

Pollard, R. T., 1970: On the generation by winds of inertial waves in the ocean. *Deep-Sea Res.*, **17**, 795-812.

Reed, L. P., and C. K. Cooper, 1986: Open boundary conditions in numerical ocean models In: Advanced Physical Oceanographic Numerical Modeling, J. J. O'Brien, Ed., Reidel Publishing Co., 411-436.

, and O. M. Smedstad, 1984: Open boundary conditions for forced waves in a rotating fluid. *SIAM J. Sci. Stat. Comp.*, **5**, 414-426.

Sielecki, A., 1968: An energy-conserving difference scheme for storm surge equations. *Mon. Weath. Rev.*, **96**, 150-156.

Smith, P. C., and J. I. MacPherson, 1987: Cross-shore variations of near-surface wind velocity and atmospheric turbulence at the land-sea boundary during CASP. *Atmosphere-Ocean*, **25**, 279-303.

Smith, R. L., 1968: Upwelling. *Oceanogr. Mar. Biol., Ann. Rev.*, **6**, 11-46.

Sommerfeld, A., 1949: *Partial differential equations: Lectures in theoretical physics*, vol. 6, Academic Press.

Sverdrup, U. H., 1938: On the process of upwelling. *J. Mar. Res.*, 1, 155-164.

Taylor, G. I., 1920: Tidal oscillations in gulfs and rectangular bays. *Proc. London Math. Soc.*, **20**, 148-181.

Taylor, P. A., 1969: On the planetary boundary layer flow under conditions of neutral thermal stability. *J. Atmos. Sci.*, **26**, 427-431.

——, 1969: The planetary boundary layer above a change in surface roughness. *J. Atmos. Sci.*, **26**, 432-440.

Yao, T., 1986: The response of currents in Trinity Bay, Newfoundland, to local wind forcing. *Atmosphere-Ocean*, **24**, 235-252.

Yoshida, K., 1955: Coastal upwelling off the California coast. *Rec. Oceanogr. Works Jpn.*, **2**, 1-13.